Search for continuous gravitational waves from 20 accreting millisecond x-ray pulsars in O3 LIGO data

R. Abbott et al. (LIGO Scientific Collaboration, Virgo Collaboration, and KAGRA Collaboration)

Phys. Rev. D **105**, 022002 — Published 19 January 2022

DOI: 10.1103/PhysRevD.105.022002

Search for continuous gravitational waves from 20 accreting millisecond X-ray pulsars in O3 LIGO data

R. Abbott,[1] T. D. Abbott,[2] F. Acernese,[3,4] K. Ackley,[5] C. Adams,[6] N. Adhikari,[7] R. X. Adhikari,[1] V. B. Adya,[8] C. Affeldt,[9,10] D. Agarwal,[11] M. Agathos,[12,13] K. Agatsuma,[14] N. Aggarwal,[15] O. D. Aguiar,[16] L. Aiello,[17] A. Ain,[18] T. Akutsu,[19,20] S. Albanesi,[21] A. Allocca,[22,4] P. A. Altin,[8] A. Amato,[23] C. Anand,[5] S. Anand,[1] A. Ananyeva,[1] S. B. Anderson,[1] W. G. Anderson,[7] M. Ando,[24,25] T. Andrade,[26] N. Andres,[27] T. Andrić,[28] S. V. Angelova,[29] S. Ansoldi,[30,31] J. M. Antelis,[32] S. Antier,[33] S. Appert,[1] Koji Arai,[1] Koya Arai,[34] Y. Arai,[34] S. Araki,[35] A. Araya,[36] M. C. Araya,[1] J. S. Areeda,[37] M. Arène,[33] N. Aritomi,[24] N. Arnaud,[38,39] S. M. Aronson,[2] K. G. Arun,[40] H. Asada,[41] Y. Asali,[42] G. Ashton,[5] Y. Aso,[43,44] M. Assiduo,[45,46] S. M. Aston,[6] P. Astone,[47] F. Aubin,[27] C. Austin,[2] S. Babak,[33] F. Badaracco,[48] M. K. M. Bader,[49] C. Badger,[50] S. Bae,[51] Y. Bae,[52] A. M. Baer,[53] S. Bagnasco,[21] Y. Bai,[1] L. Baiotti,[54] J. Baird,[33] R. Bajpai,[55] M. Ball,[56] G. Ballardin,[39] S. W. Ballmer,[57] A. Balsamo,[53] G. Baltus,[58] S. Banagiri,[59] D. Bankar,[11] J. C. Barayoga,[1] C. Barbieri,[60,61,62] B. C. Barish,[1] D. Barker,[63] P. Barneo,[26] F. Barone,[64,4] B. Barr,[65] L. Barsotti,[66] M. Barsuglia,[33] D. Barta,[67] J. Bartlett,[63] M. A. Barton,[65,19] I. Bartos,[68] R. Bassiri,[69] A. Basti,[70,18] M. Bawaj,[71,72] J. C. Bayley,[65] A. C. Baylor,[7] M. Bazzan,[73,74] B. Bécsy,[75] V. M. Bedakihale,[76] M. Bejger,[77] I. Belahcene,[38] V. Benedetto,[78] D. Beniwal,[79] T. F. Bennett,[80] J. D. Bentley,[14] M. BenYaala,[29] F. Bergamin,[9,10] B. K. Berger,[69] S. Bernuzzi,[13] D. Bersanetti,[81] A. Bertolini,[49] J. Betzwieser,[6] D. Beveridge,[82] R. Bhandare,[83] U. Bhardwaj,[84,49] D. Bhattacharjee,[85] S. Bhaumik,[68] I. A. Bilenko,[86] G. Billingsley,[1] S. Bini,[87,88] R. Birney,[89] O. Birnholtz,[90] S. Biscans,[1,66] M. Bischi,[45,46] S. Biscoveanu,[66] A. Bisht,[9,10] B. Biswas,[11] M. Bitossi,[39,18] M.-A. Bizouard,[91] J. K. Blackburn,[1] C. D. Blair,[82,6] D. G. Blair,[82] R. M. Blair,[63] F. Bobba,[92,93] N. Bode,[9,10] M. Boer,[91] G. Bogaert,[91] M. Boldrini,[94,47] L. D. Bonavena,[73] F. Bondu,[95] E. Bonilla,[69] R. Bonnand,[27] P. Booker,[9,10] B. A. Boom,[49] R. Bork,[1] V. Boschi,[18] N. Bose,[96] S. Bose,[11] V. Bossilkov,[82] V. Boudart,[58] Y. Bouffanais,[73,74] A. Bozzi,[39] C. Bradaschia,[18] P. R. Brady,[7] A. Bramley,[6] A. Branch,[6] M. Branchesi,[28,97] J. E. Brau,[56] M. Breschi,[13] T. Briant,[98] J. H. Briggs,[65] A. Brillet,[91] M. Brinkmann,[9,10] P. Brockill,[7] A. F. Brooks,[1] J. Brooks,[39] D. D. Brown,[79] S. Brunett,[1] G. Bruno,[48] R. Bruntz,[53] J. Bryant,[14] T. Bulik,[99] H. J. Bulten,[49] A. Buonanno,[100,101] R. Buscicchio,[14] D. Buskulic,[27] C. Buy,[102] R. L. Byer,[69] L. Cadonati,[103] G. Cagnoli,[23] C. Cahillane,[63] J. Calderón Bustillo,[104,105] J. D. Callaghan,[65] T. A. Callister,[106,107] E. Calloni,[22,4] J. Cameron,[82] J. B. Camp,[108] M. Canepa,[109,81] S. Canevarolo,[110] M. Cannavacciuolo,[92] K. C. Cannon,[111] H. Cao,[79] Z. Cao,[112] E. Capocasa,[19] E. Capote,[57] G. Carapella,[92,93] F. Carbognani,[39] J. B. Carlin,[113] M. F. Carney,[15] M. Carpinelli,[114,115,39] G. Carrillo,[56] G. Carullo,[70,18] T. L. Carver,[17] J. Casanueva Diaz,[39] C. Casentini,[116,117] G. Castaldi,[118] S. Caudill,[49,110] M. Cavaglià,[85] F. Cavalier,[38] R. Cavalieri,[39] M. Ceasar,[119] G. Cella,[18] P. Cerdá-Durán,[120] E. Cesarini,[117] W. Chaibi,[91] K. Chakravarti,[11] S. Chalathadka Subrahmanya,[121] E. Champion,[122] C.-H. Chan,[123] C. Chan,[111] C. L. Chan,[105] K. Chan,[105] M. Chan,[124] K. Chandra,[96] P. Chanial,[39] S. Chao,[123] P. Charlton,[125] E. A. Chase,[15] E. Chassande-Mottin,[33] C. Chatterjee,[82] Debarati Chatterjee,[11] Deep Chatterjee,[7] M. Chaturvedi,[83] S. Chaty,[33] C. Chen,[126,127] H. Y. Chen,[66] J. Chen,[123] K. Chen,[128] X. Chen,[82] Y.-B. Chen,[129] Y.-R. Chen,[130] Z. Chen,[17] H. Cheng,[68] C. K. Cheong,[105] H. Y. Cheung,[105] H. Y. Chia,[68] F. Chiadini,[131,93] C-Y. Chiang,[132] G. Chiarini,[74] R. Chierici,[133] A. Chincarini,[81] M. L. Chiofalo,[70,18] A. Chiummo,[39] G. Cho,[134] H. S. Cho,[135] R. K. Choudhary,[82] S. Choudhary,[11] N. Christensen,[91] H. Chu,[128] Q. Chu,[82] Y-K. Chu,[132] S. Chua,[8] K. W. Chung,[50] G. Ciani,[73,74] P. Ciecielag,[77] M. Cieślar,[77] M. Cifaldi,[116,117] A. A. Ciobanu,[79] R. Ciolfi,[136,74] F. Cipriano,[91] A. Cirone,[109,81] F. Clara,[63] E. N. Clark,[137] J. A. Clark,[1,103] L. Clarke,[138] P. Clearwater,[139] S. Clesse,[140] F. Cleva,[91] E. Coccia,[28,97] E. Codazzo,[28] P.-F. Cohadon,[98] D. E. Cohen,[38] L. Cohen,[2] M. Colleoni,[141] C. G. Collette,[142] A. Colombo,[60] M. Colpi,[60,61] C. M. Compton,[63] M. Constancio Jr.,[16] L. Conti,[74] S. J. Cooper,[14] P. Corban,[6] T. R. Corbitt,[2] I. Cordero-Carrión,[143] S. Corezzi,[72,71] K. R. Corley,[42] N. Cornish,[75] D. Corre,[38] A. Corsi,[144] S. Cortese,[39] C. A. Costa,[16] R. Cotesta,[101] M. W. Coughlin,[59] J.-P. Coulon,[91] S. T. Countryman,[42] B. Cousins,[145] P. Couvares,[1] D. M. Coward,[82] M. J. Cowart,[6] D. C. Coyne,[1] R. Coyne,[146] J. D. E. Creighton,[7] T. D. Creighton,[147] A. W. Criswell,[59] M. Croquette,[98] S. G. Crowder,[148] J. R. Cudell,[58] T. J. Cullen,[2] A. Cumming,[65] R. Cummings,[65] L. Cunningham,[65] E. Cuoco,[39,149,18] M. Curyło,[99] P. Dabadie,[23] T. Dal Canton,[38] S. Dall'Osso,[28] G. Dálya,[150] A. Dana,[69] L. M. DaneshgaranBajastani,[80] B. D'Angelo,[109,81] S. Danilishin,[151,49] S. D'Antonio,[117] K. Danzmann,[9,10] C. Darsow-Fromm,[121] A. Dasgupta,[76] L. E. H. Datrier,[65] S. Datta,[11] V. Dattilo,[39] I. Dave,[83] M. Davier,[38] G. S. Davies,[152] D. Davis,[1] M. C. Davis,[119] E. J. Daw,[153] R. Dean,[119] D. DeBra,[69] M. Deenadayalan,[11] J. Degallaix,[154] M. De Laurentis,[22,4] S. Deléglise,[98] V. Del Favero,[122] F. De Lillo,[48] N. De Lillo,[65] W. Del Pozzo,[70,18] L. M. DeMarchi,[15] F. De Matteis,[116,117] V. D'Emilio,[17] N. Demos,[66]

T. Dent,[104] A. Depasse,[48] R. De Pietri,[155,156] R. De Rosa,[22,4] C. De Rossi,[39] R. DeSalvo,[118] R. De Simone,[131] S. Dhurandhar,[11] M. C. Díaz,[147] M. Diaz-Ortiz Jr.,[68] N. A. Didio,[57] T. Dietrich,[101,49] L. Di Fiore,[4] C. Di Fronzo,[14] C. Di Giorgio,[92,93] F. Di Giovanni,[120] M. Di Giovanni,[28] T. Di Girolamo,[22,4] A. Di Lieto,[70,18] B. Ding,[142] S. Di Pace,[94,47] I. Di Palma,[94,47] F. Di Renzo,[70,18] A. K. Divakarla,[68] A. Dmitriev,[14] Z. Doctor,[56] L. D'Onofrio,[22,4] F. Donovan,[66] K. L. Dooley,[17] S. Doravari,[11] I. Dorrington,[17] M. Drago,[94,47] J. C. Driggers,[63] Y. Drori,[1] J.-G. Ducoin,[38] P. Dupej,[65] O. Durante,[92,93] D. D'Urso,[114,115] P.-A. Duverne,[38] S. E. Dwyer,[63] C. Eassa,[63] P. J. Easter,[5] M. Ebersold,[157] T. Eckhardt,[121] G. Eddolls,[65] B. Edelman,[56] T. B. Edo,[1] O. Edy,[152] A. Effler,[6] S. Eguchi,[124] J. Eichholz,[8] S. S. Eikenberry,[68] M. Eisenmann,[27] R. A. Eisenstein,[66] A. Ejlli,[17] E. Engelby,[37] Y. Enomoto,[24] L. Errico,[22,4] R. C. Essick,[158] H. Estellés,[141] D. Estevez,[159] Z. Etienne,[160] T. Etzel,[1] M. Evans,[66] T. M. Evans,[6] B. E. Ewing,[145] V. Fafone,[116,117,28] H. Fair,[57] S. Fairhurst,[17] A. M. Farah,[158] S. Farinon,[81] B. Farr,[56] W. M. Farr,[106,107] N. W. Farrow,[5] E. J. Fauchon-Jones,[17] G. Favaro,[73] M. Favata,[161] M. Fays,[58] M. Fazio,[162] J. Feicht,[1] M. M. Fejer,[69] E. Fenyvesi,[67,163] D. L. Ferguson,[164] A. Fernandez-Galiana,[66] I. Ferrante,[70,18] T. A. Ferreira,[16] F. Fidecaro,[70,18] P. Figura,[99] I. Fiori,[39] M. Fishbach,[15] R. P. Fisher,[53] R. Fittipaldi,[165,93] V. Fiumara,[166,93] R. Flaminio,[27,19] E. Floden,[59] H. Fong,[111] J. A. Font,[120,167] B. Fornal,[168] P. W. F. Forsyth,[8] A. Franke,[121] S. Frasca,[94,47] F. Frasconi,[18] C. Frederick,[169] J. P. Freed,[32] Z. Frei,[150] A. Freise,[170] R. Frey,[56] P. Fritschel,[66] V. V. Frolov,[6] G. G. Fronzé,[21] Y. Fujii,[171] Y. Fujikawa,[172] M. Fukunaga,[34] M. Fukushima,[20] P. Fulda,[68] M. Fyffe,[6] H. A. Gabbard,[65] B. U. Gadre,[101] J. R. Gair,[101] J. Gais,[105] S. Galaudage,[5] R. Gamba,[13] D. Ganapathy,[66] A. Ganguly,[173] D. Gao,[174] S. G. Gaonkar,[11] B. Garaventa,[81,109] C. García-Núñez,[89] C. García-Quirós,[141] F. Garufi,[22,4] B. Gateley,[63] S. Gaudio,[32] V. Gayathri,[68] G.-G. Ge,[174] G. Gemme,[81] A. Gennai,[18] J. George,[83] O. Gerberding,[121] L. Gergely,[175] P. Gewecke,[121] S. Ghonge,[103] Abhirup Ghosh,[101] Archisman Ghosh,[176] Shaon Ghosh,[7,161] Shrobana Ghosh,[17] B. Giacomazzo,[60,61,62] L. Giacoppo,[94,47] J. A. Giaime,[2,6] K. D. Giardina,[6] D. R. Gibson,[89] C. Gier,[29] M. Giesler,[177] P. Giri,[18,70] F. Gissi,[78] J. Glanzer,[2] A. E. Gleckl,[37] P. Godwin,[145] E. Goetz,[178] R. Goetz,[68] N. Gohlke,[9,10] B. Goncharov,[5,28] G. González,[2] A. Gopakumar,[179] M. Gosselin,[39] R. Gouaty,[27] D. W. Gould,[8] B. Grace,[8] A. Grado,[180,4] M. Granata,[154] V. Granata,[92] A. Grant,[65] S. Gras,[66] P. Grassia,[1] C. Gray,[63] R. Gray,[65] G. Greco,[71] A. C. Green,[68] R. Green,[17] A. M. Gretarsson,[32] E. M. Gretarsson,[32] D. Griffith,[1] W. Griffiths,[17] H. L. Griggs,[103] G. Grignani,[72,71] A. Grimaldi,[87,88] S. J. Grimm,[28,97] H. Grote,[17] S. Grunewald,[101] P. Gruning,[38] D. Guerra,[120] G. M. Guidi,[45,46] A. R. Guimaraes,[2] G. Guixé,[26] H. K. Gulati,[76] H.-K. Guo,[168] Y. Guo,[49] Anchal Gupta,[1] Anuradha Gupta,[181] P. Gupta,[49,110] E. K. Gustafson,[1] R. Gustafson,[182] F. Guzman,[183] S. Ha,[184] L. Haegel,[33] A. Hagiwara,[34,185] S. Haino,[132] O. Halim,[31,186] E. D. Hall,[66] E. Z. Hamilton,[157] G. Hammond,[65] W.-B. Han,[187] M. Haney,[157] J. Hanks,[63] C. Hanna,[145] M. D. Hannam,[17] O. Hannuksela,[110,49] H. Hansen,[63] T. J. Hansen,[32] J. Hanson,[6] T. Harder,[91] T. Hardwick,[2] K. Haris,[49,110] J. Harms,[28,97] G. M. Harry,[188] I. W. Harry,[152] D. Hartwig,[121] K. Hasegawa,[34] B. Haskell,[77] R. K. Hasskew,[6] C.-J. Haster,[66] K. Hattori,[189] K. Haughian,[65] H. Hayakawa,[190] K. Hayama,[124] F. J. Hayes,[65] J. Healy,[122] A. Heidmann,[98] A. Heidt,[9,10] M. C. Heintze,[6] J. Heinze,[9,10] J. Heinzel,[191] H. Heitmann,[91] F. Hellman,[192] P. Hello,[38] A. F. Helmling-Cornell,[56] G. Hemming,[39] M. Hendry,[65] I. S. Heng,[65] E. Hennes,[49] J. Hennig,[193] M. H. Hennig,[193] A. G. Hernandez,[80] F. Hernandez Vivanco,[5] M. Heurs,[9,10] S. Hild,[151,49] P. Hill,[29] Y. Himemoto,[194] A. S. Hines,[183] Y. Hiranuma,[195] N. Hirata,[19] E. Hirose,[34] W. C. G. Ho,[196] S. Hochheim,[9,10] D. Hofman,[154] J. N. Hohmann,[121] D. G. Holcomb,[119] N. A. Holland,[8] I. J. Hollows,[153] Z. J. Holmes,[79] K. Holt,[6] D. E. Holz,[158] Z. Hong,[197] P. Hopkins,[17] J. Hough,[65] S. Hourihane,[129] E. J. Howell,[82] C. G. Hoy,[17] D. Hoyland,[14] A. Hreibi,[9,10] B-H. Hsieh,[34] Y. Hsu,[123] G-Z. Huang,[197] H-Y. Huang,[132] P. Huang,[174] Y-C. Huang,[130] Y.-J. Huang,[132] Y. Huang,[66] M. T. Hübner,[5] A. D. Huddart,[138] B. Hughey,[32] D. C. Y. Hui,[198] V. Hui,[27] S. Husa,[141] S. H. Huttner,[65] R. Huxford,[145] T. Huynh-Dinh,[6] S. Ide,[199] B. Idzkowski,[99] A. Iess,[116,117] B. Ikenoue,[20] S. Imam,[197] K. Inayoshi,[200] C. Ingram,[79] Y. Inoue,[128] K. Ioka,[201] M. Isi,[66] K. Isleif,[121] K. Ito,[202] Y. Itoh,[203,204] B. R. Iyer,[173] K. Izumi,[205] V. JaberianHamedan,[82] T. Jacqmin,[98] S. J. Jadhav,[206] S. P. Jadhav,[11] A. L. James,[17] A. Z. Jan,[122] K. Jani,[207] J. Janquart,[110,49] K. Janssens,[208,91] N. N. Janthalur,[206] P. Jaranowski,[209] D. Jariwala,[68] R. Jaume,[141] A. C. Jenkins,[50] K. Jenner,[79] C. Jeon,[210] M. Jeunon,[59] W. Jia,[66] H.-B. Jin,[211,212] G. R. Johns,[53] A. W. Jones,[82] D. I. Jones,[213] J. D. Jones,[63] P. Jones,[14] R. Jones,[65] R. J. G. Jonker,[49] L. Ju,[82] P. Jung,[52] K. Jung,[184] J. Junker,[9,10] V. Juste,[159] K. Kaihotsu,[202] T. Kajita,[214] M. Kakizaki,[189] C. V. Kalaghatgi,[17,110] V. Kalogera,[15] B. Kamai,[1] M. Kamiizumi,[190] N. Kanda,[203,204] S. Kandhasamy,[11] G. Kang,[215] J. B. Kanner,[1] Y. Kao,[123] S. J. Kapadia,[173] D. P. Kapasi,[8] S. Karat,[1] C. Karathanasis,[216] S. Karki,[85] R. Kashyap,[145] M. Kasprzack,[1] W. Kastaun,[9,10] S. Katsanevas,[39] E. Katsavounidis,[66] W. Katzman,[6] T. Kaur,[82] K. Kawabe,[63] K. Kawaguchi,[34] N. Kawai,[217] T. Kawasaki,[24] F. Kéfélian,[91] D. Keitel,[141] J. S. Key,[218] S. Khadka,[69] F. Y. Khalili,[86] S. Khan,[17] E. A. Khazanov,[219] N. Khetan,[28,97] M. Khursheed,[83] N. Kijbunchoo,[8] C. Kim,[220]

J. C. Kim,[221] J. Kim,[222] K. Kim,[223] W. S. Kim,[224] Y.-M. Kim,[225] C. Kimball,[15] N. Kimura,[185] M. Kinley-Hanlon,[65] R. Kirchhoff,[9,10] J. S. Kissel,[63] N. Kita,[24] H. Kitazawa,[202] L. Kleybolte,[121] S. Klimenko,[68] A. M. Knee,[178] T. D. Knowles,[160] E. Knyazev,[66] P. Koch,[9,10] G. Koekoek,[49,151] Y. Kojima,[226] K. Kokeyama,[227] S. Koley,[28] P. Kolitsidou,[17] M. Kolstein,[216] K. Komori,[66,24] V. Kondrashov,[1] A. K. H. Kong,[228] A. Kontos,[229] N. Koper,[9,10] M. Korobko,[121] K. Kotake,[124] M. Kovalam,[82] D. B. Kozak,[1] C. Kozakai,[43] R. Kozu,[190] V. Kringel,[9,10] N. V. Krishnendu,[9,10] A. Królak,[230,231] G. Kuehn,[9,10] F. Kuei,[123] P. Kuijer,[49] A. Kumar,[206] P. Kumar,[177] Rahul Kumar,[63] Rakesh Kumar,[76] J. Kume,[25] K. Kuns,[66] C. Kuo,[128] H-S. Kuo,[197] Y. Kuromiya,[202] S. Kuroyanagi,[232,233] K. Kusayanagi,[217] S. Kuwahara,[111] K. Kwak,[184] P. Lagabbe,[27] D. Laghi,[70,18] E. Lalande,[234] T. L. Lam,[105] A. Lamberts,[91,235] M. Landry,[63] B. B. Lane,[66] R. N. Lang,[66] J. Lange,[164] B. Lantz,[69] I. La Rosa,[27] A. Lartaux-Vollard,[38] P. D. Lasky,[5] M. Laxen,[6] A. Lazzarini,[1] C. Lazzaro,[73,74] P. Leaci,[94,47] S. Leavey,[9,10] Y. K. Lecoeuche,[178] H. K. Lee,[236] H. M. Lee,[134] H. W. Lee,[221] J. Lee,[134] K. Lee,[237] R. Lee,[130] J. Lehmann,[9,10] A. Lemaître,[238] M. Leonardi,[19] N. Leroy,[38] N. Letendre,[27] C. Levesque,[234] Y. Levin,[5] J. N. Leviton,[182] K. Leyde,[33] A. K. Y. Li,[1] B. Li,[123] J. Li,[15] K. L. Li,[239] T. G. F. Li,[105] X. Li,[129] C-Y. Lin,[240] F-K. Lin,[132] F-L. Lin,[197] H. L. Lin,[128] L. C.-C. Lin,[184] F. Linde,[241,49] S. D. Linker,[80] J. N. Linley,[65] T. B. Littenberg,[242] G. C. Liu,[126] J. Liu,[9,10] K. Liu,[123] X. Liu,[7] F. Llamas,[147] M. Llorens-Monteagudo,[120] R. K. L. Lo,[1] A. Lockwood,[243] L. T. London,[66] A. Longo,[244,245] D. Lopez,[157] M. Lopez Portilla,[110] M. Lorenzini,[116,117] V. Loriette,[246] M. Lormand,[6] G. Losurdo,[18] T. P. Lott,[103] J. D. Lough,[9,10] C. O. Lousto,[122] G. Lovelace,[37] J. F. Lucaccioni,[169] H. Lück,[9,10] D. Lumaca,[116,117] A. P. Lundgren,[152] L.-W. Luo,[132] J. E. Lynam,[53] R. Macas,[152] M. MacInnis,[66] D. M. Macleod,[17] I. A. O. MacMillan,[1] A. Macquet,[91] I. Magaña Hernandez,[7] C. Magazzù,[18] R. M. Magee,[1] R. Maggiore,[14] M. Magnozzi,[81,109] S. Mahesh,[160] E. Majorana,[94,47] C. Makarem,[1] I. Maksimovic,[246] S. Maliakal,[1] A. Malik,[83] N. Man,[91] V. Mandic,[59] V. Mangano,[94,47] J. L. Mango,[247] G. L. Mansell,[63,66] M. Manske,[7] M. Mantovani,[39] M. Mapelli,[73,74] F. Marchesoni,[248,71,249] M. Marchio,[19] F. Marion,[27] Z. Mark,[129] S. Márka,[42] Z. Márka,[42] C. Markakis,[12] A. S. Markosyan,[69] A. Markowitz,[1] E. Maros,[1] A. Marquina,[143] S. Marsat,[33] F. Martelli,[45,46] I. W. Martin,[65] R. M. Martin,[161] M. Martinez,[216] V. A. Martinez,[68] V. Martinez,[23] K. Martinovic,[50] D. V. Martynov,[14] E. J. Marx,[66] H. Masalehdan,[121] K. Mason,[66] E. Massera,[153] A. Masserot,[27] T. J. Massinger,[66] M. Masso-Reid,[65] S. Mastrogiovanni,[33] A. Matas,[101] M. Mateu-Lucena,[141] F. Matichard,[1,66] M. Matiushechkina,[9,10] N. Mavalvala,[66] J. J. McCann,[82] R. McCarthy,[63] D. E. McClelland,[8] P. K. McClincy,[145] S. McCormick,[6] L. McCuller,[66] G. I. McGhee,[65] S. C. McGuire,[250] C. McIsaac,[152] J. McIver,[178] T. McRae,[8] S. T. McWilliams,[160] D. Meacher,[7] M. Mehmet,[9,10] A. K. Mehta,[101] Q. Meijer,[110] A. Melatos,[113] D. A. Melchor,[37] G. Mendell,[63] A. Menendez-Vazquez,[216] C. S. Menoni,[162] R. A. Mercer,[7] L. Mereni,[154] K. Merfeld,[56] E. L. Merilh,[6] J. D. Merritt,[56] M. Merzougui,[91] S. Meshkov,[1,*] C. Messenger,[65] C. Messick,[164] P. M. Meyers,[113] F. Meylahn,[9,10] A. Mhaske,[11] A. Miani,[87,88] H. Miao,[14] I. Michaloliakos,[68] C. Michel,[154] Y. Michimura,[24] H. Middleton,[113] L. Milano,[22] A. L. Miller,[48] A. Miller,[80] B. Miller,[84,49] M. Millhouse,[113] J. C. Mills,[17] E. Milotti,[186,31] O. Minazzoli,[91,251] Y. Minenkov,[117] N. Mio,[252] Ll. M. Mir,[216] M. Miravet-Tenés,[120] C. Mishra,[253] T. Mishra,[68] T. Mistry,[153] S. Mitra,[11] V. P. Mitrofanov,[86] G. Mitselmakher,[68] R. Mittleman,[66] O. Miyakawa,[190] A. Miyamoto,[203] Y. Miyazaki,[24] K. Miyo,[190] S. Miyoki,[190] Geoffrey Mo,[66] E. Moguel,[169] K. Mogushi,[85] S. R. P. Mohapatra,[66] S. R. Mohite,[7] I. Molina,[37] M. Molina-Ruiz,[192] M. Mondin,[80] M. Montani,[45,46] C. J. Moore,[14] D. Moraru,[63] F. Morawski,[77] A. More,[11] C. Moreno,[32] G. Moreno,[63] Y. Mori,[202] S. Morisaki,[7] Y. Moriwaki,[189] B. Mours,[159] C. M. Mow-Lowry,[14,170] S. Mozzon,[152] F. Muciaccia,[94,47] Arunava Mukherjee,[254] D. Mukherjee,[145] Soma Mukherjee,[147] Subroto Mukherjee,[76] Suvodip Mukherjee,[84] N. Mukund,[9,10] A. Mullavey,[6] J. Munch,[79] E. A. Muñiz,[57] P. G. Murray,[65] R. Musenich,[81,109] S. Muusse,[79] S. L. Nadji,[9,10] K. Nagano,[205] S. Nagano,[255] A. Nagar,[21,256] K. Nakamura,[19] H. Nakano,[257] M. Nakano,[34] R. Nakashima,[217] Y. Nakayama,[202] V. Napolano,[39] I. Nardecchia,[116,117] T. Narikawa,[34] L. Naticchioni,[47] B. Nayak,[80] R. K. Nayak,[258] R. Negishi,[195] B. F. Neil,[82] J. Neilson,[78,93] G. Nelemans,[259] T. J. N. Nelson,[6] M. Nery,[9,10] P. Neubauer,[169] A. Neunzert,[218] K. Y. Ng,[66] S. W. S. Ng,[79] C. Nguyen,[33] P. Nguyen,[56] T. Nguyen,[66] L. Nguyen Quynh,[260] W.-T. Ni,[211,174,130] S. A. Nichols,[2] A. Nishizawa,[25] S. Nissanke,[84,49] E. Nitoglia,[133] F. Nocera,[39] M. Norman,[17] C. North,[17] S. Nozaki,[189] L. K. Nuttall,[152] J. Oberling,[63] B. D. O'Brien,[68] Y. Obuchi,[20] J. O'Dell,[138] E. Oelker,[65] W. Ogaki,[34] G. Oganesyan,[28,97] J. J. Oh,[224] K. Oh,[198] S. H. Oh,[224] M. Ohashi,[190] N. Ohishi,[43] M. Ohkawa,[172] F. Ohme,[9,10] H. Ohta,[111] M. A. Okada,[16] Y. Okutani,[199] K. Okutomi,[190] C. Olivetto,[39] K. Oohara,[195] C. Ooi,[24] R. Oram,[6] B. O'Reilly,[6] R. G. Ormiston,[59] N. D. Ormsby,[53] L. F. Ortega,[68] R. O'Shaughnessy,[122] E. O'Shea,[177] S. Oshino,[190] S. Ossokine,[101] C. Osthelder,[1] S. Otabe,[217] D. J. Ottaway,[79] H. Overmier,[6] A. E. Pace,[145] G. Pagano,[70,18] M. A. Page,[82] G. Pagliaroli,[28,97] A. Pai,[96] S. A. Pai,[83] J. R. Palamos,[56] O. Palashov,[219] C. Palomba,[47] H. Pan,[123] K. Pan,[130,228] P. K. Panda,[206] H. Pang,[128] P. T. H. Pang,[49,110] C. Pankow,[15] F. Pannarale,[94,47] B. C. Pant,[83]

F. H. Panther,[82] F. Paoletti,[18] A. Paoli,[39] A. Paolone,[47,261] A. Parisi,[126] H. Park,[7] J. Park,[262] W. Parker,[6,250] D. Pascucci,[49] A. Pasqualetti,[39] R. Passaquieti,[70,18] D. Passuello,[18] M. Patel,[53] M. Pathak,[79] B. Patricelli,[39,18] A. S. Patron,[2] S. Patrone,[94,47] S. Paul,[56] E. Payne,[5] M. Pedraza,[1] M. Pegoraro,[74] A. Pele,[6] F. E. Peña Arellano,[190] S. Penn,[263] A. Perego,[87,88] A. Pereira,[23] T. Pereira,[264] C. J. Perez,[63] C. Périgois,[27] C. C. Perkins,[68] A. Perreca,[87,88] S. Perriès,[133] J. Petermann,[121] D. Petterson,[1] H. P. Pfeiffer,[101] K. A. Pham,[59] K. S. Phukon,[49,241] O. J. Piccinni,[47] M. Pichot,[91] M. Piendibene,[70,18] F. Piergiovanni,[45,46] L. Pierini,[94,47] V. Pierro,[78,93] G. Pillant,[39] M. Pillas,[38] F. Pilo,[18] L. Pinard,[154] I. M. Pinto,[78,93,265] M. Pinto,[39] K. Piotrzkowski,[48] M. Pirello,[63] M. D. Pitkin,[266] E. Placidi,[94,47] L. Planas,[141] W. Plastino,[244,245] C. Pluchar,[137] R. Poggiani,[70,18] E. Polini,[27] D. Y. T. Pong,[105] S. Ponrathnam,[11] P. Popolizio,[39] E. K. Porter,[33] R. Poulton,[39] J. Powell,[139] M. Pracchia,[27] T. Pradier,[159] A. K. Prajapati,[76] K. Prasai,[69] R. Prasanna,[206] G. Pratten,[14] M. Principe,[78,265,93] G. A. Prodi,[267,88] L. Prokhorov,[14] P. Prosposito,[116,117] L. Prudenzi,[101] A. Puecher,[49,110] M. Punturo,[71] F. Puosi,[18,70] P. Puppo,[47] M. Pürrer,[101] H. Qi,[17] V. Quetschke,[147] R. Quitzow-James,[85] F. J. Raab,[63] G. Raaijmakers,[84,49] H. Radkins,[63] N. Radulesco,[91] P. Raffai,[150] S. X. Rail,[234] S. Raja,[83] C. Rajan,[83] K. E. Ramirez,[6] T. D. Ramirez,[37] A. Ramos-Buades,[101] J. Rana,[145] P. Rapagnani,[94,47] U. D. Rapol,[268] A. Ray,[7] V. Raymond,[17] N. Raza,[178] M. Razzano,[70,18] J. Read,[37] L. A. Rees,[188] T. Regimbau,[27] L. Rei,[81] S. Reid,[29] S. W. Reid,[53] D. H. Reitze,[1,68] P. Relton,[17] A. Renzini,[1] P. Rettegno,[269,21] M. Rezac,[37] F. Ricci,[94,47] D. Richards,[138] J. W. Richardson,[1] L. Richardson,[183] G. Riemenschneider,[269,21] K. Riles,[182] S. Rinaldi,[18,70] K. Rink,[178] M. Rizzo,[15] N. A. Robertson,[1,65] R. Robie,[1] F. Robinet,[38] A. Rocchi,[117] S. Rodriguez,[37] L. Rolland,[27] J. G. Rollins,[1] M. Romanelli,[95] R. Romano,[3,4] C. L. Romel,[63] A. Romero-Rodríguez,[216] I. M. Romero-Shaw,[5] J. H. Romie,[6] S. Ronchini,[28,97] L. Rosa,[4,22] C. A. Rose,[7] D. Rosińska,[99] M. P. Ross,[243] S. Rowan,[65] S. J. Rowlinson,[14] S. Roy,[110] Santosh Roy,[11] Soumen Roy,[270] D. Rozza,[114,115] P. Ruggi,[39] K. Ryan,[63] S. Sachdev,[145] T. Sadecki,[63] J. Sadiq,[104] N. Sago,[271] S. Saito,[20] Y. Saito,[190] K. Sakai,[272] Y. Sakai,[195] M. Sakellariadou,[50] Y. Sakuno,[124] O. S. Salafia,[62,61,60] L. Salconi,[39] M. Saleem,[59] F. Salemi,[87,88] A. Samajdar,[49,110] E. J. Sanchez,[1] J. H. Sanchez,[37] L. E. Sanchez,[1] N. Sanchis-Gual,[273] J. R. Sanders,[274] A. Sanuy,[26] T. R. Saravanan,[11] N. Sarin,[5] B. Sassolas,[154] H. Satari,[82] S. Sato,[275] T. Sato,[172] O. Sauter,[68] R. L. Savage,[63] T. Sawada,[203] D. Sawant,[96] H. L. Sawant,[11] S. Sayah,[154] D. Schaetzl,[1] M. Scheel,[129] J. Scheuer,[15] M. Schiworski,[79] P. Schmidt,[14] S. Schmidt,[110] R. Schnabel,[121] M. Schneewind,[9,10] R. M. S. Schofield,[56] A. Schönbeck,[121] B. W. Schulte,[9,10] B. F. Schutz,[17,9,10] E. Schwartz,[17] J. Scott,[65] S. M. Scott,[8] M. Seglar-Arroyo,[27] T. Sekiguchi,[25] Y. Sekiguchi,[276] D. Sellers,[6] A. S. Sengupta,[270] D. Sentenac,[39] E. G. Seo,[105] V. Sequino,[22,4] A. Sergeev,[219] Y. Setyawati,[110] T. Shaffer,[63] M. S. Shahriar,[15] B. Shams,[168] L. Shao,[200] A. Sharma,[28,97] P. Sharma,[83] P. Shawhan,[100] N. S. Shcheblanov,[238] S. Shibagaki,[124] M. Shikauchi,[111] R. Shimizu,[20] T. Shimoda,[24] K. Shimode,[190] H. Shinkai,[277] T. Shishido,[44] A. Shoda,[19] D. H. Shoemaker,[66] D. M. Shoemaker,[164] S. ShyamSundar,[83] M. Sieniawska,[99] D. Sigg,[63] L. P. Singer,[108] D. Singh,[145] N. Singh,[99] A. Singha,[151,49] A. M. Sintes,[141] V. Sipala,[114,115] V. Skliris,[17] B. J. J. Slagmolen,[8] T. J. Slaven-Blair,[82] J. Smetana,[14] J. R. Smith,[37] R. J. E. Smith,[5] J. Soldateschi,[278,279,46] S. N. Somala,[280] K. Somiya,[217] E. J. Son,[224] K. Soni,[11] S. Soni,[2] V. Sordini,[133] F. Sorrentino,[81] N. Sorrentino,[70,18] H. Sotani,[281] R. Soulard,[91] T. Souradeep,[268,11] E. Sowell,[144] V. Spagnuolo,[151,49] A. P. Spencer,[65] M. Spera,[73,74] R. Srinivasan,[91] A. K. Srivastava,[76] V. Srivastava,[57] K. Staats,[15] C. Stachie,[91] D. A. Steer,[33] J. Steinlechner,[151,49] S. Steinlechner,[151,49] D. J. Stops,[14] M. Stover,[169] K. A. Strain,[65] L. C. Strang,[113] G. Stratta,[282,46] A. Strunk,[63] R. Sturani,[264] A. L. Stuver,[119] S. Sudhagar,[11] V. Sudhir,[66] R. Sugimoto,[283,205] H. G. Suh,[7] T. Z. Summerscales,[284] H. Sun,[82] L. Sun,[8] S. Sunil,[76] A. Sur,[77] J. Suresh,[111,34] P. J. Sutton,[17] Takamasa Suzuki,[172] Toshikazu Suzuki,[34] B. L. Swinkels,[49] M. J. Szczepańczyk,[68] P. Szewczyk,[99] M. Tacca,[49] H. Tagoshi,[34] S. C. Tait,[65] H. Takahashi,[285] R. Takahashi,[19] A. Takamori,[36] S. Takano,[24] H. Takeda,[24] M. Takeda,[203] C. J. Talbot,[29] C. Talbot,[1] H. Tanaka,[286] Kazuyuki Tanaka,[203] Kenta Tanaka,[286] Taiki Tanaka,[34] Takahiro Tanaka,[271] A. J. Tanasijczuk,[48] S. Tanioka,[19,44] D. B. Tanner,[68] D. Tao,[1] L. Tao,[68] E. N. Tapia San Martín,[49,19] C. Taranto,[116] J. D. Tasson,[191] S. Telada,[287] R. Tenorio,[141] J. E. Terhune,[119] L. Terkowski,[121] M. P. Thirugnanasambandam,[11] M. Thomas,[6] P. Thomas,[63] J. E. Thompson,[17] S. R. Thondapu,[83] K. A. Thorne,[6] E. Thrane,[5] Shubhanshu Tiwari,[157] Srishti Tiwari,[11] V. Tiwari,[17] A. M. Toivonen,[59] K. Toland,[65] A. E. Tolley,[152] T. Tomaru,[19] Y. Tomigami,[203] T. Tomura,[190] M. Tonelli,[70,18] A. Torres-Forné,[120] C. I. Torrie,[1] I. Tosta e Melo,[114,115] D. Töyrä,[8] A. Trapananti,[248,71] F. Travasso,[71,248] G. Traylor,[6] M. Trevor,[100] M. C. Tringali,[39] A. Tripathee,[182] L. Troiano,[288,93] A. Trovato,[33] L. Trozzo,[4,190] R. J. Trudeau,[1] D. S. Tsai,[123] D. Tsai,[123] K. W. Tsang,[49,289,110] T. Tsang,[290] J-S. Tsao,[197] M. Tse,[66] R. Tso,[129] K. Tsubono,[24] S. Tsuchida,[203] L. Tsukada,[111] D. Tsuna,[111] T. Tsutsui,[111] T. Tsuzuki,[20] K. Turbang,[291,208] M. Turconi,[91] D. Tuyenbayev,[203] A. S. Ubhi,[14] N. Uchikata,[34] T. Uchiyama,[190] R. P. Udall,[1] A. Ueda,[185] T. Uehara,[292,293] K. Ueno,[111] G. Ueshima,[294] C. S. Unnikrishnan,[179] F. Uraguchi,[20] A. L. Urban,[2]

T. Ushiba,[190] A. Utina,[151,49] H. Vahlbruch,[9,10] G. Vajente,[1] A. Vajpeyi,[5] G. Valdes,[183] M. Valentini,[87,88] V. Valsan,[7] N. van Bakel,[49] M. van Beuzekom,[49] J. F. J. van den Brand,[151,295,49] C. Van Den Broeck,[110,49] D. C. Vander-Hyde,[57] L. van der Schaaf,[49] J. V. van Heijningen,[48] J. Vanosky,[1] M. H. P. M. van Putten,[296] N. van Remortel,[208] M. Vardaro,[241,49] A. F. Vargas,[113] V. Varma,[177] M. Vasúth,[67] A. Vecchio,[14] G. Vedovato,[74] J. Veitch,[65] P. J. Veitch,[79] J. Venneberg,[9,10] G. Venugopalan,[1] D. Verkindt,[27] P. Verma,[231] Y. Verma,[83] D. Veske,[42] F. Vetrano,[45] A. Viceré,[45,46] S. Vidyant,[57] A. D. Viets,[247] A. Vijaykumar,[173] V. Villa-Ortega,[104] J.-Y. Vinet,[91] A. Virtuoso,[186,31] S. Vitale,[66] T. Vo,[57] H. Vocca,[72,71] E. R. G. von Reis,[63] J. S. A. von Wrangel,[9,10] C. Vorvick,[63] S. P. Vyatchanin,[86] L. E. Wade,[169] M. Wade,[169] K. J. Wagner,[122] R. C. Walet,[49] M. Walker,[53] G. S. Wallace,[29] L. Wallace,[1] S. Walsh,[7] J. Wang,[174] J. Z. Wang,[182] W. H. Wang,[147] R. L. Ward,[8] J. Warner,[63] M. Was,[27] T. Washimi,[19] N. Y. Washington,[1] J. Watchi,[142] B. Weaver,[63] S. A. Webster,[65] M. Weinert,[9,10] A. J. Weinstein,[1] R. Weiss,[66] C. M. Weller,[243] F. Wellmann,[9,10] L. Wen,[82] P. Weßels,[9,10] K. Wette,[8] J. T. Whelan,[122] D. D. White,[37] B. F. Whiting,[68] C. Whittle,[66] D. Wilken,[9,10] D. Williams,[65] M. J. Williams,[65] A. R. Williamson,[152] J. L. Willis,[1] B. Willke,[9,10] D. J. Wilson,[137] W. Winkler,[9,10] C. C. Wipf,[1] T. Wlodarczyk,[101] G. Woan,[65] J. Woehler,[9,10] J. K. Wofford,[122] I. C. F. Wong,[105] C. Wu,[130] D. S. Wu,[9,10] H. Wu,[130] S. Wu,[130] D. M. Wysocki,[7] L. Xiao,[1] W-R. Xu,[197] T. Yamada,[286] H. Yamamoto,[1] Kazuhiro Yamamoto,[189] Kohei Yamamoto,[286] T. Yamamoto,[190] K. Yamashita,[202] R. Yamazaki,[199] F. W. Yang,[168] L. Yang,[162] Y. Yang,[297] Yang Yang,[68] Z. Yang,[59] M. J. Yap,[8] D. W. Yeeles,[17] A. B. Yelikar,[122] M. Ying,[123] K. Yokogawa,[202] J. Yokoyama,[25,24] T. Yokozawa,[190] J. Yoo,[177] T. Yoshioka,[202] Hang Yu,[129] Haocun Yu,[66] H. Yuzurihara,[34] A. Zadrożny,[231] M. Zanolin,[32] S. Zeidler,[298] T. Zelenova,[39] J.-P. Zendri,[74] M. Zevin,[158] M. Zhan,[174] H. Zhang,[197] J. Zhang,[82] L. Zhang,[1] T. Zhang,[14] Y. Zhang,[183] C. Zhao,[82] G. Zhao,[142] Y. Zhao,[19] Yue Zhao,[168] R. Zhou,[192] Z. Zhou,[15] X. J. Zhu,[5] Z.-H. Zhu,[112] M. E. Zucker,[1,66] J. Zweizig,[1] A. C. Albayati,[299] D. Altamirano,[299] P. Bult,[300,301] D. Chakrabarty,[302] M. Ng,[302] P. S. Ray,[303] A. Sanna,[304] and T. E. Strohmayer[305]

(The LIGO Scientific Collaboration, the Virgo Collaboration, and the KAGRA Collaboration)

[1] *LIGO Laboratory, California Institute of Technology, Pasadena, CA 91125, USA*
[2] *Louisiana State University, Baton Rouge, LA 70803, USA*
[3] *Dipartimento di Farmacia, Università di Salerno, I-84084 Fisciano, Salerno, Italy*
[4] *INFN, Sezione di Napoli, Complesso Universitario di Monte S. Angelo, I-80126 Napoli, Italy*
[5] *OzGrav, School of Physics & Astronomy, Monash University, Clayton 3800, Victoria, Australia*
[6] *LIGO Livingston Observatory, Livingston, LA 70754, USA*
[7] *University of Wisconsin-Milwaukee, Milwaukee, WI 53201, USA*
[8] *OzGrav, Australian National University, Canberra, Australian Capital Territory 0200, Australia*
[9] *Max Planck Institute for Gravitational Physics (Albert Einstein Institute), D-30167 Hannover, Germany*
[10] *Leibniz Universität Hannover, D-30167 Hannover, Germany*
[11] *Inter-University Centre for Astronomy and Astrophysics, Pune 411007, India*
[12] *University of Cambridge, Cambridge CB2 1TN, United Kingdom*
[13] *Theoretisch-Physikalisches Institut, Friedrich-Schiller-Universität Jena, D-07743 Jena, Germany*
[14] *University of Birmingham, Birmingham B15 2TT, United Kingdom*
[15] *Center for Interdisciplinary Exploration & Research in Astrophysics (CIERA), Northwestern University, Evanston, IL 60208, USA*
[16] *Instituto Nacional de Pesquisas Espaciais, 12227-010 São José dos Campos, São Paulo, Brazil*
[17] *Gravity Exploration Institute, Cardiff University, Cardiff CF24 3AA, United Kingdom*
[18] *INFN, Sezione di Pisa, I-56127 Pisa, Italy*
[19] *Gravitational Wave Science Project, National Astronomical Observatory of Japan (NAOJ), Mitaka City, Tokyo 181-8588, Japan*
[20] *Advanced Technology Center, National Astronomical Observatory of Japan (NAOJ), Mitaka City, Tokyo 181-8588, Japan*
[21] *INFN Sezione di Torino, I-10125 Torino, Italy*
[22] *Università di Napoli "Federico II", Complesso Universitario di Monte S. Angelo, I-80126 Napoli, Italy*
[23] *Université de Lyon, Université Claude Bernard Lyon 1, CNRS, Institut Lumière Matière, F-69622 Villeurbanne, France*
[24] *Department of Physics, The University of Tokyo, Bunkyo-ku, Tokyo 113-0033, Japan*
[25] *Research Center for the Early Universe (RESCEU), The University of Tokyo, Bunkyo-ku, Tokyo 113-0033, Japan*
[26] *Institut de Ciències del Cosmos (ICCUB), Universitat de Barcelona, C/ Martí i Franquès 1, Barcelona, 08028, Spain*
[27] *Laboratoire d'Annecy de Physique des Particules (LAPP), Univ. Grenoble Alpes, Université Savoie Mont Blanc, CNRS/IN2P3, F-74941 Annecy, France*
[28] *Gran Sasso Science Institute (GSSI), I-67100 L'Aquila, Italy*
[29] *SUPA, University of Strathclyde, Glasgow G1 1XQ, United Kingdom*
[30] *Dipartimento di Scienze Matematiche, Informatiche e Fisiche, Università di Udine, I-33100 Udine, Italy*

[31] *INFN, Sezione di Trieste, I-34127 Trieste, Italy*
[32] *Embry-Riddle Aeronautical University, Prescott, AZ 86301, USA*
[33] *Université de Paris, CNRS, Astroparticule et Cosmologie, F-75006 Paris, France*
[34] *Institute for Cosmic Ray Research (ICRR), KAGRA Observatory, The University of Tokyo, Kashiwa City, Chiba 277-8582, Japan*
[35] *Accelerator Laboratory, High Energy Accelerator Research Organization (KEK), Tsukuba City, Ibaraki 305-0801, Japan*
[36] *Earthquake Research Institute, The University of Tokyo, Bunkyo-ku, Tokyo 113-0032, Japan*
[37] *California State University Fullerton, Fullerton, CA 92831, USA*
[38] *Université Paris-Saclay, CNRS/IN2P3, IJCLab, 91405 Orsay, France*
[39] *European Gravitational Observatory (EGO), I-56021 Cascina, Pisa, Italy*
[40] *Chennai Mathematical Institute, Chennai 603103, India*
[41] *Department of Mathematics and Physics, Gravitational Wave Science Project, Hirosaki University, Hirosaki City, Aomori 036-8561, Japan*
[42] *Columbia University, New York, NY 10027, USA*
[43] *Kamioka Branch, National Astronomical Observatory of Japan (NAOJ), Kamioka-cho, Hida City, Gifu 506-1205, Japan*
[44] *The Graduate University for Advanced Studies (SOKENDAI), Mitaka City, Tokyo 181-8588, Japan*
[45] *Università degli Studi di Urbino "Carlo Bo", I-61029 Urbino, Italy*
[46] *INFN, Sezione di Firenze, I-50019 Sesto Fiorentino, Firenze, Italy*
[47] *INFN, Sezione di Roma, I-00185 Roma, Italy*
[48] *Université catholique de Louvain, B-1348 Louvain-la-Neuve, Belgium*
[49] *Nikhef, Science Park 105, 1098 XG Amsterdam, Netherlands*
[50] *King's College London, University of London, London WC2R 2LS, United Kingdom*
[51] *Korea Institute of Science and Technology Information (KISTI), Yuseong-gu, Daejeon 34141, Korea*
[52] *National Institute for Mathematical Sciences, Yuseong-gu, Daejeon 34047, Korea*
[53] *Christopher Newport University, Newport News, VA 23606, USA*
[54] *International College, Osaka University, Toyonaka City, Osaka 560-0043, Japan*
[55] *School of High Energy Accelerator Science, The Graduate University for Advanced Studies (SOKENDAI), Tsukuba City, Ibaraki 305-0801, Japan*
[56] *University of Oregon, Eugene, OR 97403, USA*
[57] *Syracuse University, Syracuse, NY 13244, USA*
[58] *Université de Liège, B-4000 Liège, Belgium*
[59] *University of Minnesota, Minneapolis, MN 55455, USA*
[60] *Università degli Studi di Milano-Bicocca, I-20126 Milano, Italy*
[61] *INFN, Sezione di Milano-Bicocca, I-20126 Milano, Italy*
[62] *INAF, Osservatorio Astronomico di Brera sede di Merate, I-23807 Merate, Lecco, Italy*
[63] *LIGO Hanford Observatory, Richland, WA 99352, USA*
[64] *Dipartimento di Medicina, Chirurgia e Odontoiatria "Scuola Medica Salernitana", Università di Salerno, I-84081 Baronissi, Salerno, Italy*
[65] *SUPA, University of Glasgow, Glasgow G12 8QQ, United Kingdom*
[66] *LIGO Laboratory, Massachusetts Institute of Technology, Cambridge, MA 02139, USA*
[67] *Wigner RCP, RMKI, H-1121 Budapest, Konkoly Thege Miklós út 29-33, Hungary*
[68] *University of Florida, Gainesville, FL 32611, USA*
[69] *Stanford University, Stanford, CA 94305, USA*
[70] *Università di Pisa, I-56127 Pisa, Italy*
[71] *INFN, Sezione di Perugia, I-06123 Perugia, Italy*
[72] *Università di Perugia, I-06123 Perugia, Italy*
[73] *Università di Padova, Dipartimento di Fisica e Astronomia, I-35131 Padova, Italy*
[74] *INFN, Sezione di Padova, I-35131 Padova, Italy*
[75] *Montana State University, Bozeman, MT 59717, USA*
[76] *Institute for Plasma Research, Bhat, Gandhinagar 382428, India*
[77] *Nicolaus Copernicus Astronomical Center, Polish Academy of Sciences, 00-716, Warsaw, Poland*
[78] *Dipartimento di Ingegneria, Università del Sannio, I-82100 Benevento, Italy*
[79] *OzGrav, University of Adelaide, Adelaide, South Australia 5005, Australia*
[80] *California State University, Los Angeles, 5151 State University Dr, Los Angeles, CA 90032, USA*
[81] *INFN, Sezione di Genova, I-16146 Genova, Italy*
[82] *OzGrav, University of Western Australia, Crawley, Western Australia 6009, Australia*
[83] *RRCAT, Indore, Madhya Pradesh 452013, India*
[84] *GRAPPA, Anton Pannekoek Institute for Astronomy and Institute for High-Energy Physics, University of Amsterdam, Science Park 904, 1098 XH Amsterdam, Netherlands*
[85] *Missouri University of Science and Technology, Rolla, MO 65409, USA*
[86] *Faculty of Physics, Lomonosov Moscow State University, Moscow 119991, Russia*
[87] *Università di Trento, Dipartimento di Fisica, I-38123 Povo, Trento, Italy*
[88] *INFN, Trento Institute for Fundamental Physics and Applications, I-38123 Povo, Trento, Italy*
[89] *SUPA, University of the West of Scotland, Paisley PA1 2BE, United Kingdom*

[90] *Bar-Ilan University, Ramat Gan, 5290002, Israel*
[91] *Artemis, Université Côte d'Azur, Observatoire de la Côte d'Azur, CNRS, F-06304 Nice, France*
[92] *Dipartimento di Fisica "E.R. Caianiello", Università di Salerno, I-84084 Fisciano, Salerno, Italy*
[93] *INFN, Sezione di Napoli, Gruppo Collegato di Salerno, Complesso Universitario di Monte S. Angelo, I-80126 Napoli, Italy*
[94] *Università di Roma "La Sapienza", I-00185 Roma, Italy*
[95] *Univ Rennes, CNRS, Institut FOTON - UMR6082, F-3500 Rennes, France*
[96] *Indian Institute of Technology Bombay, Powai, Mumbai 400 076, India*
[97] *INFN, Laboratori Nazionali del Gran Sasso, I-67100 Assergi, Italy*
[98] *Laboratoire Kastler Brossel, Sorbonne Université, CNRS, ENS-Université PSL, Collège de France, F-75005 Paris, France*
[99] *Astronomical Observatory Warsaw University, 00-478 Warsaw, Poland*
[100] *University of Maryland, College Park, MD 20742, USA*
[101] *Max Planck Institute for Gravitational Physics (Albert Einstein Institute), D-14476 Potsdam, Germany*
[102] *L2IT, Laboratoire des 2 Infinis - Toulouse, Université de Toulouse, CNRS/IN2P3, UPS, F-31062 Toulouse Cedex 9, France*
[103] *School of Physics, Georgia Institute of Technology, Atlanta, GA 30332, USA*
[104] *IGFAE, Campus Sur, Universidade de Santiago de Compostela, 15782 Spain*
[105] *The Chinese University of Hong Kong, Shatin, NT, Hong Kong*
[106] *Stony Brook University, Stony Brook, NY 11794, USA*
[107] *Center for Computational Astrophysics, Flatiron Institute, New York, NY 10010, USA*
[108] *NASA Goddard Space Flight Center, Greenbelt, MD 20771, USA*
[109] *Dipartimento di Fisica, Università degli Studi di Genova, I-16146 Genova, Italy*
[110] *Institute for Gravitational and Subatomic Physics (GRASP), Utrecht University, Princetonplein 1, 3584 CC Utrecht, Netherlands*
[111] *RESCEU, University of Tokyo, Tokyo, 113-0033, Japan.*
[112] *Department of Astronomy, Beijing Normal University, Beijing 100875, China*
[113] *OzGrav, University of Melbourne, Parkville, Victoria 3010, Australia*
[114] *Università degli Studi di Sassari, I-07100 Sassari, Italy*
[115] *INFN, Laboratori Nazionali del Sud, I-95125 Catania, Italy*
[116] *Università di Roma Tor Vergata, I-00133 Roma, Italy*
[117] *INFN, Sezione di Roma Tor Vergata, I-00133 Roma, Italy*
[118] *University of Sannio at Benevento, I-82100 Benevento, Italy and INFN, Sezione di Napoli, I-80100 Napoli, Italy*
[119] *Villanova University, 800 Lancaster Ave, Villanova, PA 19085, USA*
[120] *Departamento de Astronomía y Astrofísica, Universitat de València, E-46100 Burjassot, València, Spain*
[121] *Universität Hamburg, D-22761 Hamburg, Germany*
[122] *Rochester Institute of Technology, Rochester, NY 14623, USA*
[123] *National Tsing Hua University, Hsinchu City, 30013 Taiwan, Republic of China*
[124] *Department of Applied Physics, Fukuoka University, Jonan, Fukuoka City, Fukuoka 814-0180, Japan*
[125] *OzGrav, Charles Sturt University, Wagga Wagga, New South Wales 2678, Australia*
[126] *Department of Physics, Tamkang University, Danshui Dist., New Taipei City 25137, Taiwan*
[127] *Department of Physics and Institute of Astronomy, National Tsing Hua University, Hsinchu 30013, Taiwan*
[128] *Department of Physics, Center for High Energy and High Field Physics, National Central University, Zhongli District, Taoyuan City 32001, Taiwan*
[129] *CaRT, California Institute of Technology, Pasadena, CA 91125, USA*
[130] *Department of Physics, National Tsing Hua University, Hsinchu 30013, Taiwan*
[131] *Dipartimento di Ingegneria Industriale (DIIN), Università di Salerno, I-84084 Fisciano, Salerno, Italy*
[132] *Institute of Physics, Academia Sinica, Nankang, Taipei 11529, Taiwan*
[133] *Université Lyon, Université Claude Bernard Lyon 1, CNRS, IP2I Lyon / IN2P3, UMR 5822, F-69622 Villeurbanne, France*
[134] *Seoul National University, Seoul 08826, South Korea*
[135] *Pusan National University, Busan 46241, South Korea*
[136] *INAF, Osservatorio Astronomico di Padova, I-35122 Padova, Italy*
[137] *University of Arizona, Tucson, AZ 85721, USA*
[138] *Rutherford Appleton Laboratory, Didcot OX11 0DE, United Kingdom*
[139] *OzGrav, Swinburne University of Technology, Hawthorn VIC 3122, Australia*
[140] *Université libre de Bruxelles, Avenue Franklin Roosevelt 50 - 1050 Bruxelles, Belgium*
[141] *Universitat de les Illes Balears, IAC3—IEEC, E-07122 Palma de Mallorca, Spain*
[142] *Université Libre de Bruxelles, Brussels 1050, Belgium*
[143] *Departamento de Matemáticas, Universitat de València, E-46100 Burjassot, València, Spain*
[144] *Texas Tech University, Lubbock, TX 79409, USA*

[145] The Pennsylvania State University, University Park, PA 16802, USA
[146] University of Rhode Island, Kingston, RI 02881, USA
[147] The University of Texas Rio Grande Valley, Brownsville, TX 78520, USA
[148] Bellevue College, Bellevue, WA 98007, USA
[149] Scuola Normale Superiore, Piazza dei Cavalieri, 7 - 56126 Pisa, Italy
[150] MTA-ELTE Astrophysics Research Group, Institute of Physics, Eötvös University, Budapest 1117, Hungary
[151] Maastricht University, P.O. Box 616, 6200 MD Maastricht, Netherlands
[152] University of Portsmouth, Portsmouth, PO1 3FX, United Kingdom
[153] The University of Sheffield, Sheffield S10 2TN, United Kingdom
[154] Université Lyon, Université Claude Bernard Lyon 1,
CNRS, Laboratoire des Matériaux Avancés (LMA),
IP2I Lyon / IN2P3, UMR 5822, F-69622 Villeurbanne, France
[155] Dipartimento di Scienze Matematiche, Fisiche e Informatiche, Università di Parma, I-43124 Parma, Italy
[156] INFN, Sezione di Milano Bicocca, Gruppo Collegato di Parma, I-43124 Parma, Italy
[157] Physik-Institut, University of Zurich, Winterthurerstrasse 190, 8057 Zurich, Switzerland
[158] University of Chicago, Chicago, IL 60637, USA
[159] Université de Strasbourg, CNRS, IPHC UMR 7178, F-67000 Strasbourg, France
[160] West Virginia University, Morgantown, WV 26506, USA
[161] Montclair State University, Montclair, NJ 07043, USA
[162] Colorado State University, Fort Collins, CO 80523, USA
[163] Institute for Nuclear Research, Hungarian Academy of Sciences, Bem t'er 18/c, H-4026 Debrecen, Hungary
[164] Department of Physics, University of Texas, Austin, TX 78712, USA
[165] CNR-SPIN, c/o Università di Salerno, I-84084 Fisciano, Salerno, Italy
[166] Scuola di Ingegneria, Università della Basilicata, I-85100 Potenza, Italy
[167] Observatori Astronòmic, Universitat de València, E-46980 Paterna, València, Spain
[168] The University of Utah, Salt Lake City, UT 84112, USA
[169] Kenyon College, Gambier, OH 43022, USA
[170] Vrije Universiteit Amsterdam, 1081 HV, Amsterdam, Netherlands
[171] Department of Astronomy, The University of Tokyo, Mitaka City, Tokyo 181-8588, Japan
[172] Faculty of Engineering, Niigata University, Nishi-ku, Niigata City, Niigata 950-2181, Japan
[173] International Centre for Theoretical Sciences, Tata Institute of Fundamental Research, Bengaluru 560089, India
[174] State Key Laboratory of Magnetic Resonance and Atomic and Molecular Physics,
Innovation Academy for Precision Measurement Science and Technology (APM),
Chinese Academy of Sciences, Xiao Hong Shan, Wuhan 430071, China
[175] University of Szeged, Dóm tér 9, Szeged 6720, Hungary
[176] Universiteit Gent, B-9000 Gent, Belgium
[177] Cornell University, Ithaca, NY 14850, USA
[178] University of British Columbia, Vancouver, BC V6T 1Z4, Canada
[179] Tata Institute of Fundamental Research, Mumbai 400005, India
[180] INAF, Osservatorio Astronomico di Capodimonte, I-80131 Napoli, Italy
[181] The University of Mississippi, University, MS 38677, USA
[182] University of Michigan, Ann Arbor, MI 48109, USA
[183] Texas A&M University, College Station, TX 77843, USA
[184] Department of Physics, Ulsan National Institute of Science and Technology (UNIST), Ulju-gun, Ulsan 44919, Korea
[185] Applied Research Laboratory, High Energy Accelerator Research Organization (KEK), Tsukuba City, Ibaraki 305-0801, Japan
[186] Dipartimento di Fisica, Università di Trieste, I-34127 Trieste, Italy
[187] Shanghai Astronomical Observatory, Chinese Academy of Sciences, Shanghai 200030, China
[188] American University, Washington, D.C. 20016, USA
[189] Faculty of Science, University of Toyama, Toyama City, Toyama 930-8555, Japan
[190] Institute for Cosmic Ray Research (ICRR), KAGRA Observatory,
The University of Tokyo, Kamioka-cho, Hida City, Gifu 506-1205, Japan
[191] Carleton College, Northfield, MN 55057, USA
[192] University of California, Berkeley, CA 94720, USA
[193] Maastricht University, 6200 MD, Maastricht, Netherlands
[194] College of Industrial Technology, Nihon University, Narashino City, Chiba 275-8575, Japan
[195] Graduate School of Science and Technology, Niigata University, Nishi-ku, Niigata City, Niigata 950-2181, Japan
[196] Department of Physics and Astronomy, Haverford College,
370 Lancaster Avenue, Haverford, PA 19041, USA
[197] Department of Physics, National Taiwan Normal University, sec. 4, Taipei 116, Taiwan
[198] Astronomy & Space Science, Chungnam National University, Yuseong-gu, Daejeon 34134, Korea, Korea
[199] Department of Physics and Mathematics, Aoyama Gakuin University, Sagamihara City, Kanagawa 252-5258, Japan
[200] Kavli Institute for Astronomy and Astrophysics,
Peking University, Haidian District, Beijing 100871, China

[201] *Yukawa Institute for Theoretical Physics (YITP), Kyoto University, Sakyou-ku, Kyoto City, Kyoto 606-8502, Japan*
[202] *Graduate School of Science and Engineering, University of Toyama, Toyama City, Toyama 930-8555, Japan*
[203] *Department of Physics, Graduate School of Science, Osaka City University, Sumiyoshi-ku, Osaka City, Osaka 558-8585, Japan*
[204] *Nambu Yoichiro Institute of Theoretical and Experimental Physics (NITEP), Osaka City University, Sumiyoshi-ku, Osaka City, Osaka 558-8585, Japan*
[205] *Institute of Space and Astronautical Science (JAXA), Chuo-ku, Sagamihara City, Kanagawa 252-0222, Japan*
[206] *Directorate of Construction, Services & Estate Management, Mumbai 400094, India*
[207] *Vanderbilt University, Nashville, TN 37235, USA*
[208] *Universiteit Antwerpen, Prinsstraat 13, 2000 Antwerpen, Belgium*
[209] *University of Białystok, 15-424 Białystok, Poland*
[210] *Department of Physics, Ewha Womans University, Seodaemun-gu, Seoul 03760, Korea*
[211] *National Astronomical Observatories, Chinese Academic of Sciences, Chaoyang District, Beijing, China*
[212] *School of Astronomy and Space Science, University of Chinese Academy of Sciences, Chaoyang District, Beijing, China*
[213] *University of Southampton, Southampton SO17 1BJ, United Kingdom*
[214] *Institute for Cosmic Ray Research (ICRR), The University of Tokyo, Kashiwa City, Chiba 277-8582, Japan*
[215] *Chung-Ang University, Seoul 06974, South Korea*
[216] *Institut de Física d'Altes Energies (IFAE), Barcelona Institute of Science and Technology, and ICREA, E-08193 Barcelona, Spain*
[217] *Graduate School of Science, Tokyo Institute of Technology, Meguro-ku, Tokyo 152-8551, Japan*
[218] *University of Washington Bothell, Bothell, WA 98011, USA*
[219] *Institute of Applied Physics, Nizhny Novgorod, 603950, Russia*
[220] *Ewha Womans University, Seoul 03760, South Korea*
[221] *Inje University Gimhae, South Gyeongsang 50834, South Korea*
[222] *Department of Physics, Myongji University, Yongin 17058, Korea*
[223] *Korea Astronomy and Space Science Institute, Daejeon 34055, South Korea*
[224] *National Institute for Mathematical Sciences, Daejeon 34047, South Korea*
[225] *Ulsan National Institute of Science and Technology, Ulsan 44919, South Korea*
[226] *Department of Physical Science, Hiroshima University, Higashihiroshima City, Hiroshima 903-0213, Japan*
[227] *School of Physics and Astronomy, Cardiff University, Cardiff, CF24 3AA, UK*
[228] *Institute of Astronomy, National Tsing Hua University, Hsinchu 30013, Taiwan*
[229] *Bard College, 30 Campus Rd, Annandale-On-Hudson, NY 12504, USA*
[230] *Institute of Mathematics, Polish Academy of Sciences, 00656 Warsaw, Poland*
[231] *National Center for Nuclear Research, 05-400 Świerk-Otwock, Poland*
[232] *Instituto de Fisica Teorica, 28049 Madrid, Spain*
[233] *Department of Physics, Nagoya University, Chikusa-ku, Nagoya, Aichi 464-8602, Japan*
[234] *Université de Montréal/Polytechnique, Montreal, Quebec H3T 1J4, Canada*
[235] *Laboratoire Lagrange, Université Côte d'Azur, Observatoire Côte d'Azur, CNRS, F-06304 Nice, France*
[236] *Department of Physics, Hanyang University, Seoul 04763, Korea*
[237] *Sungkyunkwan University, Seoul 03063, South Korea*
[238] *NAVIER, École des Ponts, Univ Gustave Eiffel, CNRS, Marne-la-Vallée, France*
[239] *Department of Physics, National Cheng Kung University, Tainan City 701, Taiwan*
[240] *National Center for High-performance computing, National Applied Research Laboratories, Hsinchu Science Park, Hsinchu City 30076, Taiwan*
[241] *Institute for High-Energy Physics, University of Amsterdam, Science Park 904, 1098 XH Amsterdam, Netherlands*
[242] *NASA Marshall Space Flight Center, Huntsville, AL 35811, USA*
[243] *University of Washington, Seattle, WA 98195, USA*
[244] *Dipartimento di Matematica e Fisica, Università degli Studi Roma Tre, I-00146 Roma, Italy*
[245] *INFN, Sezione di Roma Tre, I-00146 Roma, Italy*
[246] *ESPCI, CNRS, F-75005 Paris, France*
[247] *Concordia University Wisconsin, Mequon, WI 53097, USA*
[248] *Università di Camerino, Dipartimento di Fisica, I-62032 Camerino, Italy*
[249] *School of Physics Science and Engineering, Tongji University, Shanghai 200092, China*
[250] *Southern University and A&M College, Baton Rouge, LA 70813, USA*
[251] *Centre Scientifique de Monaco, 8 quai Antoine Ier, MC-98000, Monaco*
[252] *Institute for Photon Science and Technology, The University of Tokyo, Bunkyo-ku, Tokyo 113-8656, Japan*
[253] *Indian Institute of Technology Madras, Chennai 600036, India*
[254] *Saha Institute of Nuclear Physics, Bidhannagar, West Bengal 700064, India*

[255] *The Applied Electromagnetic Research Institute, National Institute of Information and Communications Technology (NICT), Koganei City, Tokyo 184-8795, Japan*
[256] *Institut des Hautes Etudes Scientifiques, F-91440 Bures-sur-Yvette, France*
[257] *Faculty of Law, Ryukoku University, Fushimi-ku, Kyoto City, Kyoto 612-8577, Japan*
[258] *Indian Institute of Science Education and Research, Kolkata, Mohanpur, West Bengal 741252, India*
[259] *Department of Astrophysics/IMAPP, Radboud University Nijmegen, P.O. Box 9010, 6500 GL Nijmegen, Netherlands*
[260] *Department of Physics, University of Notre Dame, Notre Dame, IN 46556, USA*
[261] *Consiglio Nazionale delle Ricerche - Istituto dei Sistemi Complessi, Piazzale Aldo Moro 5, I-00185 Roma, Italy*
[262] *Korea Astronomy and Space Science Institute (KASI), Yuseong-gu, Daejeon 34055, Korea*
[263] *Hobart and William Smith Colleges, Geneva, NY 14456, USA*
[264] *International Institute of Physics, Universidade Federal do Rio Grande do Norte, Natal RN 59078-970, Brazil*
[265] *Museo Storico della Fisica e Centro Studi e Ricerche "Enrico Fermi", I-00184 Roma, Italy*
[266] *Lancaster University, Lancaster LA1 4YW, United Kingdom*
[267] *Università di Trento, Dipartimento di Matematica, I-38123 Povo, Trento, Italy*
[268] *Indian Institute of Science Education and Research, Pune, Maharashtra 411008, India*
[269] *Dipartimento di Fisica, Università degli Studi di Torino, I-10125 Torino, Italy*
[270] *Indian Institute of Technology, Palaj, Gandhinagar, Gujarat 382355, India*
[271] *Department of Physics, Kyoto University, Sakyou-ku, Kyoto City, Kyoto 606-8502, Japan*
[272] *Department of Electronic Control Engineering, National Institute of Technology, Nagaoka College, Nagaoka City, Niigata 940-8532, Japan*
[273] *Departamento de Matemática da Universidade de Aveiro and Centre for Research and Development in Mathematics and Applications, Campus de Santiago, 3810-183 Aveiro, Portugal*
[274] *Marquette University, 11420 W. Clybourn St., Milwaukee, WI 53233, USA*
[275] *Graduate School of Science and Engineering, Hosei University, Koganei City, Tokyo 184-8584, Japan*
[276] *Faculty of Science, Toho University, Funabashi City, Chiba 274-8510, Japan*
[277] *Faculty of Information Science and Technology, Osaka Institute of Technology, Hirakata City, Osaka 573-0196, Japan*
[278] *Università di Firenze, Sesto Fiorentino I-50019, Italy*
[279] *INAF, Osservatorio Astrofisico di Arcetri, Largo E. Fermi 5, I-50125 Firenze, Italy*
[280] *Indian Institute of Technology Hyderabad, Sangareddy, Khandi, Telangana 502285, India*
[281] *iTHEMS (Interdisciplinary Theoretical and Mathematical Sciences Program), The Institute of Physical and Chemical Research (RIKEN), Wako, Saitama 351-0198, Japan*
[282] *INAF, Osservatorio di Astrofisica e Scienza dello Spazio, I-40129 Bologna, Italy*
[283] *Department of Space and Astronautical Science, The Graduate University for Advanced Studies (SOKENDAI), Sagamihara City, Kanagawa 252-5210, Japan*
[284] *Andrews University, Berrien Springs, MI 49104, USA*
[285] *Research Center for Space Science, Advanced Research Laboratories, Tokyo City University, Setagaya, Tokyo 158-0082, Japan*
[286] *Institute for Cosmic Ray Research (ICRR), Research Center for Cosmic Neutrinos (RCCN), The University of Tokyo, Kashiwa City, Chiba 277-8582, Japan*
[287] *National Metrology Institute of Japan, National Institute of Advanced Industrial Science and Technology, Tsukuba City, Ibaraki 305-8568, Japan*
[288] *Dipartimento di Scienze Aziendali - Management and Innovation Systems (DISA-MIS), Università di Salerno, I-84084 Fisciano, Salerno, Italy*
[289] *Van Swinderen Institute for Particle Physics and Gravity, University of Groningen, Nijenborgh 4, 9747 AG Groningen, Netherlands*
[290] *Faculty of Science, Department of Physics, The Chinese University of Hong Kong, Shatin, N.T., Hong Kong*
[291] *Vrije Universiteit Brussel, Boulevard de la Plaine 2, 1050 Ixelles, Belgium*
[292] *Department of Communications Engineering, National Defense Academy of Japan, Yokosuka City, Kanagawa 239-8686, Japan*
[293] *Department of Physics, University of Florida, Gainesville, FL 32611, USA*
[294] *Department of Information and Management Systems Engineering, Nagaoka University of Technology, Nagaoka City, Niigata 940-2188, Japan*
[295] *Vrije Universiteit Amsterdam, 1081 HV Amsterdam, Netherlands*
[296] *Department of Physics and Astronomy, Sejong University, Gwangjin-gu, Seoul 143-747, Korea*
[297] *Department of Electrophysics, National Chiao Tung University, Hsinchu, Taiwan*
[298] *Department of Physics, Rikkyo University, Toshima-ku, Tokyo 171-8501, Japan*
[299] *School of Physics and Astronomy, University of Southampton, Southampton, SO17 1B J, United Kingdom*
[300] *Astrophysics Science Division, NASA Goddard Space Flight Center, Greenbelt, MD 20771, USA*
[301] *Department of Astronomy, University of Maryland, College Park, MD 20742, USA*
[302] *MIT Kavli Institute for Astrophysics and Space Research, Massachusetts Institute of Technology, Cambridge, MA 02139, USA*
[303] *Space Science Division, U.S. Naval Research Laboratory, Washington, DC 20375, USA*

[304] *Dipartimento di Fisica, Università degli Studi di Cagliari, SP Monserrato-Sestu km 0.7, 09042 Monserrato, Italy*
[305] *Astrophysics Science Division and Joint Space-Science Institute, NASA Goddard Space Flight Center, Greenbelt, MD 20771, USA*

Results are presented of searches for continuous gravitational waves from 20 accreting millisecond X-ray pulsars with accurately measured spin frequencies and orbital parameters, using data from the third observing run of the Advanced LIGO and Advanced Virgo detectors. The search algorithm uses a hidden Markov model, where the transition probabilities allow the frequency to wander according to an unbiased random walk, while the $\mathcal{J}$-statistic maximum-likelihood matched filter tracks the binary orbital phase. Three narrow sub-bands are searched for each target, centered on harmonics of the measured spin frequency. The search yields 16 candidates, consistent with a false alarm probability of 30% per sub-band and target searched. These candidates, along with one candidate from an additional target-of-opportunity search done for SAX J1808.4−3658, which was in outburst during one month of the observing run, cannot be confidently associated with a known noise source. Additional follow-up does not provide convincing evidence that any are a true astrophysical signal. When all candidates are assumed non-astrophysical, upper limits are set on the maximum wave strain detectable at 95% confidence, $h_0^{95\%}$. The strictest constraint is $h_0^{95\%} = 4.7 \times 10^{-26}$ from IGR J17062−6143. Constraints on the detectable wave strain from each target lead to constraints on neutron star ellipticity and r-mode amplitude, the strictest of which are $\epsilon^{95\%} = 3.1 \times 10^{-7}$ and $\alpha^{95\%} = 1.8 \times 10^{-5}$ respectively. This analysis is the most comprehensive and sensitive search of continuous gravitational waves from accreting millisecond X-ray pulsars to date.

I. INTRODUCTION

Second generation, ground-based gravitational wave detectors, specifically the Advanced Laser Interferometer Gravitational wave Observatory (Advanced LIGO) [1] and Advanced Virgo [2], have detected more than 50 compact binary coalescence events in recent years [3–5]. Continuous gravitational waves from rapidly-rotating neutron stars are also potential sources, e.g. a non-axisymmetry due to mountains on the surface, or stellar oscillation modes in the interior [6–8]. There are no reported detections of continuous gravitational waves to date, despite a number of searches in Advanced LIGO and Advanced Virgo data [9–30].

Low-mass X-ray binaries (LMXBs) are a high-priority target for continuous gravitational wave searches. LMXBs are composed of a compact object, such as a neutron star[1], which accretes matter from a stellar-mass ($\lesssim 1 M_\odot$) companion [31]. The accretion exerts a torque that may spin up the compact object. Electromagnetic (EM) observations show that even the pulsar with the highest known frequency, PSR J1748−2446ad at 716 Hz [32], rotates well below the centrifugal break-up frequency, estimated at ~ 1400 Hz [33]. Gravitational wave emission may provide the balancing torque in binary systems such as these, stopping the neutron star from spinning up to the break-up frequency [34, 35]. If so, there should thus be a correlation between accretion rate (which is inferred via X-ray flux) and the strength of the continuous gravitational wave emission [34–37]. The LMXB Scorpius X-1 is the brightest extra-Solar X-ray source in the sky, making it a prime target for searches for continuous gravitational waves [11, 18, 38, 39].

Some LMXBs have EM observations of pulsations during "outburst" events lasting days to months, which allow for measurement of their rotational frequency, $f_\star$, to an accuracy of $\sim 10^{-8}$ Hz, and measurement of their binary ephemerides [31, 40]. LMXBs that are observed to go into outburst and have measurable pulsations with millisecond periods are sometimes called accreting millisecond X-ray pulsars (AMXPs). If the rotational frequency is known, computationally cheap narrowband searches are possible. Six AMXPs were previously searched for continuous gravitational waves, one in Science Run 6 (S6) using the TwoSpect algorithm [41, 42], and five in Observing Run 2 (O2) using the same Hidden Markov Model (HMM) algorithm we use in this work [12, 43]. No significant candidates were found in either search. Searches for continuous gravitational waves from LMXBs are difficult as the rotation frequency may wander stochastically on timescales of $\lesssim 1$ yr [44], limiting the duration of coherent integration. A HMM tracks a wandering signal, and is the search algorithm we use here, following Refs. [11, 12, 43, 45].

Advanced LIGO and Advanced Virgo began the third Observing Run (O3) on April 1 2019, 15:00 UTC. There was a month-long commissioning break between October 1 2019, 15:00 UTC, and November 1 2019, 15:00 UTC, after which observations resumed until March 27, 2020, 17:00 UTC. This month-long break divides O3 into two segments: O3a and O3b. In this work we search the full O3 data set for continuous gravitational wave signals from AMXPs with known rotational frequencies. The search is a more sensitive version of an analogous search in O2 data [12], with an expanded target list. We briefly review the algorithm and O2 search in Sec. II. In Secs. III and IV we describe the targets and the parame-

* Deceased, August 2020.
[1] LMXBs in which the compact object is a stellar-mass black hole are not expected to function as continuous gravitational wave sources and are not discussed in this paper.

ter space respectively. We discuss the data used in Sec. V. In Sec. VI we describe the vetoes applied to discriminate between terrestrial and astrophysical candidates. In Sec. VII we present the results of the search. In Sec. VIII we describe an additional target-of-opportunity search performed for one of the targets that was in outburst during O3a. We provide upper limits for the detectable wave-strain, and astrophysical implications thereof, in Sec. IX. We conclude in Sec. X.

II. SEARCH ALGORITHM

The search in this paper follows the same prescription as the O2 searches for Scorpius X-1 [11] and LMXBs with known rotational frequency [12]. It is composed of two parts: a HMM which uses the Viterbi algorithm to efficiently track the most likely spin history, and the $\mathcal{J}$-statistic, which calculates the likelihood a gravitational wave is present given the detector data, and the orbital parameters of both the Earth and the LMXB. The HMM formalism is identical to that used in Refs. [11, 12, 38, 43, 45], and the $\mathcal{J}$-statistic was first introduced in Ref. [43]. Below, we provide a brief review of both the HMM and the $\mathcal{J}$-statistic.

A. HMM

In a Markov process, the probability of finding the system in the current state depends only on the previous state. In a hidden Markov process the states are not directly observable and must be inferred from noisy data. In this paper, the hidden state of interest is the gravitational wave frequency $f(t)$. Although the rotation frequency $f_\star(t)$ of every target in this search is measured accurately from EM pulsations, we allow $f(t) \neq f_\star(t)$ in general for three reasons: i) different emission mechanisms emit at different multiples of $f_\star$ [46]; ii) a small, fluctuating drift may arise between $f(t)$ and $f_\star(t)$, if the star's core (where the gravitational-wave-emitting mass or current quadrupole may reside) decouples partially from the crust (to which EM pulsations are locked) [45, 47]; and, iii) the rotational frequency of the crust may also drift stochastically due to a fluctuating accretion torque [31, 44]. The gravitational-wave frequency is therefore hidden even though the EM measurement of $f_\star$ helps restrict the searched frequency space, as described in Sec. IV.

Following the notation of Refs. [11, 12] we label the hidden state variable as $q(t)$. In our model, it transitions between a discrete set of allowed values $\{q_1, ..., q_{N_Q}\}$ at discrete times $\{t_0, ..., t_{N_T}\}$. The probability of the state transitioning from q_i at time t_n to q_j at time t_{n+1} is determined by the transition matrix $A_{q_j q_i}$. In this search, as in previous searches of LMXBs [11, 12, 38], the transition matrix is

$$A_{q_j q_i} = \frac{1}{3}\left(\delta_{q_j q_{i+1}} + \delta_{q_j q_i} + \delta_{q_j q_{i-1}}\right) , \tag{1}$$

where δ_{ij} is the Kronecker delta. Eq. (1) corresponds to allowing $f(t)$ to move 0, or ± 1 frequency bins, with equal probability, at each discrete transition. It implicitly defines the signal model for $f(t)$ to be a piece-wise constant function, with jumps in frequency allowed at the discrete times $\{t_0, ..., t_{N_T}\}$. This is a well-tested approximation for an unbiased random walk [43, 45].

The total duration of the search is $T_{\rm obs}$, which we split into N_T coherent equal chunks of length $T_{\rm drift}$, where $N_T = \lfloor T_{\rm obs}/T_{\rm drift} \rfloor$, and $\lfloor ... \rfloor$ indicates rounding down to the nearest integer. We justify our choice of $T_{\rm drift}$ in Sec. IV. In essence, it needs to be short enough to ensure that $f_\star(t)$ does not wander by more than one frequency bin during each time segment, but ideally no shorter in order to maximize the signal-to-noise ratio in each segment. For each time segment the likelihood that the observation o_j is related to the hidden state q_i is given by the emission matrix $L_{o_j q_i}$. We calculate $L_{o_j q_i}$ from the data via a frequency domain estimator, e.g. the $\mathcal{J}$-statistic, as discussed in Sec. II B.

The probability that the hidden path is $Q = \{q(t_0), ..., q(t_{N_T})\}$ given a set of observations $O = \{o(t_0), ..., o(t_{N_T})\}$ is

$$\begin{aligned} P(Q\,|\,O) = \Pi_{q(t_0)}\, A_{q(t_1)q(t_0)} L_{o(t_1)q(t_1)} \ \cdots \\ \times A_{q(t_{N_T})q(t_{N_T-1})} L_{o(t_{N_T})q(t_{N_T})} \ , \end{aligned} \tag{2}$$

where $\Pi_{q(t_0)}$ is the prior probability of starting in the state $q(t_0)$, and is taken to be uniform within a certain range guided by EM measurements of $f_\star$. The Viterbi algorithm is a computationally efficient way to find the path Q^* that maximizes Eq. (2) [48].

The detection statistic we use in this work is $\mathcal{L} = \ln P(Q^*\,|\,O)$, i.e. the log-likelihood of the most likely path given the data. The search outputs one $P(Q^*|O)$ value per frequency bin, corresponding to the optimal path Q^* terminating in that frequency bin.

B. $\mathcal{J}$-statistic

Any long-lived gravitational wave signal from an LMXB observed by the detectors is Doppler modulated by the orbital motion of the detectors around the Solar System barycenter, and by the orbital motion of the compact object in its binary. The $\mathcal{F}$-statistic is a frequency domain estimator originally designed for isolated neutron stars, and accounts for the Earth's annual orbital motion (as well as the amplitude modulation caused by the Earth's diurnal rotation) [49]. Algorithms that implement the $\mathcal{F}$-statistic, such as `lalapps_ComputeFstatistic_v2` [50], have subsequently added functionality to account for modulation of the signal due to binary motion.

The $\mathcal{J}$-statistic accounts for the binary modulation via a Jacobi-Anger expansion of the orbit [43]. It ingests $\mathcal{F}$-statistic "atoms" as calculated for an isolated source as an input, assumes the binary is in a circular orbit[2], and requires three binary orbital parameters: the period P, the projected semi-major axis a_0, and the time of passage of the ascending node $T_{\rm asc}$. We use the $\mathcal{J}$-statistic as the frequency domain estimator $L_{o_j q_i}$ in this paper, as in Refs. [11, 12]. The $\mathcal{J}$-statistic is a computationally efficient algorithm, as it re-uses $\mathcal{F}$-statistic atoms when searching over a template bank of binary orbital parameters.

III. TARGETS

The AMXPs chosen as targets for this search, along with their positions, orbital elements, and pulsation frequencies are listed in Table I. These 20 targets constitute all known AMXPs with observed coherent pulsations and precisely measured orbital elements as of April 2021[3]. For details on the relevant EM observations, principally in the X-ray band, see Refs. [31, 40, 53, 54].

Most AMXPs are transient, with "active" (outburst) and "quiescent" phases. Pulsations, and therefore $f_\star$, are only observed during the active phase. Active phases are typically associated with accretion onto the neutron star, however accretion can also happen during quiescence [55]. The frequency derivatives, $\dot{f}_\star$, in the active phase and in the quiescent phase are set by the accretion torque and magnetic dipole braking respectively [55, 56]. The value of $\dot{f}_\star$ has implications for the continuous gravitational wave signal strength (see Sec. IX C), as well as the choice of $T_{\rm drift}$ (see Sec. IV A).

One target, SAX J1808.4−3658, went into outburst during O3a [57–59]. It may be the case that continuous gravitational waves are only emitted when an AMXP is in outburst [60]. If so, we increase our signal-to-noise ratio by searching only data from the times that it was in outburst, compared to searching the entirety of O3 data. To investigate this possibility, we perform in Sec. VIII an additional target-of-opportunity search for continuous gravitational waves from SAX J1808.4−3658 while it is in outburst.

[2] This assumption is justified as none of the targets described in Sec. III have measurable eccentricity with sufficient precision [31, 40].

[3] We do not include the AMXP Aquila X-1 [51, 52] in our target list as there is a large uncertainty on all three binary orbital elements, compared to the other 20 AMXPs. One would need to search $> 10^{10}$ binary orbital templates, an order of magnitude more than the rest of the targets combined. The number of binary orbital templates is calculated as a function of the uncertainty in orbital elements in Sec. IV B.

IV. SEARCH PARAMETERS

The $\mathcal{J}$-statistic matched filter requires specification of the source sky position [right ascension (RA) and declination (Dec)], the orbital period P, the projected semi-major axis a_0, and the orbital phase ϕ_a at the start of the search. The orbital phase can be equivalently specified via a time of passage through the ascending node, $T_{\rm asc}$. EM observations constrain all of these parameters, as well as the spin frequency $f_\star$. These measurements, along with their associated uncertainties, are listed in Table I.

There are several mechanisms that could lead to continuous gravitational wave emission from an AMXP, in its active or quiescent phase. "Mountains" on the neutron star surface, be they magnetically or elastically supported, emit at $2f_\star$ and potentially $f_\star$ [97]. The dominant continuous gravitational wave emission from r-mode oscillations (Rossby waves excited by radiation-reaction instabilities) is predicted to be at $\sim 4f_\star/3$ [98–101]. Thus, we search frequency sub-bands centered on $\{1, 4/3, 2\}\, f_\star$ for each target. As in Refs. [11, 12] we choose a sub-band width of $\sim 0.61\,\mathrm{Hz}$[4].

Recent work indicates that the continuous gravitational wave signal from r-modes could emit at a frequency far from $4f_\star/3$ due to equation-of-state-dependent relativistic corrections, and so comprehensive searches for r-modes may need to cover hundreds of Hz for the targets listed in Table I [103, 104]. The exact range of frequencies to search is a non-linear function of $f_\star$, and does not necessarily include $4f_\star/3$ (see equation (17) of Ref. [104]). However, these estimates are still uncertain. We deliberately search $\sim 0.61\,\mathrm{Hz}$ sub-bands centered on $4f_\star/3$, as an exhaustive broadband search lies outside the scope of this paper, which aims to conduct fast, narrowband searches at astrophysically motivated harmonics of $f_\star$ while accommodating frequency wandering within those sub-bands, a challenge in its own right.

A. $T_{\rm drift}$ and frequency binning

Another key parameter for the search algorithm described in Sec. II is the coherence time $T_{\rm drift}$. As in Refs. [11, 12] we fix $T_{\rm drift} = 10\,\mathrm{d}$ for each target[5]. This choice of $T_{\rm drift}$ is guided by observations of Scorpius X-1 [44]. Quantitative studies of how X-ray flux variability

[4] Other narrowband searches, such as Refs. [10, 102], search sub-bands whose width, $\sim 10^{-3} f$, scales with frequency. We note that 0.61 Hz is comparable to $10^{-3} f$ for the harmonics of $f_\star$ that we search in this paper, but is $2^{20}\Delta f$, where Δf is the frequency bin size defined in Sec. IV A. Having the number of frequency bins in the sub-band equal a power of two speeds up the Fourier transform [11].

[5] We consider additional $T_{\rm drift}$ durations for the target-of-opportunity search for continuous gravitational waves from SAX J1808.4−3658 during its O3a outburst in Sec. VIII.

TABLE I: Target list: position (RA and Dec), orbital period (P), projected semi-major axis in light-seconds (a_0), time of passage through the ascending node as measured near the time of the most recent outburst ($T_{\rm asc}$), the time of passage through the ascending node as propagated to the start of O3 ($T_{\rm asc,\,O3}$), as described in Sec. IV B, and frequency of observed pulsations ($f_\star$). Numbers in parentheses indicate reported 1σ errors (68% confidence level), unless otherwise noted. All objects have positional uncertainty $\leq$ 1s in RA and $\leq 0.5''$ in Dec.

Target	RA	Dec	P/s	a_0/lt-s	$T_{\rm asc}$/GPS time	$T_{\rm asc,\,O3}$/GPS time	$f_\star$/Hz	Refs.
IGR J00291+5934	00h29m03.05s	+59°34′18.93″	8844.07673(9)	0.064993(2)	1122149932.93(5)	1238157687(1)	598.89213099(6)	[61, 62]
MAXI J0911−655	09h12m02.46s	−64°52′06.37″	2659.93312(47)	0.017595(9)	1145507148.0(9)	1238165918(16)	339.9750123(3)	[63, 64]
XTE J0929−314	09h29m20.19s	−31°23′03.2″	2614.746(3)	0.006290(9)	705152406.1(9)	1238165763(612)	185.105254297(9)	[65, 66]
IGR J16597−3704	16h59m32.902s	−37°07′14.3″	2758.2(3)	0.00480(3)	1193053416(9)	1238163777(4907)	105.1758271(3)	[67, 68]
IGR J17062−6143	17h06m16.29s	−61°42′40.6″	2278.21124(2)	0.003963(6)	1239389342(4)	1238165942(4)	163.656110049(9)	[69]
IGR J17379−3747	17h37m58.836s	−37°46′18.35″	6765.8388(17)	0.076979(14)	1206573046.6(3)	1238162748(8)	468.083266605(7)	[70, 71]
SAX J1748.9−2021	17h48m52.161s	−20°21′32.406″	31555.300(3)	0.38757(2)	1109500772.5(8)	1238151731(12)	442.3610957(2)	[40, 72]
NGC 6440 X−2	17h48m52.76s	−20°21′24.0″	3457.8929(7)	0.00614(1)	956797704(2)	1238166449(57)	205.89221(2)	[73, 74]
IGR J17494−3030	17h49m23.62s	−30°29′58.999″	4496.67(3)	0.015186(12)	1287797911(1)	1238163668(331)	376.05017022(4)	[75]
Swift J1749.4−2807	17h49m31.728s	−28°08′05.064″	31740.8417(27)	1.899568(11)	1298634645.85(12)	1238136602(5)	517.92001385(6)	[76–78]
IGR J17498−2921	17h49m56.02s	−29°19′20.7″	13835.619(1)[b]	0.365165(5)[b]	997147537.43(7)[b]	1238164020(6)	400.99018734(9)[b]	[79, 80]
IGR J17511−3057	17h51m08.66s	−30°57′41.0″	12487.5121(4)	0.2751952(18)	936924316.03(3)	1238160570(10)	244.83395145(9)	[81, 82]
XTE J1751−305	17h51m13.49s	−30°37′23.4″	2545.3414(38)[a]	0.010125(5)[a]	701914663.57(3)[a]	1238164644(487)	435.31799357(3)[a]	[83, 84]
Swift J1756.9−2508	17h56m57.43s	−25°06′27.4″	3282.40(4)	0.00596(2)	1207196675(9)	1238166119(378)	182.06580377(11)	[85]
IGR J17591−2342	17h59m02.86s	−23°43′08.3″	31684.7503(5)	1.227714(4)	1218341207.72(8)	1238144176.7(3)	527.425700578(9)	[86, 87]
XTE J1807−294	18h06m59.8s	−29°24′30″	2404.4163(3)	0.004830(3)	732384720.7(3)	1238165711(63)	190.62350702(4)	[88, 89]
SAX J1808.4−3658	18h08m27.647s	−36°58′43.90″	7249.155(3)	0.062809(7)	1250296258.5(2)	1238161173(5)	400.97521037(1)	[58]
XTE J1814−338	18h13m39.02s	−33°46′22.3″	15388.7229(2)[a]	0.390633(9)[a]	739049147.41(8)[a]	1238151597(4)	314.35610879(1)[a]	[90, 91]
IGR J18245−2452	18h24m32.51s	−24°52′07.9″	39692.812(7)	0.76591(1)	1049865088.37(9)	1238128096(33)	254.3330310(1)	[92, 93]
HETE J1900.1−2455	19h00m08.65s	−24°55′13.7″	4995.2630(5)	0.01844(2)	803963262.3(8)	1238161513(43)	377.296171971(5)	[94–96]

[a] 90% confidence level
[b] 3σ error

in AMXPs impacts searches for continuous gravitational waves are absent from the literature. The choice to use $T_{\rm drift} = 10\,\mathrm{d}$ balances the increased sensitivity achieved via longer coherence times with the knowledge that the gravitational wave frequency may wander stochastically, e.g. due to fluctuations in the mass accretion rate. The particular value $T_{\rm drift} = 10\,\mathrm{d}$ has been adopted in all previous Viterbi LMXB searches [11, 12, 38] and is justified approximately with reference to a simple random-walk interpretation of fluctuations in the X-ray flux of Scorpius X-1 [44, 105, 106], but other values are reasonable too.

We remind the reader that the choice of $T_{\rm drift}$ implicitly fixes the proposed signal model as one in which the frequency may wander step-wise zero, plus or minus one frequency bin every $T_{\rm drift} = 10\,\mathrm{d}$. The size of the frequency bins, Δf, is fixed by the resolution implied by the coherence time, i.e. $\Delta f = 1/(2\,T_{\rm drift}) = 5.787037 \times 10^{-7}\,\mathrm{Hz}$, for $T_{\rm drift} = 10\,\mathrm{d}$. As Δf depends on $T_{\rm drift}$, changing the coherence time explicitly changes the signal model, e.g. if $T_{\rm drift}$ is halved and $T_{\rm obs}$ is kept constant, then both N_T and Δf double; thus the signal can move up to a factor of four more in frequency in the same $T_{\rm obs}$. The connection between the coherence time and signal model features in all semi-coherent search methods. However, for a HMM-based search such as this, the choice of coherence time is not limited by computational cost, as it is in all-sky searches or searches based on the $\mathcal{F}$-statistic [17, 107].

This analysis does not search over any frequency derivatives. The maximum absolute frequency derivative, $|\dot{f}_{\rm max}|$, that does not change the frequency more than one frequency bin over the course of one coherent chunk is

$$\left|\dot{f}_{\rm max}\right| = \frac{\Delta f}{T_{\rm drift}} \approx 6.7 \times 10^{-13}\,\mathrm{Hz\,s^{-1}}\,. \tag{3}$$

When measured, the long-term secular frequency derivative is well below this value for all of our targets, see Sec. IX C for details.

B. Number of orbital templates

The orbital elements are known to high precision, with the uncertainty in P satisfying $\sigma_P \lesssim 10^{-3}\,\mathrm{s}$, the uncertainty in a_0 satisfying $\sigma_{a_0} \lesssim 10^{-4}$ light-seconds (lt-s), and the uncertainty in $T_{\rm asc}$ satisfying $\sigma_{T_{\rm asc}} \lesssim 1\,\mathrm{s}$. However, $T_{\rm asc}$ is measured relative to the target's most recent outburst, which is often years before the start of O3 ($T_{\rm O3,\,start} = 1238166483\,\mathrm{GPS\ time}$). We need to propagate it forward in time. This propagation compounds the uncertainty in $T_{\rm asc}$, viz. [11, 12, 39]

$$\sigma_{T_{\rm asc,\,O3}} = \left[\sigma_{T_{\rm asc}}^2 + \left(N_{\rm orb}\sigma_P\right)^2\right]^{1/2}\,, \tag{4}$$

where $N_{\rm orb}$ is the number of orbits between the observed $T_{\rm asc}$ and $T_{\rm asc,\,O3}$. Henceforth $T_{\rm asc}$ and $\sigma_{T_{\rm asc}}$ symbolize their values when propagated to $T_{\rm O3,\,start}$.

To conduct the search over the orbital elements for each target and sub-band we construct a rectangular grid in the parameter space defined by $(P \pm 3\sigma_P, a_0 \pm 3\sigma_{a_0}, T_{\rm asc} \pm 3\sigma_{T_{\rm asc}})$. For three targets, XTE J0929−314, IGR J16597−3704, and IGR J17494−3030, the range $(T_{\rm asc} \pm P/2)$ is smaller than $(T_{\rm asc} \pm 3\sigma_{T_{\rm asc}})$ and we use the former. We assume that P and a_0 remain within the same bin for the entire search. While some targets have a non-zero measurement of $\dot{P}\,T_{\rm obs}$ ($\dot{a}_0\,T_{\rm obs}$), in all cases it is much smaller than the template spacing in P (a_0) [62, 69, 108].

It is unlikely that the true source parameters lie exactly on a grid point in the parameter space. Thus the grid is spaced such that the maximum mismatch, $\mu_{\rm max}$, is never more than an acceptable level. The mismatch is defined as the fractional loss in signal-to-noise ratio between the search executed at the true parameters and at the nearest grid point [109]. We calculate the number of grid points required for P, a_0 and $T_{\rm asc}$ using Eq. (71) of Ref. [109], i.e.

$$N_P = \pi^2\sqrt{6}\,\mu_{\rm max}^{-1/2} f a_0 \frac{\gamma T_{\rm drift}}{P^2}\sigma_P\,, \tag{5}$$

$$N_{a_0} = 3\pi\sqrt{2}\,\mu_{\rm max}^{-1/2} f \sigma_{a_0}\,, \tag{6}$$

$$N_{T_{\rm asc}} = 6\pi^2\sqrt{2}\,\mu_{\rm max}^{-1/2} f a_0 \frac{1}{P}\sigma_{T_{\rm asc}}\,, \tag{7}$$

where γ is a refinement factor defined in general in Eq. (67) of Ref. [109]. In the case of O3, the semi-coherent segments are contiguous so we have $\gamma = N_T = 36$. We fix $\mu_{\rm max} = 0.1$. A set of software injections into O3 data verifies that a template grid constructed with $\mu_{\rm max} = 0.1$ results in a maximum fractional loss in signal-to-noise ratio of 10%. We make the conservative choice of rounding N_P, N_{a_0}, and $N_{T_{\rm asc}}$ up to the nearest integer, after setting f to the highest frequency in each 0.61 Hz sub-band. As in Ref. [12] we find $N_{a_0} = 1$ for each target and sub-band, and so hold a_0 constant at its central value while searching over P and $T_{\rm asc}$. Table II shows N_P, $N_{T_{\rm asc}}$, and $N_{\rm tot} = N_P N_{T_{\rm asc}}$ for each target and sub-band. When Eq. (5) or (7) predicts only two templates for a given sub-band we round up to three, ensuring that the central value of P or $T_{\rm asc}$ from EM observations is included in the template bank. Note that the EM observations are sufficiently precise that $< 5 \times 10^4$ templates are required across all targets and sub-bands. This is in contrast to the O2 search for continuous gravitational waves from Scorpius X-1, for which $\sim 10^9$ templates were needed, mainly due to the large uncertainty in a_0, and the unknown rotation frequency [11].

C. Thresholds

The output of the search algorithm outlined in Sec. II is a $\mathcal{L}$ value corresponding to the most likely path through each sub-band for each orbital template $(P, a_0, T_{\rm asc})$. We flag a template for further follow-up if $\mathcal{L}$ exceeds a threshold, $\mathcal{L}_{\rm th}$, given an acceptable probability of false alarm.

TABLE II: Starting frequencies, f_s, for each ~ 0.61 Hz-wide sub-band, number of templates needed to cover the P and T_{asc} domains in that sub-band, N_P and $N_{T_{asc}}$ respectively, and the total number of templates for each sub-band, $N_{tot} = N_P N_{T_{asc}}$. The projected semi-major axis a_0 is known precisely enough that we have $N_{a_0} = 1$ for each sub-band.

Target	f_s (Hz)	N_P	$N_{T_{asc}}$	N_{tot}	Target	f_s (Hz)	N_P	$N_{T_{asc}}$	N_{tot}
IGR J00291+5934	598.6	1	3	3	IGR J17498−2921	400.7	1	17	17
	798.5	1	3	3		534.7	1	22	22
	1197.8	1	3	3		802.0	3	33	99
MAXI J0911−655	339.7	1	10	10	IGR J17511−3057	244.5	1	14	14
	453.3	3	14	42		326.4	1	19	19
	679.9	3	20	60		489.7	1	28	28
XTE J0929−314	184.8	3	52	156	XTE J1751−305	435.0	4	195	780
	246.8	3	69	207		580.4	5	260	1300
	370.2	3	104	312		870.6	8	390	3120
IGR J16597−3704	104.9	49	23	1127	Swift J1756.9−2508	181.8	10	34	340
	140.2	65	31	2015		242.8	13	45	585
	210.4	97	46	4462		364.1	20	67	1340
IGR J17062−6143	163.4	1	1	1	IGR J17591−2342	527.1	1	3	3
	218.2	1	1	1		703.2	3	3	9
	327.3	1	1	1		1054.9	3	4	12
IGR J17379−3747	467.8	4	12	48	XTE J1807−294	190.3	1	7	7
	624.1	5	15	75		254.2	1	9	9
	936.2	7	23	161		381.2	1	13	13
SAX J1748.9−2021	442.1	3	18	54	SAX J1808.4−3658	400.7	4	5	20
	589.8	3	24	72		534.6	5	7	35
	884.7	3	36	108		802.0	7	10	70
NGC 6440 X−2	205.6	1	6	6	XTE J1814−338	314.1	1	9	9
	274.5	1	8	8		419.1	1	12	12
	411.8	1	12	12		628.7	1	17	17
IGR J17494−3030	375.7	21	112	2352	IGR J18245−2452	254.0	3	44	132
	501.4	27	150	4050		339.1	3	58	174
	752.1	41	224	9184		508.7	5	87	435
Swift J1749.4−2807	517.6	7	43	301	HETE J1900.1−2455	377.0	1	17	17
	690.6	9	57	513		503.1	1	22	22
	1035.8	13	85	1105		754.6	1	33	33

To determine $\mathcal{L}_{th}$ we need to know how often pure noise yields $\mathcal{L} > \mathcal{L}_{th}$. The distribution of $\mathcal{L}$ in noise-only data is unknown analytically, but depends on P, a_0, and the frequency, so Monte-Carlo simulations are used to determine $\mathcal{L}_{th}$ in each sub-band for each target.

We estimate the distribution of $\mathcal{L}$ in noise via two methods: i) using realizations of synthetic Gaussian noise generated using the `lalapps_Makefakedata_v5` program in the LIGO Scientific Collaboration Algorithm Library (LALSuite) [50], and ii) searching O3 data in off-target locations to simulate different realizations of true detector noise. As in Refs. [11, 12] we generate realizations for each target and sub-band, and apply the search algorithm described in Sec. II to each realization to recover samples from the noise-only distribution of $\mathcal{L}$. Details on how we use these samples to find $\mathcal{L}_{th}$ for each sub-band are given in Appendix A. Unless otherwise noted, $\mathcal{L}_{th}$ refers to the lower of the two thresholds derived from the methods listed above to minimize false dismissals.

To define $\mathcal{L}_{th}$ we must also account for a "trials factor" due to the number of templates searched in each sub-band. We assume that in noise-only data the spacing between templates is sufficiently large such that each template returns a statistically independent $\mathcal{L}$. We can therefore relate the false alarm probability for a search of a sub-band with N_{tot} templates, $\alpha_{N_{tot}}$, to the probability of a false alarm for a single template, α, viz.

$$\alpha_{N_{tot}} = 1 - (1 - \alpha)^{N_{tot}} . \tag{8}$$

Previous comparable searches have set $\alpha_{N_{tot}}$ between 0.01 and 0.3 [11, 12, 38, 39]. In this search, we fix $\alpha_{N_{tot}} = 0.3$, i.e. set the acceptable probability of false alarm at 30% per sub-band. As we search a total of $20 \times 3 = 60$ sub-bands, we expect ~ 18 candidates above $\mathcal{L}_{th}$ due to noise alone (i.e. false alarms), a reasonable number on which to perform more exhaustive follow-up. Looking ahead to the results in Sec. VII we recover 4611 candidates above $\mathcal{L}_{th}$. While this number is much higher than the ~ 18 false alarms expected, almost all of these candidates are non-Gaussian noise artifacts in one (or both) of the detectors. All but 16 of the 4611 candidates are eliminated by the vetoes outlined in Sec. VI. We reiterate that $\mathcal{L}_{th}$ in each sub-band is the lower of the two

thresholds described in Appendix A, lowering conservatively the probability of false dismissal.

D. Computing resources

A mix of central processing unit (CPU) and graphical processing unit (GPU) resources are used. The GPU implementation of the $\mathcal{J}$-statistic is identical to that used in Refs. [11, 12]. The entire search across all targets and sub-bands takes ~ 30 CPU-hours and ~ 40 GPU-hours when using compute nodes equipped with Xeon Gold 6140 CPUs and NVIDIA P100 12GB PCIe GPUs. Producing $\mathcal{L}_{\rm th}$ for each sub-band, as described in Sec. IV C, takes an additional $\sim 5\times10^2$ CPU-hours and $\sim 4\times10^3$ GPU-hours to perform the search on different noise realizations. The additional follow-up in Appendix B 1 requires an additional $\sim 10^3$ CPU-hours and $\sim 10^2$ GPU-hours.

V. O3 DATA

We use the full dataset from O3, spanning from April 1, 2019, 15:00 UTC to March 27, 2020, 17:00 UTC, from the LIGO Livingston and Hanford observatories. We do not use any data from the Virgo interferometer in this analysis, due to its lower sensitivity compared to the two LIGO observatories in the frequency sub-bands over which we search [110]. The data products ingested by the search algorithm described in Sec. II are short Fourier transforms (SFTs) lasting 1800 s. Times when the detectors were offline, poorly calibrated, or were impacted by egregious noise, are excluded from analysis by using "Category 1" vetoes as defined in section 5.2 of Ref. [110]. The SFTs are generated from the "C01 calibrated self-gated" dataset, which is the calibrated strain data with loud transient glitches removed [111]. Transient glitches otherwise impact the noise floor, as described in section 6.1 of Ref. [110]. The median systematic error of the strain magnitude across O3 is $< 2\%$ [112, 113].

The coherence time $T_{\rm drift} = 10\,$d splits the data into $N_T = 36$ segments. However, due to the month-long commissioning break between O3a and O3b there are two segments without any SFTs. These two segments, starting at October 8, 2019, 15:00 UTC and October 15, 2019, 15:00 UTC, are replaced with a uniform log-likelihood for all frequency bins, which allows the HMM to effectively skip over them while still allowing spin wandering. When generating synthetic data in Secs. IV C and IX the same two data segments are also replaced with uniform log-likelihoods to emulate the real search.

VI. VETOES

When a candidate is returned with $\mathcal{L} > \mathcal{L}_{\rm th}$ we must decide whether there are reasonable grounds to veto the candidate as non-astrophysical. We use three of the vetoes from Ref. [12]: the known line veto, detailed in Sec. VI A, the single interferometer veto, detailed in Sec. VI B, and the off-target veto, detailed in Sec. VI C. The false dismissal rate of these vetoes is less than 5% (see detailed safety investigations in section IVB of Ref. [38] and section IVB of Ref. [11]).

A. Known line veto

As part of the detector characterization process many harmonic features are identified as instrumental "known lines" [110, 114]. However, the exact source of these harmonic features is sometimes unidentified, and their impact cannot always be mitigated through isolating hardware components or post-processing the data [110, 114]. We use the vetted known lines list in Ref. [115].

Any candidate close to a known line at frequency $f_{\rm line}$ is vetoed. Precisely, if for any time $0 \le t \le T_{\rm obs}$ the candidate's frequency path $f(t)$ satisfies

$$|f(t) - f_{\rm line}| < 2\pi a_0 f_{\rm line}/P\,, \tag{9}$$

then the candidate is vetoed[6].

B. Single interferometer veto

An instrumental artifact is unlikely to be coincident in both detectors, so the candidate's $\mathcal{L}$ should be dominated by only one of the detectors if the signal is non-astrophysical. On the other hand, an astrophysical signal may need data from both detectors to be detected, or if it is particularly strong may be seen in both detectors individually.

We label the original log-likelihood as $\mathcal{L}_\cup$, and we also calculate the two single interferometer log-likelihoods $\mathcal{L}_a$ and $\mathcal{L}_b$ (where the higher $\mathcal{L}$ is labelled with b for definiteness). There are four possible outcomes for this veto:

1. If the $\mathcal{L}$ value in one detector is sub-threshold, while the other is above the two-detector $\mathcal{L}$ value, i.e. one has $\mathcal{L}_a < \mathcal{L}_{\rm th}$ and $\mathcal{L}_b > \mathcal{L}_\cup$ and $f_b(t)$, the frequency path associated with $\mathcal{L}_b$, is close to the frequency path of the candidate when using data from both detectors, $f_\cup(t)$, i.e.

$$|f_\cup(t) - f_b(t)| < 2\pi a_0 f_\cup/P\,, \tag{10}$$

[6] One might consider an additional Doppler broadening factor of $2\pi a_\oplus/1\,$yr, where $a_\oplus$ is the mean Earth-Sun distance, as stationary lines in the detector frame get Doppler shifted when transforming the data to the frame of reference of the source. We opt not to apply this factor for simplicity in this search, as the exact pattern of Doppler modulation depends strongly on the sky location of the target. Looking ahead to the results in Sec. VII, we note that none of the 16 surviving candidates is within $2\pi f a_\oplus/1\,$yr of any known line.

then the candidate is likely to be a noise artifact in detector b, and is vetoed.

2. If one has $\mathcal{L}_a < \mathcal{L}_{\rm th}$ and $\mathcal{L}_b > \mathcal{L}_\cup$, but Eq. (10) does not hold then the candidate signal cannot be vetoed, as the single-interferometer searches did not find the same candidate. This could indicate that the candidate is a weak astrophysical signal that needs data from both detectors to be detectable.

3. If one has $\mathcal{L}_a > \mathcal{L}_{\rm th}$ and $\mathcal{L}_b > \mathcal{L}_{\rm th}$, the candidate could represent a strong astrophysical signal that is visible in data from both detectors independently, or it could represent a common noise source. Candidates in this category cannot be vetoed.

4. If one has $\mathcal{L}_a < \mathcal{L}_{\rm th}$ and $\mathcal{L}_b < \mathcal{L}_\cup$, data from both detectors is needed for the candidate to be above threshold, possible indicating a weak astrophysical signal. Candidates in this category cannot be vetoed.

C. Off-target veto

The third veto we apply to a candidate is to search an off-target sky position with the same orbital template. If the off-target search returns $\mathcal{L} > \mathcal{L}_{\rm th}$ then the candidate is likely instrumental rather than astrophysical. For this veto, off-target corresponds to shifting the target sky position +40 m in RA and +10° in Dec.

VII. O3 SEARCH RESULTS

The results of the search of all 20 targets are summarized in Fig. 1, with $\alpha_{N_{\rm tot}} = 0.3$, i.e. a nominal probability of false alarm per sub-band of 30%. Each symbol indicates, for all templates with $\mathcal{L} > \mathcal{L}_{\rm th}$, the terminating frequency bin and $p_{\rm noise}$, the probability that a search of that candidate's sub-band in pure noise would return at least one candidate at least as loud as the one seen. Equation (A6) in Appendix A 5 defines $p_{\rm noise}$ explicitly. Each candidate is colored according to $\mathcal{L}$. We note that high $\mathcal{L}$ does not always correspond to low $p_{\rm noise}$ due to the differing "trials factors" in each sub-band, as accounted for when calculating $\mathcal{L}_{\rm th}$ via Eq. (8). A low value of $p_{\rm noise}$ corresponds to a higher probability that the candidate is a true astrophysical signal. Targets not listed in the legend return zero candidates above threshold. We do not display in Fig. 1 candidates that are eliminated by any of the vetoes described in Sec. VI for clarity.

In total, across all targets and sub-bands, there are 4611 candidates with $\mathcal{L} > \mathcal{L}_{\rm th}$, before the vetoes are applied. All but 100 are eliminated by veto A (known line veto). A further 84 candidates are eliminated by veto B (single interferometer veto). None of the remaining candidates are eliminated by veto C (off-target veto), leaving 16 candidates passing all of the vetoes outlined in Sec. VI. None of the surviving candidates from the O3 search coincide in their orbital template and terminating frequency bin with the seven above- or sub-threshold candidates from the O2 search (c.f. Table VI of Ref. [12]). If we set $\alpha_{N_{\rm tot}} = 0.01$, i.e. set the probability of false alarm per sub-band to 1%, the search does not return any candidates with $\mathcal{L} > \mathcal{L}_{\rm th}$ for any target or sub-band, after vetoes are applied.

In Secs. VII A–VII T we summarize the search results for each of the 20 targets. To guide the reader, and not clutter the main body of the paper, the full search results for one target, IGR J18245−2452, are shown in Fig. 2, while the full search results for the other 19 targets are shown in Figs. 4a–4s in Appendix B. The orbital template, terminating frequency bin, $\mathcal{L}$, and $p_{\rm noise}$ for all 16 candidates with $\mathcal{L} > \mathcal{L}_{\rm th}$ are collated in Table VI in Appendix B. We present further follow-up of the 16 candidates in Appendix B 1. We find no convincing evidence that any are a true astrophysical signal.

A. IGR J18245−2452

The search results for IGR J18245−2452 are presented in Fig. 2. Each marker in Fig. 2 shows the terminating frequency and associated $\mathcal{L}$ of the most likely path through the sub-band for a given template, i.e. choice of P and $T_{\rm asc}$. The vertical blue dashed (green dot-dashed) lines correspond to the threshold set via Gaussian (off-target) noise realizations, $\mathcal{L}_{\rm th,\,G}$ ($\mathcal{L}_{\rm th,\,OT}$), in each sub-band, with $\alpha_{N_{\rm tot}} = 0.3$. See Appendix A for details on how we set thresholds in each sub-band. The horizontal red lines indicate known instrumental lines in the detector with bandwidth indicated by the shading. There are zero above-threshold candidates in the $f_\star$ and $4f_\star/3$ sub-bands. There are 435 above-threshold candidates in the $2f_\star$ sub-band, which are all coincident with known noise lines in both the Livingston and Hanford detectors, and are therefore eliminated by veto A. The sub-band around 508 Hz is especially noisy due to violin mode resonances [110].

B. IGR J00291+5934

The search results for IGR J00291+5934 are shown in Fig. 4a, which is laid out identically to Fig. 2. There are zero above-threshold candidates in the $4f_\star/3$ and $2f_\star$ sub-bands. There are three above-threshold candidates in the $f_\star$ sub-band, however all three of these candidates are coincident with known noise lines in the Hanford detector, and are therefore eliminated with veto A.

C. MAXI J0911−655

The search results for MAXI J0911−655 are shown in Fig. 4b, which is laid out identically to Fig. 2. There

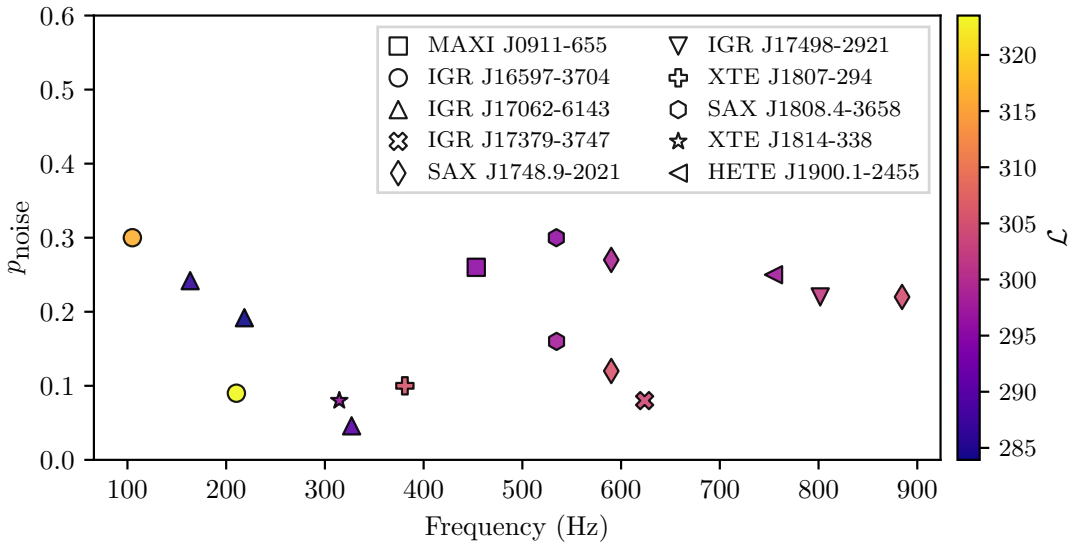

FIG. 1: Summary of search results across all targets and sub-bands with $\mathcal{L} > \mathcal{L}_{\rm th}$. The different symbols correspond to candidates from different targets. The ordinate shows $p_{\rm noise}$ for each candidate, the probability that a search of that candidate's sub-band in pure noise would return at least one candidate at least as loud as the one seen. The color of each candidate indicates $\mathcal{L}$ (see color bar at right). Candidates that are eliminated by the vetoes outlined in Sec. VI are not shown for clarity. Details on the search results are in Sec. VII and Appendix B.

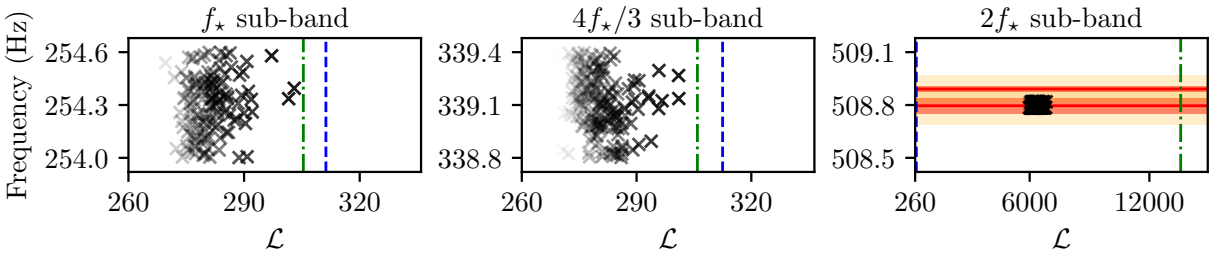

FIG. 2: Search results for IGR J18245−2452. Black crosses indicate the terminating frequency and $\mathcal{L}$ for the most likely path through the sub-band for each binary template. The vertical blue dashed (green dot-dashed) lines correspond to the threshold set via Gaussian (off-target) noise realizations, $\mathcal{L}_{\rm th,\,G}$ ($\mathcal{L}_{\rm th,\,OT}$), in each sub-band. Solid red lines in the right panel indicate the peak frequency of known instrumental lines in the Hanford detector; the orange band indicates the width of the line in the detector frame and the yellow band indicates the increased effective width due to Doppler broadening, as described in Sec. VI A. Multiple overlapping orange bands creates the red bands. The sub-band around 508.8 Hz is especially noisy due to test mass suspension violin mode resonances [110]. The transparency of crosses in sub-bands with many templates, is adjusted relative to the maximum $\mathcal{L}$ in that sub-band for clarity.

are zero above-threshold candidates in the $f_\star$ and $2f_\star$ sub-bands. There is one above-threshold candidate in the $4f_\star/3$ sub-band which survives all of the vetoes and has $p_{\rm noise} = 0.26$. Additional follow-up, presented in Appendix B 1, does not provide any evidence that this candidate is a true astrophysical signal.

D. XTE J0929−314

The search results for XTE J0929−314 are shown in Fig. 4c, which is laid out identically to Fig. 2. There are zero above-threshold candidates across all three sub-bands.

E. IGR J16597−3704

The search results for IGR J16597−3704 are shown in Fig. 4d, which is laid out identically to Fig. 2. Each sub-band for this target is contaminated with known noise lines. There are 84 above-threshold candidates in the $4f_\star/3$ sub-band, however they are all eliminated by veto B. One above-threshold candidate is returned in

each of the $f_\star$ and $2f_\star$ sub-bands. Both of these candidates survive all of the vetoes, and have $p_{\rm noise} = 0.30$ and $p_{\rm noise} = 0.09$ respectively. Further follow-up, including the frequency path and cumulative log-likelihood for the latter candidate, is presented in Appendix B 1. This follow-up does not provide any evidence that either candidate is a true astrophysical signal.

F. IGR J17062−6143

The search results for IGR J17062−6143 are shown in Fig. 4e, which is laid out identically to Fig. 2. Given the long-term timing presented in Ref. [69] there is only one template needed in each of the three sub-bands for this target. The template returns $\mathcal{L} > \mathcal{L}_{\rm th}$ in all three of the $f_\star$, $4f_\star/3$, and $2f_\star$ sub-bands. All of these candidates survive all of the vetoes, and have $p_{\rm noise} = 0.24$, $p_{\rm noise} = 0.19$, and $p_{\rm noise} = 0.05$ respectively. Further follow-up, including the frequency path and cumulative log-likelihood for the candidate with $p_{\rm noise} = 0.05$, is presented in Appendix B 1. This follow-up does not provide any evidence that any of the three candidates are a true astrophysical signal.

G. IGR J17379−3747

The search results for IGR J17379−3747 are shown in Fig. 4f, which is laid out identically to Fig. 2. There are zero above-threshold candidates in the $f_\star$ and $2f_\star$ sub-bands. There is one above-threshold candidate in the $4f_\star/3$ sub-band which survives all of the vetoes and has $p_{\rm noise} = 0.08$. Further follow-up, including the frequency path and cumulative log-likelihood, for this candidate is presented in Appendix B 1. This follow-up does not provide any evidence that the candidate is a true astrophysical signal.

H. SAX J1748.9−2021

The search results for SAX J1748.9−2021 are shown in Fig. 4g, which is laid out identically to Fig. 2. There are zero above-threshold candidates in the $f_\star$ sub-band. There are two above-threshold candidates in the $4f_\star/3$ sub-band which survive all of the vetoes and have $p_{\rm noise} = 0.12$ and $p_{\rm noise} = 0.27$. There is one above-threshold candidate in the $2f_\star$ sub-band which survives all of the vetoes and has $p_{\rm noise} = 0.22$. Additional follow-up, presented in Appendix B 1, does not provide any evidence that any of the three candidates are a true astrophysical signal.

I. NGC 6440 X−2

The search results for NGC 6440 X−2 are shown in Fig. 4h, which is laid out identically to Fig. 2. There are zero above-threshold candidates across all three sub-bands.

J. IGR J17494−3030

The search results for IGR J17494−3030 are shown in Fig. 4i, which is laid out identically to Fig. 2. There are zero above-threshold candidates in the $f_\star$ and $2f_\star$ sub-bands. All 4050 candidates in the $4f_\star/3$ sub-band are above threshold, however all of them are coincident with a known noise line in the Hanford detector, and are therefore eliminated with veto A. The sub-band around 501.7 Hz is especially noisy due to violin mode resonances [110].

K. Swift J1749.4−2807

The search results for Swift J1749.4−2807 are shown in Fig. 4j, which is laid out identically to Fig. 2. There are zero above-threshold candidates in the $f_\star$ and $4f_\star/3$ sub-bands. There is one above threshold candidate in the $2f_\star$ sub-band. However it is coincident with a known noise line in the Hanford detector, and is therefore eliminated by veto A.

L. IGR J17498−2921

The search results for IGR J17498−2921 are shown in Fig. 4k, which is laid out identically to Fig. 2. There are zero above-threshold candidates in the $f_\star$, and $4f_\star/3$ sub-bands. There is one above-threshold candidate in the $2f_\star$ sub-band which survives all of the vetoes and has $p_{\rm noise} = 0.22$. Additional follow-up, presented in Appendix B 1, does not provide any evidence that this candidate is a true astrophysical signal.

M. IGR J17511−3057

The search results for IGR J17511−3057 are shown in Fig. 4l, which is laid out identically to Fig. 2. There are zero above-threshold candidates across all three sub-bands.

N. XTE J1751−305

The search results for XTE J1751−305 are shown in Fig. 4m, which is laid out identically to Fig. 2. There are zero above-threshold candidates across all three sub-bands.

O. Swift J1756.9−2508

The search results for Swift J1756.9−2508 are shown in Fig. 4n, which is laid out identically to Fig. 2. There are zero above-threshold candidates across all three sub-bands.

P. IGR J17591−2342

The search results for IGR J17591−2342 are shown in Fig. 4o, which is laid out identically to Fig. 2. There are zero above-threshold candidates across all three sub-bands.

Q. XTE J1807−294

The search results for XTE J1807−294 are shown in Fig. 4p, which is laid out identically to Fig. 2. There are zero above-threshold candidates in the $f_\star$ and $4f_\star/3$ sub-bands. There is one above-threshold candidate in the $2f_\star$ sub-band which survives all of the vetoes and has $p_{\rm noise} = 0.10$. Further follow-up, including the frequency path and cumulative log-likelihood, for this candidate is presented in Appendix B 1. This follow-up does not provide any evidence that the candidate is a true astrophysical signal.

R. SAX J1808.4−3658

The search results for SAX J1808.4−3658 are shown in Fig. 4q, which is laid out identically to Fig. 2. There are zero above-threshold candidates in the $f_\star$ and $2f_\star$ sub-bands. There are two above-threshold candidates in the $4f_\star/3$ sub-band which survive all of the vetoes and have $p_{\rm noise} = 0.16$ and $p_{\rm noise} = 0.30$. Additional follow-up, presented in Appendix B 1, does not provide any evidence that either candidate is a true astrophysical signal.

SAX J1808.4−3658 was observed in outburst in August 2019, during O3a [58, 59]. This allows us to perform an additional target-of-opportunity search during only its active phase. If the target only emits continuous gravitational waves during outburst, searching a shorter duration of data increases the probability of detection by increasing the signal-to-noise ratio. The details and results of this target-of-opportunity search are in Sec. VIII. In summary, after searching with three separate coherence times of $T_{\rm drift} = 1\,$d, $T_{\rm drift} = 8\,$d, and $T_{\rm drift} = 24\,$d, only one candidate is above threshold and survives all of the vetoes. The candidate is found using $T_{\rm drift} = 24\,$d in the $f_\star$ sub-band, and has $p_{\rm noise} = 0.02$. Additional follow-up does not reveal any informative features that would distinguish between an astrophysical signal and noise. It does not coincide with either of the two candidates in the $4f_\star/3$ sub-band found in the semi-coherent search using the full O3 data set.

S. XTE J1814−338

The search results for XTE J1814−338 are shown in Fig. 4r, which is laid out identically to Fig. 2. There are zero above-threshold candidates in the $4f_\star/3$ and $2f_\star$ sub-bands. There is one above-threshold candidate in the $f_\star$ sub-band which survives all of the vetoes and has $p_{\rm noise} = 0.08$. Further follow-up, including the frequency path and cumulative log-likelihood, for this candidate is presented in Appendix B 1. This follow-up does not provide any evidence that the candidate is a true astrophysical signal.

T. HETE J1900.1−2455

The search results for HETE J1900.1−2455 are shown in Fig. 4s, which is laid out identically to Fig. 2. There are zero above-threshold candidates in the $f_\star$ sub-band. All 22 templates in the $4f_\star/3$ sub-band return candidates above $\mathcal{L}_{\rm th}$, however these candidates are all coincident with known noise lines in the Hanford detector, and are summarily eliminated with veto A. The sub-band around 503 Hz is especially noisy due to violin mode resonances [110]. There is one above-threshold candidate in the $2f_\star$ sub-band which survives all of the vetoes and has $p_{\rm noise} = 0.25$. Additional follow-up, presented in Appendix B 1, does not provide any evidence that this candidate is a true astrophysical signal.

VIII. TARGET-OF-OPPORTUNITY SEARCH: SAX J1808.4−3658 IN OUTBURST

On August 7 2019 SAX J1808.4−3658 went into outburst [57]. The Neutron star Interior Composition Explorer (NICER) team undertook a high-cadence monitoring campaign, and performed a timing analysis of the pulsations [58]. The outburst lasted for roughly 24 days, with enhanced X-ray flux observed between August 7 2019 and August 31 2019 (see Fig. 1 of Ref. [58]). We note that the *Swift* X-ray Telescope observed increased X-ray activity from August 6 2019, and observations in the optical i'-band with the Las Cumbres Observatory network detected an increased flux from July 25 2019 [59].

Outburst events are attributed to in-falling plasma that is channeled by the magnetosphere onto a localized region on the neutron star surface, creating a hot spot that rotates with the star [116]. As the observed X-ray flux is assumed to be linearly proportional to the mass accretion rate, an outburst could result in a larger mountain on the neutron star surface (or excite r-modes in the interior), compared to when the AMXP is in quiescence [60, 117].

If continuous gravitational waves are only emitted from SAX J1808.4−3658 when it is in outburst, searching all of the O3 data decreases the signal-to-noise ra-

tio, as compared to only searching data from the outburst. To protect against this possibility, we do an additional search for continuous gravitational waves from SAX J1808.4−3658 using data from both LIGO observatories between 1249171218 GPS time (August 7 2019) and 1251244818 GPS time (August 31 2019), rather than data from the entirety of O3, as in Sec. VII R.

A. Search parameters

The search algorithm is laid out in Sec. II. We run the search using three different coherence times, setting $T_{\rm drift} = 1\,{\rm d}$, $T_{\rm drift} = 8\,{\rm d}$, and $T_{\rm drift} = 24\,{\rm d}$. We search three sub-bands centered on $\{1, 4/3, 2\}f_\star$, for each $T_{\rm drift}$. The width of the sub-band depends on $T_{\rm drift}$. It is $\sim 0.76\,{\rm Hz}$ for the searches with $T_{\rm drift} = 1\,{\rm d}$ and $8\,{\rm d}$, and is $\sim 1.01\,{\rm Hz}$ for the search with $T_{\rm drift} = 24\,{\rm d}$. Given the precise timing achieved during the outburst in 2019 [58], and the shorter search duration, only one $\{P,\ T_{\rm asc},\ a_0\}$ template is required for each sub-band, according to Eqs. (5)–(7). Due to the different values of $T_{\rm drift}$, shorter total duration, and different number of templates, we re-calculate $\mathcal{L}_{\rm th}$ for each sub-band and value of $T_{\rm drift}$, using the procedure outlined in Sec. IV C and Appendix A. As in the full O3 search, we set the probability of false alarm in each sub-band at $\alpha_{N_{\rm tot}} = 0.3$. For all candidates that have $\mathcal{L} > \mathcal{L}_{\rm th}$ we apply the three vetoes described in VI.

B. Search results

For $T_{\rm drift} = 1\,{\rm d}$, the search in the $f_\star$ sub-band returns one candidate above $\mathcal{L}_{\rm th}$. The candidate survives both veto A (known line) and veto B (single interferometer), but fails veto C (off-target). The searches in the $4/3f_\star$ and $2f_\star$ sub-bands do not return any candidates above $\mathcal{L}_{\rm th}$.

For $T_{\rm drift} = 8\,{\rm d}$, there are no candidates above $\mathcal{L}_{\rm th}$ in any of the three sub-bands.

For $T_{\rm drift} = 24\,{\rm d}$, the searches in the $4f_\star/3$ and $2f_\star$ sub-bands do not return any candidates above $\mathcal{L}_{\rm th}$. The search in the $f_\star$ sub-band does return one candidate above $\mathcal{L}_{\rm th}$. This candidate survives all of the vetoes outlined in Sec. VI. We remind the reader that with $\alpha_{N_{\rm tot}} = 0.3$ and nine sub-bands searched (three for each of the three choices of $T_{\rm drift}$), we should expect ~ 3 candidates above threshold purely due to noise. The probability that we would see a value of $\mathcal{L}$ at least this large if this sub-band is pure noise, $p_{\rm noise}$, is 0.02. The template and frequency of the candidate are not coincident with any candidate from the full O3 search (see Table VI) or the sub-threshold candidate found in the search of this sub-band in O2 data [12]. By setting $T_{\rm drift} = T_{\rm obs} = 24\,{\rm d}$ we perform a fully coherent search across this time period, with a frequency bin size of $\Delta f = 2.4\times10^{-7}\,{\rm Hz}$. We describe in Appendix C further follow-up of this candidate. In summary, we find no significant evidence that it is an astrophysical signal rather than a noise fluctuation.

IX. FREQUENTIST UPPER LIMITS

If we assume that the remaining candidates reported in Sec. VII and Appendix B are false alarms, we can place an upper limit on the wave strain that is detectable at a confidence level of 95%, $h_0^{95\%}$, in a sub-band. The value of $h_0^{95\%}$ is a function of our algorithm, the detector configuration during O3, and our assumptions about the signal model. We describe the method used to estimate $h_0^{95\%}$ in Sec. IX A, present the upper limits in each sub-band in Sec. IX B, and compare the results to indirect methods that calculate the expected strain in the $2f_\star$ sub-band in Sec. IX C. The astrophysical implications are discussed in Sec. IX D.

A. Upper limit procedure in a sub-band

We set empirical frequentist upper limits in each sub-band using a sequence of injections into O3 SFTs. For each sub-band we inject $N_{\rm trials} = 100$ simulated binary signals at 12–15 fixed values of h_0 using `lalapps_Makefakedata_v5` [50]. For each of the $N_{\rm trials}$ injections at a fixed h_0 we select a constant injection frequency, $f_{\rm inj}$, uniformly from the sub-band. While the injected signal has zero spin-wandering, we still use $T_{\rm drift} = 10\,{\rm d}$ in the search algorithm outlined in Sec. II to mimic the real search. The injected period, $P_{\rm inj}$, and time of ascension, $T_{\rm asc,\,inj}$ are chosen uniformly from the ranges $[P-3\sigma_P, P+3\sigma_P]$ and $[T_{\rm asc}-3\sigma_{T_{\rm asc}}, T_{\rm asc}+3\sigma_{T_{\rm asc}}]$ respectively. We keep a_0 fixed at the precisely known value for each target. The polarization, ψ, is chosen uniformly from the range $[0, 2\pi]$. The cosine of the projected inclination angle of the neutron star spin axis with our line of sight, $\cos\iota$, is chosen uniformly from the range $[-1, 1]$[7]. We then search for the injected signal with the template in this sub-band's template grid that is nearest to $\{P_{\rm inj}, T_{\rm asc,\,inj}\}$. We re-calculate $\mathcal{L}_{\rm th}$ such that the probability of false alarm in each sub-band is $\alpha_{N_{\rm tot}} = 0.01$. This allows us to set conservative upper limits, even in sub-bands where we have marginal candidates above a threshold corresponding to a probability of false alarm of 30% per sub-band. By recording the fraction of injected signals we recover at each h_0 with $\mathcal{L} > \mathcal{L}_{\rm th}$ we estimate the efficiency, ε, as a function of h_0. We then perform a logistic regression [118] to obtain a sigmoid fit to $\varepsilon(h_0)$,

[7] While the inclination angle of the binary with respect to our line of sight is restricted via EM observations for some of our targets, we opt to marginalize over $\cos\iota$ as the neutron star spin axis may not necessarily align with the orbital axis of the binary. It is possible to scale our results via equation (19) of Ref. [106], if one wishes to fix $\cos\iota$.

and solve

$$\varepsilon(h_0^{95\%}) = 0.95 \ , \tag{11}$$

to find an estimate of $h_0^{95\%}$ in the given sub-band.

One might reasonably ask, how precise is this estimate of $h_0^{95\%}$? The main factors impacting the precision are: (i) the precision of the most likely parameters of the sigmoid, as estimated via logistic regression, when solving Eq. (11) for $h_0^{95\%}$, given the $N_{\rm trials}$ injections done at 12–15 values of h_0; and (ii) the assumption that the strain data (and hence the SFTs) are perfectly calibrated. We investigate the impact of (i) by drawing alternative sigmoid fits of $\varepsilon(h_0)$ using the covariance matrix of the parameters returned by the logistic regression. We find that inverting these alternative fits through Eq. (11) results in a value of $h_0^{95\%}$ that varies by less than 5% from the value calculated via the most likely parameters (at the 95% confidence level). The impact of (ii) is trickier to quantify. As described in Refs. [112, 113] the median systematic error in the magnitude of the strain is less than 2% in the 20–2000 Hz frequency band across O3a. The statistical uncertainty around the measurement of calibration bias means that in the worst case the true magnitude of the calibration bias may be as large as 7%. However, the calibration bias at a given frequency is not correlated between the detectors (see Figures 16 and 17 in Ref. [112]), and so the impact on a continuous gravitational wave search that combines data from both detectors is likely to be less than 7%.

In light of the above considerations we quote $h_0^{95\%}$ to a precision of two significant figures, but we emphasize that estimating $h_0^{95\%}$ involves many (potentially compounding) uncertainties. Subsequent conclusions about the physical system that are drawn from estimates of $h_0^{95\%}$ cannot be more precise than the estimate of $h_0^{95\%}$ itself.

B. Upper limits

The estimates of $h_0^{95\%}$ for each target and sub-band are listed in Table III. Dashes correspond to sub-bands that are highly contaminated with noise lines, which preclude the procedure described in Sec. IX A, as one always finds $\mathcal{L} > \mathcal{L}_{\rm th}$, regardless of h_0. The most sensitive sub-bands are for IGR J17062−6143 with $h_0^{95\%} = 4.7\times10^{-26}$ in both the $4f_\star/3$ and $2f_\star$ sub-bands (centered around 218.2 Hz and 327.6 Hz respectively). These sub-bands lie in the most sensitive band of the detector, and the binary elements are known to high precision [69], so only one template is needed in each sub-band, corresponding to a relatively lower $\mathcal{L}_{\rm th}$ at fixed probability of false alarm.

No estimates of $h_0^{95\%}$ were established in Ref. [12] for the five targets therein. The search of XTE J1751−305 in S6 data estimated $h_0^{95\%} \approx 3.3\times10^{-24}$, 4.7×10^{-24}, and 7.8×10^{-24} in three sub-bands corresponding to $f_\star$, an r-mode frequency, and $2f_\star$ respectively [42]. Our estimates of $h_0^{95\%}$ for XTE J1751−305 improve these results by two orders of magnitude, because the detector is more sensitive, and $T_{\rm drift}$ is longer.

TABLE III: Upper limits on the detectable gravitational wave strain at a 95% confidence level, $h_0^{95\%}$, in each of the sub-bands for each target. See Sec. IX A for details on how they are estimated, and the precision to which they are known. Upper limits are not estimated in sub-bands marked with a "−" as these sub-bands are highly contaminated with known noise lines.

	$h_0^{95\%}$ in each sub-band ($\times10^{-26}$)		
Target	$f_\star$	$4f_\star/3$	$2f_\star$
IGR J00291+5934	−	7.6	11
MAXI J0911−655	7.7	6.4	7.3
XTE J0929−314	5.1	5.3	6.4
IGR J16597−3704	7.5	−	5.6
IGR J17062−6143	8.1	4.7	4.7
IGR J17379−3747	8.5	7.4	10
SAX J1748.9−2021	9.2	7.7	10
NGC 6440 X−2	6.2	7.2	5.8
IGR J17494−3030	8.3	−	9.0
Swift J1749.4−2807	11	17	24
IGR J17498−2921	7.0	6.6	8.4
IGR J17511−3057	7.5	5.5	6.6
XTE J1751−305	10	8.3	9.7
Swift J1756.9−2508	8.1	8.8	6.3
IGR J17591−2342	9.5	11	14
XTE J1807−294	6.1	5.0	5.6
SAX J1808.4−3658	6.4	6.9	8.8
XTE J1814−338	9.4	6.0	6.9
IGR J18245−2452	9.0	6.3	−
HETE J1900.1−2455	5.6	−	8.4

C. Comparison to expected strain from AMXPs

It is valuable to consider how strong the signal from our targets could be, given EM observations. If we assume that all rotational energy losses, as observed in the frequency derivative $\dot{f}_\star$, are converted into gravitational radiation, the indirect spin-down limit on the maximum strain, $h_{0,\,\rm sd}$, is [46]

$$h_{0,\,\rm sd} = 4.0\times10^{-28}\left(\frac{8\,\rm kpc}{D}\right) \times\left(\frac{600\,\rm Hz}{f_{\rm GW}}\right)^{1/2}\left(\frac{-\dot{f}_{\rm GW}}{10^{-14}\,\rm Hz\,s^{-1}}\right)^{1/2} , \tag{12}$$

where D is the distance to the target, $f_{\rm GW}$ is the gravitational wave frequency, and $\dot{f}_{\rm GW}$ is its derivative. In Eq. (12) we assume $I_{zz}/I_0 \approx 1$, i.e. the zz component of the moment-of-inertia tensor (I_{zz}) is very close to the moment-of-inertia of an undeformed star (I_0). We assume $f_{\rm GW} \approx 2f_\star$ when computing Eq. (12) for each of our targets. We list the best estimates for the distance

TABLE IV: Maximum expected strain from each target, as inferred from EM observations. The second column contains the best estimate for the distance to the target. Targets with "-" listed as the frequency derivative (third column), $\dot{f}_\star$, do not have a measured value during outburst, and also do not have a long-term (quiescent) $\dot{f}_\star$ measured either. The labels (A) and (Q) indicate that $\dot{f}_\star$ is measured in outburst and quiescence respectively. The scaling equations used to estimate the maximum spin-down strain (fourth column), $h_{0,\mathrm{sd}}$, and the maximum strain assuming torque-balance (sixth column), $h_{0\,\mathrm{torque}}$, are Eqs. (12) and (13) respectively. The $h_{0,\mathrm{sd}}$ value is calculated using the central distance and $\dot{f}_\star$ estimates. The $h_{0\,\mathrm{torque}}$ value is calculated using the maximum bolometric X-ray flux measured during outburst (fifth column), $F_{X,\mathrm{max}}$, which is typically measured to a precision of $\sim 10\%$. The X-ray flux of each target in quiescence is not shown, as it is only measured for half of the targets, and is usually $\sim 1-2$ orders of magnitude lower than $F_{X,\mathrm{max}}$. The seventh column contains $h_0^{95\%}$ in the $2f_\star$ sub-band (fourth column of Table III) to facilitate comparisons between $h_0^{95\%}$ and $h_{0\,\mathrm{torque}}$ or $h_{0,\mathrm{sd}}$.

Target	Distance (kpc)	$\dot{f}_\star$ ($\mathrm{Hz\,s^{-1}}$)	$h_{0,\mathrm{sd}}$ ($\times 10^{-26}$)	$F_{X,\mathrm{max}}$ ($\times 10^{-8}$ $\mathrm{erg\,s^{-1}\,cm^{-2}}$)	$h_{0,\mathrm{torque}}$ ($\times 10^{-26}$)	$h_0^{95\%}$ ($\times 10^{-26}$)	Refs.
IGR J00291+5934	4.2(5)	$-4.0(1.4)\times10^{-15}$ (Q)	0.05	0.35	0.2	11	[53, 119–121]
MAXI J0911−655	9.45(15)	-	-	0.047	0.1	7.3	[63, 64, 122]
XTE J0929−314	7.4[a]	$-9.2(4)\times10^{-14}$ (A)	0.2	0.1	0.2	6.4	[53, 65, 123]
IGR J16597−3704	9.1[b]	-	-	0.065	0.2	5.6	[68]
IGR J17062−6143	7.3(5)	$+3.77(9)\times10^{-15}$ (A)	0.04[f]	0.006	0.05	4.7	[69, 124]
IGR J17379−3747	8[c]	$-1.2(1.9)\times10^{-14}$[e](A)	0.05	0.04	0.08	10	[70, 71, 125, 126]
SAX J1748.9−2021	8.5[b]	-	-	0.077	0.1	10	[53, 72, 127, 128]
NGC 6440 X−2	8.5[b]	-	-	0.02	0.09	5.8	[74, 127]
IGR J17494−3030	8[c]	$-2.1(7)\times10^{-14}$ (Q)	0.07	0.0143	0.05	9.0	[75]
Swift J1749.4−2807	6.7(1.3)	-	-	0.0352	0.07	24	[77, 78, 129]
IGR J17498−2921	7.6(1.1)	$-6.3(1.9)\times10^{-14}$ [e] (A)	0.1	0.2	0.2	8.4	[79, 80, 130]
IGR J17511−3057	3.6(5)	$+4.8(1.4)\times10^{-14}$ (A)	0.2[f]	0.2	0.2	6.6	[82]
XTE J1751−305	6.7[d]	$-5.5(1.2)\times10^{-15}$ (Q)	0.04	0.29	0.2	9.7	[53, 84, 131]
		$+3.7(1.0)\times10^{-13}$ (A)	0.2[f]				
Swift J1756.9−2508	8[c]	$-4.8(6)\times10^{-16}$ (Q)	0.02	0.288	0.3	6.3	[53, 85]
		$-4.3(2.1)\times10^{-11}$ [e] (A)	5				
IGR J17591−2342	7.6(7)	$-7.1(4)\times10^{-14}$ (A)	0.1	0.0535	0.09	14	[87, 132, 133]
XTE J1807−294	8[c]	$+2.7(1.0)\times10^{-14}$ (A)	0.08[f]	0.2	0.3	8.8	[53, 89, 134]
SAX J1808.4−3658	$3.3^{+0.3}_{-0.2}$	$-1.01(7)\times10^{-15}$ (Q)	0.04	0.103	0.1	5.6	[53, 58, 135, 136]
		$-3.02(13)\times10^{-13}$ (A)	0.7				
XTE J1814−338	10.25(1)	$-6.7(7)\times10^{-14}$ (A)	0.1	0.069	0.1	6.9	[53, 91, 137]
IGR J18245−2452	5.5[b]	-	-	0.0466	0.1	-	[93, 127, 138]
HETE J1900.1−2455	4.5(2)	$+4.2(1)\times10^{-13}$ (A)	0.4[f]	0.09	0.1	8.4	[53, 96, 139, 140]

[a] Estimate assumes conservative mass transfer during accretion. An alternative estimate gives less than 4 kpc [123].
[b] Uncertainty not quoted as target located in a globular cluster.
[c] Unknown, but as the target is in the direction of the galactic centre a fiducial value of 8 kpc is assumed in the literature.
[d] Lower limit.
[e] Estimate of $\dot{f}_\star$ consistent with zero at a 3σ level.
[f] Assumes $\dot{f}_{\mathrm{GW}} \approx -\dot{f}_\star$, see text for details.

to each target in the second column of Table IV. These estimates are typically poorly known, especially if there is no known counterpart observed in wavelengths other than X-ray for the target. We use the central estimate of the distance in Eq. (12).

For AMXPs, $\dot{f}_\star$ is estimated by constructing a phase-connected timing solution when the target is in outburst, but estimates for $\dot{f}_\star$ in quiescence are also possible for targets that have gone into outburst multiple times. The $\dot{f}_\star$ observed during outburst can be either positive (corresponding to spin-up) or negative (corresponding to spin-down), while in quiescence $\dot{f}_\star$ is typically (but not always) negative [55, 56]. The third column of Table IV records $\dot{f}_\star$ for each of our targets. When $\dot{f}_\star$ has been measured in multiple outburst events, only the $\dot{f}_\star$ from the most recent outburst is listed. For $\dot{f}_\star < 0$ we assume $\dot{f}_{\mathrm{GW}} \approx 2\dot{f}_\star$ in Eq. (12). For targets with $\dot{f}_\star < 0$ (in either quiescent or active phases) we find $10^{-28} \lesssim h_{0,\mathrm{sd}} \lesssim 10^{-27}$ (fourth column of Table IV), an order of magnitude lower than the estimated value of $h_0^{95\%}$.

As argued in Ref. [12], for $\dot{f}_\star > 0$ the torque due to gravitational radiation reaction may be masked by the accretion torque, allowing larger values of $\dot{f}_{\mathrm{GW}}$, as long as one has $\dot{f}_\star = \dot{f}_{\mathrm{acc}} + \dot{f}_{\mathrm{GW}}$, where $\dot{f}_{\mathrm{acc}}$ is the spin-up rate due to accretion. A reasonable choice, without excessive fine-tuning, is to set $\dot{f}_{\mathrm{GW}} \approx -\dot{f}_\star$, for an

order-of-magnitude estimate in Eq. (12), i.e. assuming $|\dot{f}_{\rm acc}| \approx 2|\dot{f}_{\rm GW}|$. The resultant values for $h_{0,\,\rm sd}$ for targets with $\dot{f}_\star > 0$ are all well below the estimates of $h_0^{95\%}$ set in Sec. IX B, and fall in the range $10^{-28} \lesssim h_{0,\,\rm sd} \lesssim 10^{-27}$.

Another avenue through which EM observations can constrain h_0 is by assuming that the X-ray flux is proportional to the mass accretion rate, and that the torque due to accretion balances the gravitational radiation reaction. The torque-balance limit is [18, 46]

$$h_{0,\,\rm torque} = 5\times10^{-27}\left(\frac{600\,\mathrm{Hz}}{f_{\rm GW}}\right)^{1/2} \times\left(\frac{F_X}{10^{-8}\,\mathrm{erg\,s^{-1}\,cm^{-2}}}\right)^{1/2}, \quad (13)$$

where F_X is the observed bolometric X-ray flux. Eq. (13) has a few hidden assumptions, namely: i) that the mass of the neutron star is $1.4M_\odot$, ii) that all of the accretion luminosity is radiated as an X-ray flux, and iii) that the accretion torque is applied at the radius of the neutron star, which is set to 10 km. The exact dependence of the torque-balance limit on these assumptions is discussed in Ref. [18]. We take $f_{\rm GW} \approx 2f_\star$ for each of our targets, as for Eq. (12). We take $F_X = F_{X,\,\rm max}$, the maximum recorded X-ray flux from each target when it was in outburst (fifth column of Table IV), providing an upper limit on $h_{0,\,\rm torque}$ (sixth column of Table IV). We find $5\times10^{-28} \lesssim h_{0,\,\rm torque} \lesssim 1\times10^{-27}$ across all targets.

D. Astrophysical implications

The estimates of $h_0^{95\%}$ given in Sec. IX B can be converted into constraints on the physical parameters that govern the mechanism putatively generating continuous gravitational waves in each sub-band.

In the $2f_\star$ sub-band the simplest emission mechanism is that of a perpendicular biaxial rotator (using the language from Ref. [141]), for which we calculate the upper limit of the ellipticity of the neutron star as [49]

$$\epsilon^{95\%} = 2.1\times10^{-6}\left(\frac{h_0^{95\%}}{10^{-25}}\right)\left(\frac{D}{8\,\mathrm{kpc}}\right)\left(\frac{600\,\mathrm{Hz}}{f_{\rm GW}}\right)^2, \quad (14)$$

assuming $I_{zz} = 10^{38}\,\mathrm{kg\,m^2}$. Using the central estimate for D (second column of Table IV), we find the strictest constraint, from all of our targets, $\epsilon^{95\%} = 3.1\times10^{-7}$ for IGR J00291+5934. A kernel density estimate of the probability density function (PDF) of the constraints $\epsilon^{95\%}$, $\hat{p}(\epsilon^{95\%})$, for all our targets, is shown in the left panel of Fig. 3. It is peaked around $\epsilon^{95\%} \sim 10^{-6}$.

In the $4f_\star/3$ sub-band the emission mechanism is via r-modes, the strength of which is parameterized as [142]

$$\alpha^{95\%} = 1.0\times10^{-4}\left(\frac{h_0^{95\%}}{10^{-25}}\right)\left(\frac{D}{8\,\mathrm{kpc}}\right)\left(\frac{600\,\mathrm{Hz}}{f_{\rm GW}}\right)^3. \quad (15)$$

Eq. (15) assumes $f_{\rm GW} \approx 4f_\star/3$, which may not be true, as discussed in Sec. IV [103, 104]. The strictest constraint, from all of our targets, is $\alpha^{95\%} = 1.8\times10^{-5}$, again for IGR J00291+5934. A kernel density estimate of the PDF of the constraints $\alpha^{95\%}$, $\hat{p}(\alpha^{95\%})$, for all our targets, is shown in the right panel of Fig. 3. It is peaked around $\alpha^{95\%} \sim 10^{-4}$.

The kernel density estimates of the PDFs $\hat{p}(\epsilon^{95\%})$ and $\hat{p}(\alpha^{95\%})$ in Fig. 3 are not constraints on ϵ and α respectively, nor are they expressing the uncertainty in each individual estimate of $\epsilon^{95\%}$ or $\alpha^{95\%}$ (which are dominated by the uncertainty in $h_0^{95\%}$, and the distance, see column two of Table IV). They are instead presented to indicate where the constraints on $\epsilon^{95\%}$ and $\alpha^{95\%}$ lie, given the strain upper limits calculated for the targets in this search. That is, they are estimates of the true probability distribution of the constraints one would obtain for ϵ and α, given a large population of AMXPs (assuming the targets studied here are representative of this larger population). The kernel density estimates are calculated by summing Gaussian kernels centered on each data point, with bandwidth chosen to minimize the asymptotic mean integrated square error [143].

The physical mechanism for emission in the $f_\star$ sub-band is less well-defined. A biaxial non-perpendicular rotator emits gravitational radiation at both $f_\star$ and $2f_\star$ [49, 97, 144]. The emission at $f_\star$ dominates the $2f_\star$ emission for both $\theta \lesssim 20°$ and $|\cos\iota| \lesssim 0.8$, where θ is the wobble angle (see figure 5 of Ref. [141] for details). The value of θ is low for certain models involving pinned superfluid interiors [97, 145]. Other possibilities exist, including a triaxial rotator [146–148]. We recommend future searches to also consider searching the $f_\star$ sub-band, due to the wealth of information that a continuous gravitational wave detection at this frequency would provide regarding neutron star structure.

X. CONCLUSIONS

We present the results of a search for continuous gravitational waves from 20 accreting low-mass X-ray binaries in the Advanced LIGO O3 dataset. Five of these targets were searched before in O2 [12], and one was searched in S6 [42]. The search pipeline we use allows for spin-wandering and tracks the orbital phase of the binary via a hidden Markov model and the $\mathcal{J}$-statistic respectively. The targets have well-constrained rotational frequencies, $f_\star$, and orbital elements from electromagnetic observations of outburst events, restricting the parameter space. For each target we search three ~ 0.61 Hz-wide sub-bands centered on $\{1, 4/3, 2\}f_\star$. We also perform a target-of-opportunity search for emission from SAX J1808.4−3658, which went into outburst during O3a.

We find no candidates that survive our veto procedure and are above a threshold corresponding to a 1% false alarm probability per sub-band. We find 16 candidates that survive our astrophysical vetoes when we set the

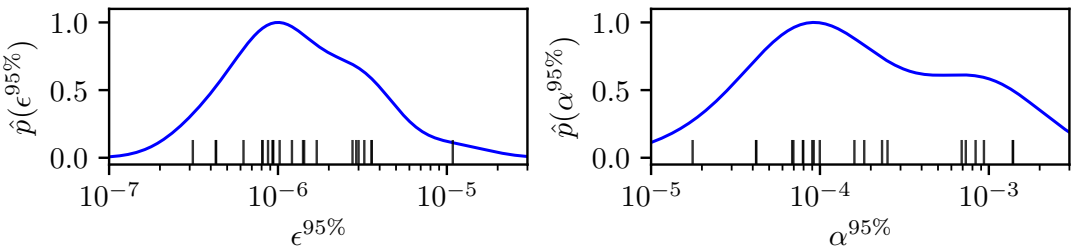

FIG. 3: Kernel density estimate of the PDF of the constraints on ellipticity $\epsilon^{95\%}$ (left panel) and dimensionless r-mode amplitude $\alpha^{95\%}$ (right panel) via Eqs. (14) and (15) respectively. Both PDFs are normalized to a height of one. The black dashes in both panels correspond to the individual estimates of $\epsilon^{95\%}$ or $\alpha^{95\%}$ from each target.

threshold to 30% false alarm probability per sub-band. As we search a total of 60 sub-bands, this number of surviving candidates is consistent with the expected number of false alarms. These candidates are systematically investigated with further follow-up. In all cases, the follow-up does not provide convincing evidence that any are real astrophysical signals. However, they could not be convincingly ruled out, which is not surprising given their borderline significance. We record the orbital template and frequencies recovered for these candidates, and recommend that they are followed up in future gravitational wave data sets, and with different pipelines.

The target-of-opportunity search returns one candidate above threshold that survives our veto procedure. Additional, detailed follow-up of this candidate does not produce convincing evidence that it is a true astrophysical signal rather than a noise fluctuation.

Assuming all of the candidates are not astrophysical, we set upper limits on the strain at 95% confidence in each sub-band. Using these estimates, the strictest constraint on neutron star ellipticity is $\epsilon^{95\%} = 3.1 \times 10^{-7}$. The strictest constraint we place on the r-mode amplitude is $\alpha^{95\%} = 1.8 \times 10^{-5}$. Both of these constraints come from IGR J00291+5934.

ACKNOWLEDGEMENTS

This material is based upon work supported by NSFs LIGO Laboratory which is a major facility fully funded by the National Science Foundation. The authors also gratefully acknowledge the support of the Science and Technology Facilities Council (STFC) of the United Kingdom, the Max-Planck-Society (MPS), and the State of Niedersachsen/Germany for support of the construction of Advanced LIGO and construction and operation of the GEO600 detector. Additional support for Advanced LIGO was provided by the Australian Research Council. The authors gratefully acknowledge the Italian Istituto Nazionale di Fisica Nucleare (INFN), the French Centre National de la Recherche Scientifique (CNRS) and the Netherlands Organization for Scientific Research, for the construction and operation of the Virgo detector and the creation and support of the EGO consortium. The authors also gratefully acknowledge research support from these agencies as well as by the Council of Scientific and Industrial Research of India, the Department of Science and Technology, India, the Science & Engineering Research Board (SERB), India, the Ministry of Human Resource Development, India, the Spanish Agencia Estatal de Investigación, the Vicepresidència i Conselleria d'Innovació, Recerca i Turisme and the Conselleria d'Educació i Universitat del Govern de les Illes Balears, the Conselleria d'Innovació, Universitats, Ciència i Societat Digital de la Generalitat Valenciana and the CERCA Programme Generalitat de Catalunya, Spain, the National Science Centre of Poland and the Foundation for Polish Science (FNP), the Swiss National Science Foundation (SNSF), the Russian Foundation for Basic Research, the Russian Science Foundation, the European Commission, the European Regional Development Funds (ERDF), the Royal Society, the Scottish Funding Council, the Scottish Universities Physics Alliance, the Hungarian Scientific Research Fund (OTKA), the French Lyon Institute of Origins (LIO), the Belgian Fonds de la Recherche Scientifique (FRS-FNRS), Actions de Recherche Concertes (ARC) and Fonds Wetenschappelijk Onderzoek Vlaanderen (FWO), Belgium, the Paris Île-de-France Region, the National Research, Development and Innovation Office Hungary (NKFIH), the National Research Foundation of Korea, the Natural Science and Engineering Research Council Canada, Canadian Foundation for Innovation (CFI), the Brazilian Ministry of Science, Technology, and Innovations, the International Center for Theoretical Physics South American Institute for Fundamental Research (ICTP-SAIFR), the Research Grants Council of Hong Kong, the National Natural Science Foundation of China (NSFC), the Leverhulme Trust, the Research Corporation, the Ministry of Science and Technology (MOST), Taiwan, the United States Department of Energy, and the Kavli Foundation. The authors gratefully acknowledge the support of the NSF, STFC, INFN and CNRS for provision of computational resources. This work was supported by MEXT, JSPS Leading-edge Research Infrastructure Program, JSPS Grant-in-Aid for Specially Promoted Research 26000005, JSPS Grant-in-Aid for Scientific Research on Innovative Areas 2905:

JP17H06358, JP17H06361 and JP17H06364, JSPS Core-to-Core Program A. Advanced Research Networks, JSPS Grant-in-Aid for Scientific Research (S) 17H06133, the joint research program of the Institute for Cosmic Ray Research, University of Tokyo, National Research Foundation (NRF) and Computing Infrastructure Project of KISTI-GSDC in Korea, Academia Sinica (AS), AS Grid Center (ASGC) and the Ministry of Science and Technology (MoST) in Taiwan under grants including AS-CDA-105-M06, Advanced Technology Center (ATC) of NAOJ, and Mechanical Engineering Center of KEK.

This work is supported by NASA through the NICER mission and the Astrophysics Explorers Program and uses data and software provided by the High Energy Astrophysics Science Archive Research Center (HEASARC), which is a service of the Astrophysics Science Division at NASA/GSFC and High Energy Astrophysics Division of the Smithsonian Astrophysical Observatory.

[1] J. Aasi *et al.*, Advanced LIGO, Class. Quantum Grav. **32**, 074001 (2015).
[2] F. Acernese *et al.*, Advanced Virgo: A second-generation interferometric gravitational wave detector, Class. Quantum Grav. **32**, 024001 (2014).
[3] LIGO Scientific Collaboration and Virgo Collaboration *et al.*, GWTC-1: A Gravitational-Wave Transient Catalog of Compact Binary Mergers Observed by LIGO and Virgo during the First and Second Observing Runs, Phys. Rev. X **9**, 031040 (2019).
[4] LIGO Scientific Collaboration and Virgo Collaboration *et al.*, GWTC-2: Compact Binary Coalescences Observed by LIGO and Virgo during the First Half of the Third Observing Run, Phys. Rev. X **11**, 021053 (2021).
[5] The LIGO Scientific Collaboration *et al.*, GWTC-2.1: Deep Extended Catalog of Compact Binary Coalescences Observed by LIGO and Virgo During the First Half of the Third Observing Run, arXiv e-prints , arXiv:2108.01045 (2021).
[6] K. Glampedakis *et al.*, Gravitational Waves from Single Neutron Stars: An Advanced Detector Era Survey, in *The Physics and Astrophysics of Neutron Stars*, Astrophysics and Space Science Library (Springer International Publishing, Cham, 2018) pp. 673–736.
[7] M. Sieniawska and M. Bejger, Continuous Gravitational Waves from Neutron Stars: Current Status and Prospects, Universe **5**, 217 (2019).
[8] B. Haskell and K. Schwenzer, Gravitational waves from isolated neutron stars, arXiv e-prints , arXiv:2104.03137 (2021).
[9] B. P. Abbott *et al.*, Search for Gravitational Waves from a Long-lived Remnant of the Binary Neutron Star Merger GW170817, Astrophys. J. **875**, 160 (2019).
[10] LIGO Scientific Collaboration and Virgo Collaboration *et al.*, Narrow-band search for gravitational waves from known pulsars using the second LIGO observing run, Phys. Rev. D **99**, 122002 (2019).
[11] LIGO Scientific Collaboration and Virgo Collaboration *et al.*, Search for gravitational waves from Scorpius X-1 in the second Advanced LIGO observing run with an improved hidden Markov model, Phys. Rev. D **100**, 122002 (2019).
[12] H. Middleton, P. Clearwater, A. Melatos, and L. Dunn, Search for gravitational waves from five low mass x-ray binaries in the second Advanced LIGO observing run with an improved hidden Markov model, Phys. Rev. D **102**, 023006 (2020).
[13] M. A. Papa *et al.*, Search for Continuous Gravitational Waves from the Central Compact Objects in Supernova Remnants Cassiopeia A, Vela Jr., and G347.3–0.5, Astrophys. J. **897**, 22 (2020).
[14] L. Fesik and M. A. Papa, First Search for r-mode Gravitational Waves from PSR J0537–6910, Astrophys. J. **895**, 11 (2020).
[15] L. Fesik and M. A. Papa, Erratum: "First Search for r-mode Gravitational Waves from PSR J0537–6910" (2020, ApJ, 895, 11), Astrophys. J. **897**, 185 (2020).
[16] O. J. Piccinni *et al.*, Directed search for continuous gravitational-wave signals from the Galactic Center in the Advanced LIGO second observing run, Phys. Rev. D **101**, 082004 (2020).
[17] B. Steltner *et al.*, Einstein@Home All-sky Search for Continuous Gravitational Waves in LIGO O2 Public Data, Astrophys. J. **909**, 79 (2021).
[18] Y. Zhang, M. A. Papa, B. Krishnan, and A. L. Watts, Search for Continuous Gravitational Waves from Scorpius X-1 in LIGO O2 Data, Astrophys. J. **906**, L14 (2021).
[19] D. Beniwal, P. Clearwater, L. Dunn, A. Melatos, and D. Ottaway, Search for continuous gravitational waves from ten H.E.S.S. sources using a hidden Markov model, Phys. Rev. D **103**, 083009 (2021).
[20] D. Jones and L. Sun, Search for continuous gravitational waves from Fomalhaut b in the second Advanced LIGO observing run with a hidden Markov model, Phys. Rev. D **103**, 023020 (2021).
[21] R. Abbott *et al.*, Gravitational-wave Constraints on the Equatorial Ellipticity of Millisecond Pulsars, Astrophys. J. Lett. **902**, L21 (2020).
[22] V. Dergachev and M. A. Papa, Search for continuous gravitational waves from small-ellipticity sources at low frequencies, Phys. Rev. D **104**, 043003 (2021).
[23] B. Rajbhandari, B. J. Owen, S. Caride, and R. Inta, First searches for gravitational waves from r-modes of the Crab pulsar, arXiv e-prints , arXiv:2101.00714 (2021).
[24] The LIGO Scientific Collaboration and the Virgo Collaboration *et al.*, All-sky search in early O3 LIGO data for continuous gravitational-wave signals from unknown neutron stars in binary systems, Phys. Rev. D **103**, 064017 (2021).
[25] K. Wette, L. Dunn, P. Clearwater, and A. Melatos, Deep exploration for continuous gravitational waves at 171–172 Hz in LIGO second observing run data, Phys. Rev. D **103**, 083020 (2021).
[26] R. Abbott *et al.*, Diving below the Spin-down Limit: Constraints on Gravitational Waves from the Energetic Young Pulsar PSR J0537-6910, Astrophys. J. Lett. **913**,

L27 (2021).
[27] The LIGO Scientific Collaboration *et al.*, Constraints from LIGO O3 data on gravitational-wave emission due to r-modes in the glitching pulsar PSR J0537-6910, arXiv e-prints , arXiv:2104.14417 (2021).
[28] The LIGO Scientific Collaboration *et al.*, All-sky Search for Continuous Gravitational Waves from Isolated Neutron Stars in the Early O3 LIGO Data, arXiv e-prints , arXiv:2107.00600 (2021).
[29] R. Abbott *et al.*, Searches for Continuous Gravitational Waves from Young Supernova Remnants in the Early Third Observing Run of Advanced LIGO and Virgo, Astrophys. J. **921**, 80 (2021).
[30] A. Ashok *et al.*, New searches for continuous gravitational waves from seven fast pulsars, arXiv e-prints , arXiv:2107.09727 (2021).
[31] A. Patruno and A. L. Watts, Accreting Millisecond X-ray Pulsars, in *Timing Neutron Stars: Pulsations, Oscillations and Explosions*, Astrophysics and Space Science Library, edited by T. M. Belloni, M. Méndez, and C. Zhang (Springer, Berlin, Heidelberg, 2021) pp. 143–208.
[32] J. W. T. Hessels *et al.*, A Radio Pulsar Spinning at 716 Hz, Science **311**, 1901 (2006).
[33] G. B. Cook, S. L. Shapiro, and S. A. Teukolsky, Rapidly rotating neutron stars in general relativity: Realistic equations of state, Astrophys. J. **424**, 823 (1994).
[34] L. Bildsten, Gravitational Radiation and Rotation of Accreting Neutron Stars, Astrophys. J. Lett. **501**, L89 (1998).
[35] N. Andersson, K. D. Kokkotas, and N. Stergioulas, On the Relevance of the R-Mode Instability for Accreting Neutron Stars and White Dwarfs, Astrophys. J. **516**, 307 (1999).
[36] J. Papaloizou and J. E. Pringle, Gravitational radiation and the stability of rotating stars, Mon. Not. R. Astron. Soc. **184**, 501 (1978).
[37] R. V. Wagoner, Gravitational radiation from accreting neutron stars, Astrophys. J. **278**, 345 (1984).
[38] B. P. Abbott *et al.*, Search for gravitational waves from Scorpius X-1 in the first Advanced LIGO observing run with a hidden Markov model, Phys. Rev. D **95**, 122003 (2017).
[39] B. P. Abbott *et al.*, Upper Limits on Gravitational Waves from Scorpius X-1 from a Model-based Cross-correlation Search in Advanced LIGO Data, Astrophys. J. **847**, 47 (2017).
[40] T. Di Salvo and A. Sanna, Accretion powered X-ray millisecond pulsars, arXiv e-prints , arXiv:2010.09005 (2020).
[41] E. Goetz and K. Riles, An all-sky search algorithm for continuous gravitational waves from spinning neutron stars in binary systems, Class. Quantum Grav. **28**, 215006 (2011).
[42] G. D. Meadors, E. Goetz, K. Riles, T. Creighton, and F. Robinet, Searches for continuous gravitational waves from Scorpius X-1 and XTE J1751-305 in LIGO's sixth science run, Phys. Rev. D **95**, 042005 (2017).
[43] S. Suvorova *et al.*, Hidden Markov model tracking of continuous gravitational waves from a binary neutron star with wandering spin. II. Binary orbital phase tracking, Phys. Rev. D **96**, 102006 (2017).
[44] A. Mukherjee, C. Messenger, and K. Riles, Accretion-induced spin-wandering effects on the neutron star in Scorpius X-1: Implications for continuous gravitational wave searches, Phys. Rev. D **97**, 043016 (2018).
[45] S. Suvorova, L. Sun, A. Melatos, W. Moran, and R. J. Evans, Hidden Markov model tracking of continuous gravitational waves from a neutron star with wandering spin, Phys. Rev. D **93**, 123009 (2016).
[46] K. Riles, Gravitational waves: Sources, detectors and searches, Progress in Particle and Nuclear Physics **68**, 1 (2013).
[47] B. Abbott *et al.*, Beating the Spin-Down Limit on Gravitational Wave Emission from the Crab Pulsar, Astrophys. J. Lett. **683**, L45 (2008).
[48] A. Viterbi, Error bounds for convolutional codes and an asymptotically optimum decoding algorithm, IEEE Trans. Inform. Theory **13**, 260 (1967).
[49] P. Jaranowski, A. Królak, and B. F. Schutz, Data analysis of gravitational-wave signals from spinning neutron stars: The signal and its detection, Phys. Rev. D **58**, 063001 (1998).
[50] LIGO Scientific Collaboration, LIGO Algorithm Library - LALSuite 10.7935/GT1W-FZ16 (2018).
[51] P. Casella, D. Altamirano, A. Patruno, R. Wijnands, and M. van der Klis, Discovery of Coherent Millisecond X-Ray Pulsations in Aquila X-1, Astrophys. J. Lett. **674**, L41 (2008).
[52] D. Mata Sánchez, T. Muñoz-Darias, J. Casares, and F. Jiménez-Ibarra, The donor of Aquila X-1 revealed by high-angular resolution near-infrared spectroscopy, Mon. Not. R. Astron. Soc. **464**, L41 (2017).
[53] A. L. Watts, B. Krishnan, L. Bildsten, and B. F. Schutz, Detecting gravitational wave emission from the known accreting neutron stars, Mon. Not. R. Astron. Soc. **389**, 839 (2008).
[54] A. Marino *et al.*, Indications of non-conservative mass transfer in AMXPs, Astron. Astrophys. **627**, 11 (2019).
[55] A. Melatos and A. Mastrano, Electromagnetic Spin-down of a Transient Accreting Millisecond Pulsar During Quiescence, Astrophys. J. **818**, 49 (2016).
[56] P. Ghosh, F. K. Lamb, and C. J. Pethick, Accretion by rotating magnetic neutron stars. I - Flow of matter inside the magnetosphere and its implications for spin-up and spin-down of the star, Astrophys. J. **217**, 578 (1977).
[57] P. M. Bult *et al.*, NICER detects X-ray pulsations from the rapidly brightening SAX J1808.4-3658, The Astronomer's Telegram **3001** (2019).
[58] P. Bult *et al.*, Timing the Pulsations of the Accreting Millisecond Pulsar SAX J1808.4–3658 during Its 2019 Outburst, Astrophys. J. **898**, 38 (2020), arXiv:1910.03062.
[59] A. J. Goodwin *et al.*, Enhanced optical activity 12 d before X-ray activity, and a 4 d X-ray delay during outburst rise, in a low-mass X-ray binary, Mon. Not. R. Astron. Soc. **498**, 3429 (2020).
[60] B. Haskell and A. Patruno, Are Gravitational Waves Spinning Down PSR J1023+0038?, Phys. Rev. Lett. **119**, 161103 (2017).
[61] M. A. P. Torres *et al.*, Observations of the 599 Hz Accreting X-Ray Pulsar IGR J00291+5934 during the 2004 Outburst and in Quiescence, Astrophys. J. **672**, 1079 (2008).
[62] A. Patruno, The Slow Orbital Evolution of the Accreting Millisecond Pulsar IGR J0029+5934, Astrophys. J. **839**, 51 (2017).

[63] J. Homan *et al.*, Chandra identification of the X-ray transient MAXI J0911-635/Swift J0911.9-6452 in NGC 2808, The Astronomer's Telegram **8971** (2016).

[64] A. Sanna *et al.*, Discovery of a new accreting millisecond X-ray pulsar in the globular cluster NGC 2808, Astron. Astrophys. **598**, A34 (2017).

[65] D. K. Galloway, D. Chakrabarty, E. H. Morgan, and R. A. Remillard, Discovery of a High-Latitude Accreting Millisecond Pulsar in an Ultracompact Binary, Astrophys. J. Lett. **576**, L137 (2002).

[66] A. B. Giles, J. G. Greenhill, K. M. Hill, and E. Sanders, The optical counterpart of XTE J0929-314: The third transient millisecond X-ray pulsar, Mon. Not. R. Astron. Soc. **361**, 1180 (2005).

[67] A. J. Tetarenko *et al.*, A Radio Frequency Study of the Accreting Millisecond X-ray Pulsar, IGR J16597-3704, in the Globular Cluster NGC 6256, Astrophys. J. **854**, 125 (2018).

[68] A. Sanna *et al.*, Discovery of 105 Hz coherent pulsations in the ultracompact binary IGR J16597-3704, Astron. Astrophys. **610**, L2 (2018).

[69] P. Bult, T. E. Strohmayer, C. Malacaria, M. Ng, and Z. Wadiasingh, Long-term Coherent Timing of the Accreting Millisecond Pulsar IGR J17062–6143, Astrophys. J. **912**, 120 (2021).

[70] A. Sanna *et al.*, XMM-Newton detection of the 2.1 ms coherent pulsations from IGR J17379-3747, Astron. Astrophys. **616**, L17 (2018).

[71] P. Bult *et al.*, On the Curious Pulsation Properties of the Accreting Millisecond Pulsar IGR J17379-3747, Astrophys. J. **877**, 70 (2019).

[72] A. Sanna *et al.*, Timing of the accreting millisecond pulsar SAX J1748.9-2021 during its 2015 outburst, Mon. Not. R. Astron. Soc. **459**, 1340 (2016).

[73] C. O. Heinke *et al.*, Discovery of a Second Transient Low-Mass X-ray Binary in the Globular Cluster Ngc 6440, Astrophys. J. **714**, 894 (2010).

[74] P. Bult, A. Patruno, and M. van der Klis, Coherent Timing of the Accreting Millisecond Pulsar NGC 6440 X-2, Astrophys. J. **814**, 138 (2015).

[75] M. Ng *et al.*, NICER Discovery of Millisecond X-Ray Pulsations and an Ultracompact Orbit in IGR J17494-3030, Astrophys. J. Lett. **908**, L15 (2021).

[76] P. G. Jonker, M. A. P. Torres, D. Steeghs, and D. Chakrabarty, Chandra X-ray and Gemini near-infrared observations of the eclipsing millisecond pulsar SWIFT J1749.4-2807 in quiescence, Mon. Not. R. Astron. Soc. **429**, 523 (2013).

[77] P. M. Bult *et al.*, NICER detects pulsations from Swift J1749.4-2807, The Astronomer's Telegram **4428** (2021).

[78] A. Sanna *et al.*, NICER timing of millisecond X-ray pulsar SWIFT J1749.4-2807 during its 2021 outburst, in preparation.

[79] A. Papitto *et al.*, The discovery of the 401 Hz accreting millisecond pulsar IGR J17498-2921 in a 3.8 h orbit, Astron. Astrophys. **535**, L4 (2011).

[80] M. Falanga *et al.*, Spectral and timing properties of the accreting X-ray millisecond pulsar IGR J17498-2921, Astron. Astrophys. **545**, A26 (2012).

[81] A. Paizis *et al.*, A Chandra Observation of the Bursting Millisecond X-Ray Pulsar IGR J17511-3057, Astrophys. J. **755**, 52 (2012).

[82] A. Riggio *et al.*, Timing of the accreting millisecond pulsar IGR J17511-3057, Astron. Astrophys. **526**, A95 (2011).

[83] C. B. Markwardt, J. H. Swank, T. E. Strohmayer, J. J. M. in 't Zand, and F. E. Marshall, Discovery of a Second Millisecond Accreting Pulsar: XTE J1751-305, Astrophys. J. Lett. **575**, L21 (2002).

[84] A. Papitto, M. T. Menna, L. Burderi, T. di Salvo, and A. Riggio, Measuring the spin up of the accreting millisecond pulsar XTEJ1751-305, Mon. Not. R. Astron. Soc. **383**, 411 (2008).

[85] A. Sanna *et al.*, SWIFT J1756.9-2508: Spectral and timing properties of its 2018 outburst, Mon. Not. R. Astron. Soc. **481**, 1658 (2018).

[86] T. D. Russell *et al.*, The Radio-bright Accreting Millisecond X-Ray Pulsar IGR J17591-2342, Astrophys. J. Lett. **869**, L16 (2018).

[87] A. Sanna *et al.*, Timing of the accreting millisecond pulsar IGR J17591–2342: Evidence of spin-down during accretion, Mon. Not. R. Astron. Soc. **495**, 1641 (2020).

[88] C. B. Markwardt, M. Juda, and J. H. Swank, XTE J1807-294, International Astronomical Union Circular **8095**, 2 (2003).

[89] A. Patruno, J. M. Hartman, R. Wijnands, D. Chakrabarty, and M. van der Klis, Accretion Torques and Motion of the Hot Spot on the Accreting Millisecond Pulsar XTE J1807-294, Astrophys. J. **717**, 1253 (2010).

[90] M. I. Krauss *et al.*, The X-Ray Position and Optical Counterpart of the Accretion-powered Millisecond Pulsar XTE J1814-338, Astrophys. J. **627**, 910 (2005).

[91] A. Papitto *et al.*, Timing of the accreting millisecond pulsar XTE J1814-338, Mon. Not. R. Astron. Soc. **375**, 971 (2007).

[92] C. Pallanca, E. Dalessandro, F. R. Ferraro, B. Lanzoni, and G. Beccari, The Optical Counterpart to the X-Ray Transient IGR J1824-24525 in the Globular Cluster M28, Astrophys. J. **773**, 122 (2013).

[93] A. Papitto *et al.*, Swings between rotation and accretion power in a binary millisecond pulsar, Nature **501**, 517 (2013).

[94] D. B. Fox, HETE J1900.1-2455 Optical Counterpart, The Astronomer's Telegram **526** (2005).

[95] P. Kaaret, E. H. Morgan, R. Vanderspek, and J. A. Tomsick, Discovery of the Millisecond X-Ray Pulsar HETE J1900.1-2455, Astrophys. J. **638**, 963 (2006).

[96] A. Patruno, Evidence of Fast Magnetic Field Evolution in an Accreting Millisecond Pulsar, Astrophys. J. Lett. **753**, L12 (2012).

[97] D. I. Jones, Gravitational wave emission from rotating superfluid neutron stars, Mon. Not. R. Astron. Soc. **402**, 2503 (2010).

[98] N. Andersson, A New Class of Unstable Modes of Rotating Relativistic Stars, Astrophys. J. **502**, 708 (1998).

[99] J. L. Friedman and S. M. Morsink, Axial Instability of Rotating Relativistic Stars, Astrophys. J. **502**, 714 (1998).

[100] S. Yoshida and U. Lee, R-Modes of Neutron Stars with a Solid Crust, Astrophys. J. **546**, 1121 (2001).

[101] M. G. Alford, S. Mahmoodifar, and K. Schwenzer, Viscous damping of r-modes: Small amplitude instability, Phys. Rev. D **85**, 024007 (2012).

[102] LIGO Scientific Collaboration and Virgo Collaboration *et al.*, First narrow-band search for continuous gravitational waves from known pulsars in advanced detector data, Phys. Rev. D **96**, 122006 (2017).

[103] A. Idrisy, B. J. Owen, and D. I. Jones, R-mode frequencies of slowly rotating relativistic neutron stars with realistic equations of state, Phys. Rev. D **91**, 024001 (2015).

[104] S. Caride, R. Inta, B. J. Owen, and B. Rajbhandari, How to search for gravitational waves from r-modes of known pulsars, Phys. Rev. D **100**, 064013 (2019).

[105] L. Sammut, C. Messenger, A. Melatos, and B. J. Owen, Implementation of the frequency-modulated sideband search method for gravitational waves from low mass x-ray binaries, Phys. Rev. D **89**, 043001 (2014).

[106] C. Messenger *et al.*, Gravitational waves from Scorpius X-1: A comparison of search methods and prospects for detection with advanced detectors, Phys. Rev. D **92**, 023006 (2015).

[107] LIGO Scientific Collaboration and Virgo Collaboration *et al.*, All-sky search for continuous gravitational waves from isolated neutron stars using Advanced LIGO O2 data, Phys. Rev. D **100**, 024004 (2019).

[108] A. Patruno *et al.*, Accelerated Orbital Expansion and Secular Spin-down of the Accreting Millisecond Pulsar SAX J1808.4-3658, Astrophys. J. Lett. **746**, L27 (2012).

[109] P. Leaci and R. Prix, Directed searches for continuous gravitational waves from binary systems: Parameter-space metrics and optimal Scorpius X-1 sensitivity, Phys. Rev. D **91**, 102003 (2015).

[110] D. Davis *et al.*, LIGO detector characterization in the second and third observing runs, Class. Quantum Grav. **38**, 135014 (2021).

[111] J. Zweizig and K. Riles, LIGO-T2000384-v4: Information on self-gating of h(t) used in O3 continuous-wave and stochastic searches.

[112] L. Sun *et al.*, Characterization of systematic error in Advanced LIGO calibration, Class. Quantum Grav. **37**, 225008 (2020).

[113] L. Sun *et al.*, Characterization of systematic error in Advanced LIGO calibration in the second half of O3, arXiv e-prints , arXiv:2107.00129 (2021).

[114] LSC Instrument Authors *et al.*, Identification and mitigation of narrow spectral artifacts that degrade searches for persistent gravitational waves in the first two observing runs of Advanced LIGO, Phys. Rev. D **97**, 082002 (2018).

[115] E. Goetz *et al.*, LIGO-T2100200-v1: O3 lines and combs in found in self-gated C01 data.

[116] M. M. Romanova, G. V. Ustyugova, A. V. Koldoba, and R. V. E. Lovelace, Three-dimensional Simulations of Disk Accretion to an Inclined Dipole. II. Hot Spots and Variability, Astrophys. J. **610**, 920 (2004).

[117] B. Haskell *et al.*, Detecting gravitational waves from mountains on neutron stars in the advanced detector era, Mon. Not. R. Astron. Soc. **450**, 2393 (2015).

[118] A. Gelman *et al.*, *Bayesian Data Analysis*, 3rd ed. (Chapman and Hall/CRC, New York, 2013).

[119] A. Papitto *et al.*, Spin down during quiescence of the fastest known accretion-powered pulsar, Astron. Astrophys. **528**, A55 (2011).

[120] A. Sanna *et al.*, Spectral and timing properties of IGR J00291+5934 during its 2015 outburst, Mon. Not. R. Astron. Soc. **466**, 2910 (2017).

[121] V. De Falco *et al.*, The 2015 outburst of the accretion-powered pulsar IGR J00291+5934: INTEGRAL and Swift observations, Astron. Astrophys. **599**, A88 (2017).

[122] L. L. Watkins, R. P. van der Marel, A. Bellini, and J. Anderson, Hubble Space Telescope Proper Motion (HSTPROMO) Catalogs of Galactic Globular Clusters. III. Dynamical Distances and Mass-to-Light Ratios, Astrophys. J. **812**, 149 (2015).

[123] A. Marino *et al.*, Evidence of a non-conservative mass transfer for XTE J0929-314, Astron. Astrophys. **603**, A137 (2017).

[124] L. Keek *et al.*, X-Ray Reflection and an Exceptionally Long Thermonuclear Helium Burst from IGR J17062-6143, Astrophys. J. **836**, 111 (2017).

[125] J. van den Eijnden *et al.*, VLA radio detection of the very-faint X-ray transient IGR J17379-3747, The Astronomer's Telegram **1487** (2018).

[126] H. Negoro *et al.*, MAXI/GSC detection of renewed activity from the gamma-ray source IGR J17379-3747, The Astronomer's Telegram **1447** (2018).

[127] W. E. Harris, A New Catalog of Globular Clusters in the Milky Way, arXiv e-prints , arXiv:1012.3224 (2010).

[128] R. Sharma, A. Beri, A. Sanna, and A. Dutta, A broadband look of the accreting millisecond X-ray pulsar SAX J1748.9-2021 using AstroSat and XMM-Newton, Mon. Not. R. Astron. Soc. **492**, 4361 (2020).

[129] R. Wijnands, E. Rol, E. Cackett, R. L. C. Starling, and R. A. Remillard, GRB060602B = Swift J1749.4-2807: An unusual transiently accreting neutron-star X-ray binary, Mon. Not. R. Astron. Soc. **393**, 126 (2009).

[130] M. Linares *et al.*, RXTE detection of a thermonuclear burst from IGR J17498-2921: Distance estimate and burst oscillations, The Astronomer's Telegram **3568** (2011).

[131] A. Riggio *et al.*, Secular spin-down of the AMP XTE J1751-305, Astron. Astrophys. **531**, A140 (2011).

[132] N. V. Gusinskaia *et al.*, Radio and X-ray monitoring of the accreting millisecond X-ray pulsar IGR J17591-2342 in outburst, Mon. Not. R. Astron. Soc. **492**, 1091 (2020).

[133] L. Kuiper *et al.*, High-energy characteristics of the accretion-powered millisecond pulsar IGR J17591-2342 during its 2018 outburst. XMM-Newton, NICER, NuSTAR, and INTEGRAL view of the 0.3-300 keV X-ray band, Astron. Astrophys. **641**, A37 (2020).

[134] A. Riggio *et al.*, Spin-up and Phase Fluctuations in the Timing of the Accreting Millisecond Pulsar XTE J1807-294, Astrophys. J. **678**, 1273 (2008).

[135] D. K. Galloway and A. Cumming, Helium-rich Thermonuclear Bursts and the Distance to the Accretion-powered Millisecond Pulsar SAX J1808.4-3658, Astrophys. J. **652**, 559 (2006).

[136] A. J. Goodwin, D. K. Galloway, A. Heger, A. Cumming, and Z. Johnston, A Bayesian approach to matching thermonuclear X-ray burst observations with models, Mon. Not. R. Astron. Soc. **490**, 2228 (2019).

[137] P. D'Avanzo *et al.*, The optical counterparts of accreting millisecond X-ray pulsars during quiescence, Astron. Astrophys. **508**, 297 (2009).

[138] S. Campana *et al.*, Accreting Pulsars: Mixing-up Accretion Phases in Transitional Systems, in *The Physics and Astrophysics of Neutron Stars*, Astrophysics and Space Science Library (Springer International Publishing, Cham, 2018) pp. 149–184.

[139] M. Suzuki *et al.*, Discovery of a New X-Ray Burst/Millisecond Accreting Pulsar, HETE J1900.1-2455, Publ. Astron. Soc. Jpn. **59**, 263 (2007).

[140] D. K. Galloway, M. P. Muno, J. M. Hartman, D. Psaltis,

and D. Chakrabarty, Thermonuclear (Type I) X-Ray Bursts Observed by the Rossi X-Ray Timing Explorer, Astrophys. J. Suppl. Ser. **179**, 360 (2008).
[141] L. Sun, A. Melatos, and P. D. Lasky, Tracking continuous gravitational waves from a neutron star at once and twice the spin frequency with a hidden Markov model, Phys. Rev. D **99**, 123010 (2019).
[142] B. J. Owen, How to adapt broad-band gravitational-wave searches for r-modes, Phys. Rev. D **82**, 104002 (2010).
[143] M. P. Wand and M. C. Jones, *Kernel Smoothing* (Chapman & Hall, London; New York, 1995).
[144] D. I. Jones, Parameter choices and ranges for continuous gravitational wave searches for steadily spinning neutron stars, Mon. Not. R. Astron. Soc. **453**, 53 (2015).
[145] A. Melatos, J. A. Douglass, and T. P. Simula, Persistent Gravitational Radiation from Glitching Pulsars, Astrophys. J. **807**, 132 (2015).
[146] M. Zimmermann, Gravitational waves from rotating and precessing rigid bodies. II. General solutions and computationally useful formulas, Phys. Rev. D **21**, 891 (1980).
[147] C. V. D. Broeck, The gravitational wave spectrum of non-axisymmetric, freely precessing neutron stars, Class. Quantum Grav. **22**, 1825 (2005).
[148] P. D. Lasky and A. Melatos, Tilted torus magnetic fields in neutron stars and their gravitational wave signatures, Phys. Rev. D **88**, 103005 (2013).
[149] M. Millhouse, L. Strang, and A. Melatos, Search for gravitational waves from 12 young supernova remnants with a hidden Markov model in Advanced LIGO's second observing run, Phys. Rev. D **102**, 083025 (2020).
[150] G. Ashton and R. Prix, Hierarchical multistage MCMC follow-up of continuous gravitational wave candidates, Phys. Rev. D **97**, 103020 (2018).
[151] D. Keitel, R. Tenorio, G. Ashton, and R. Prix, PyFstat: A Python package for continuous gravitational-wave data analysis, J. Open Source Softw. **6**, 3000 (2021).
[152] P. B. Covas and A. M. Sintes, First All-Sky Search for Continuous Gravitational-Wave Signals from Unknown Neutron Stars in Binary Systems Using Advanced LIGO Data, Phys. Rev. Lett. **124**, 191102 (2020).
[153] R. Tenorio, D. Keitel, and A. M. Sintes, Application of a hierarchical MCMC follow-up to Advanced LIGO continuous gravitational-wave candidates, Phys. Rev. D **104**, 084012 (2021).
[154] D. Foreman-Mackey, D. W. Hogg, D. Lang, and J. Goodman, Emcee: The MCMC Hammer, Publ. Astron. Soc. Pac. **125**, 306 (2013).
[155] W. D. Vousden, W. M. Farr, and I. Mandel, Dynamic temperature selection for parallel tempering in Markov chain Monte Carlo simulations, Mon. Not. R. Astron. Soc. **455**, 1919 (2016).

Appendix A: Threshold setting

In this Appendix we outline two alternative methods to set thresholds for the search. In Appendix A 1 we detail the method in Ref. [11] to set thresholds by modeling the tail of the log-likelihood distribution in noise as an exponential. In Appendix A 2 we review the non-parametric method in Refs. [12, 19, 20, 38, 149], which takes a certain percentile detection statistic from noise-only realizations as the threshold. We compare the methods in Appendix A 3. In Appendix A 4 we discuss generating noise realizations using off-target searches, and justify the approach taken in this paper. In Appendix A 5 we specify how to calculate $p_{\rm noise}$, the probability that we see a value of $\mathcal{L}$ at least as high as a certain candidate in a given sub-band.

Whatever the method, the threshold depends on both the target's projected semi-major axis, a_0, and the sub-band frequency, f, as log-likelihoods depend non-linearly on $a_0\,f$ as an increased number orbital sidebands are included in the $\mathcal{J}$-statistic at higher $a_0\,f$ [see equation (6) in Ref. [11] and Ref. [43] for details]. For this reason we set thresholds independently for each target and sub-band.

1. Exponential tail method

The PDF of the log-likelihood, $p(\mathcal{L})$, for the most likely path for a given template is observed to have an exponentially distributed tail in noise,

$$p(\mathcal{L}) = A\lambda \exp\left[-\lambda\left(\mathcal{L}-\mathcal{L}_{\rm tail}\right)\right] \quad \text{for} \quad \mathcal{L} > \mathcal{L}_{\rm tail}\ , \tag{A1}$$

where A is a normalization constant, λ is a parameter to be found empirically, and $\mathcal{L}_{\rm tail}$ is a cut-off that must also be determined empirically.

For each target and sub-band we estimate λ and $\mathcal{L}_{\rm tail}$ using a set of M sample log-likelihoods, a subset of which have $\mathcal{L} > \mathcal{L}_{\rm tail}$. This subset is denoted $S_{N_{\rm tail}} \equiv \{\mathcal{L}_i\}$, $i \in \{1, ..., N_{\rm tail}\}$. The entire set of M samples is generated by running the search on $N_{\rm G} = 100$ realizations of Gaussian noise. To keep $N_{\rm G}$ small enough to be computationally feasible we include log-likelihoods from all possible Viterbi paths through the sub-band for each template, instead of just the log-likelihood from the most likely path. Thus, we have $M = N_{\rm G} N_f N_B$, where $N_f = 2^{20}$ is the number of frequency bins in each sub-band, and N_B is the number of binary orbital templates needed for each individual sub-band, as listed in Table II. Separate tests, not shown here, indicate that including the log-likelihoods from non-maximal paths does not change the shape of $p(\mathcal{L})$, and therefore does not change the thresholds $\mathcal{L}_{\rm th}$, if the appropriate trials factor is taken into account.

Assuming each $\mathcal{L}_i$ is independent, the maximum likelihood estimator, $\hat{\lambda}$, for λ is

$$\hat{\lambda} = \frac{N_{\rm tail}}{\sum_{i=1}^{N_{\rm tail}} \left(\mathcal{L}_i - \mathcal{L}_{\rm tail}\right)}\ . \tag{A2}$$

The normalization $A = N_{\rm tail}/M$ is fixed via the fraction of total samples used to construct $p(\mathcal{L})$. The cut-off $\mathcal{L}_{\rm tail}$ is estimated in each sub-band as the smallest value $\mathcal{L}^*$ where a histogram of the samples $\mathcal{L}_i > \mathcal{L}^*$ has approximately constant slope when viewed on log-linear axes. Each $\mathcal{L}_i$ is independent for the long coherence times ($T_{\rm drift} = 10\,{\rm d}$) used in this search, as $N_T \ll N_f$ implies

most optimal paths through the sub-band are not correlated.

The probability, α, that $\mathcal{L}$ is above some threshold $\mathcal{L}_{\rm th} > \mathcal{L}_{\rm tail}$ if no signal is present (i.e. in pure noise) is

$$\int_{\mathcal{L}_{\rm th}}^{\infty} {\rm d}\mathcal{L}\, p(\mathcal{L}) = \alpha \ . \tag{A3}$$

Combining Eqs. (8), (A1), and (A3) we solve for $\mathcal{L}_{\rm th}$ in a given sub-band, viz.

$$\mathcal{L}_{\rm th} = -\frac{1}{\hat{\lambda}} \log\left(\frac{N_{\rm G}\alpha_{N_{\rm tot}}}{N_{\rm tail}}\right) + \mathcal{L}_{\rm tail} \ , \tag{A4}$$

where Eq. (8) is simplified via the binomial approximation ($N_{\rm tot} = N_f N_B \gg 1$), and $\alpha_{N_{\rm tot}}$ is the desired false alarm probability for the search over the sub-band. Note Eq. (A4) depends implicitly on the sub-band frequency and N_B, through $\hat{\lambda}$ and $N_{\rm tail}$.

Across all targets and sub-bands we find $0.195 < \hat{\lambda} < 0.248$, with larger values corresponding to higher frequency sub-bands, and those with larger N_B. A simple rule-of-thumb is that, for a median value of $\hat{\lambda} = 0.218$, an increment of ≈ 3 in $\mathcal{L}$ is $\approx 50\%$ less likely to occur in pure noise.

2. Percentile method

Given a sorted set of most likely log-likelihoods $\{\mathcal{L}_i\}$, $i \in \{1, ..., M\}$ with $M = N_{\rm G} N_B$, generated via running the search algorithm over $N_{\rm G}$ realizations of noise for a single target and sub-band, one can pick as the threshold the $\mathcal{L}_i$ corresponding to the percentile equal to the desired false alarm probability, i.e.

$$\mathcal{L}_{\rm th} = \mathcal{L}_j \ , \tag{A5}$$

with $j = \lfloor \alpha_{N_{\rm tot}} M \rfloor$. As with the method described in Appendix A 1 we may opt to use the log-likelihoods from all possible Viterbi paths through the sub-band for a given orbital template, to reduce the number of realizations of noise we need to generate. With this set of log-likelihoods, we have $M = N_{\rm G} N_f N_B$.

3. Comparison of methods

The two methods described in Appendices A 1 and A 2 give broadly similar results for $\mathcal{L}_{\rm th}$ for a given probability of false alarm. Ref. [11] opts for the method in Appendix A 1. When Viterbi scores are used as the detection statistic, as in Ref. [11], the PDF of the score in noise does not vary with frequency, and thus the thresholds in each sub-band can be extrapolated from a small set of Gaussian noise realizations. If the PDF of the detection statistic varies with target search parameters, then the method in Appendix A 2 is used, as in Refs. [12, 19, 20, 149]. The percentile method has inherently fewer assumptions, as it does not fit a parametric model to $p(\mathcal{L})$. However it is not possible to extrapolate thresholds calculated in one sub-band to other sub-bands.

For our targets and sub-bands, we find $\mathcal{L}^e_{\rm th} - \mathcal{L}^p_{\rm th} \approx 2$, where the superscripts e and p correspond to the exponential tail and percentile methods respectively. However the exact difference depends on the realizations of Gaussian noise; Monte Carlo simulations indicate that with $N_{\rm G} = 100$ the calculated threshold is usually within 2% of the true value, so thresholds should only be considered precise to 2%.

4. Off-target thresholds

Both methods derive $\mathcal{L}_{\rm th}$ based on realizations of Gaussian noise. However, the noise in real detector data is non-Gaussian in general [110]. To account for this we search O3 data at $N_{\rm OT}$ randomly chosen, but well-separated, off-target positions, to generate $N_{\rm OT}$ realizations of real detector noise, as originally done in Ref. [12]. We set $N_{\rm OT}$ such that $N_B N_{\rm OT} > 500$, with a minimum value of $N_{\rm OT} = 100$, to ensure enough samples are generated.

If there are no known noise lines in the sub-band, we find $4 < \mathcal{L}^e_{\rm th,\,G} - \mathcal{L}^p_{\rm th,\,OT} < 12$, where the subscripts G and OT correspond to thresholds calculated using Gaussian and off-target noise realizations respectively. That is, the thresholds calculated from Gaussian noise, using the exponential tail method are considerably more conservative than those calculated from off-target noise and the percentile method. If there are loud noise lines in the sub-band, $\mathcal{L}_{\rm th,\,OT}$ is often much higher, as these lines appear in the off-target noise realizations. Because off-target noise realizations are impacted by noise lines, $p(\mathcal{L})$ is not necessarily exponential in its tail. We thus opt to use the percentile method when calculating thresholds with off-target noise realizations. Table V contains the calculated $\mathcal{L}^e_{\rm th,\,G}$ and $\mathcal{L}^p_{\rm th,\,OT}$ for each target and sub-band.

As in Ref. [12] we consider $\mathcal{L}_{\rm th}$ for each sub-band to be the minimum of $\mathcal{L}^e_{\rm th,\,G}$ and $\mathcal{L}^p_{\rm th,\,OT}$, with $\alpha_{N_{\rm tot}} = 0.3$. This choice minimizes the probability that we will miss a potential candidate due to inadvertently setting our threshold too high.

5. Probability that a candidate arises due to noise

As discussed in Sec. IV C, when we set $\alpha_{N_{\rm tot}} = 0.3$ we expect ~ 18 candidates above $\mathcal{L}_{\rm th}$, across all targets and sub-bands. Let us quantify empirically the probability, $p_{\rm noise}$, that, if the data in a given sub-band are pure noise, we see at least one template with log-likelihood higher than that of the candidate, $\mathcal{L}_{\rm cand}$. We have

$$p_{\rm noise} = \frac{\sum_{i=1}^{M} \mathbb{1}\left(\mathcal{L}_i > \mathcal{L}_{\rm cand}\right)}{M} \ , \tag{A6}$$

where $\mathbb{1}(...)$ is the indicator function which returns 1 when the argument is true, otherwise 0. In this paper we calculate Eq. (A6) for each candidate with $\mathcal{L} > \mathcal{L}_{\rm th}$ using the set of log-likelihoods, $\{\mathcal{L}_i\}$, generated via off-target realizations as discussed in Appendix A 4. As in Appendix A 2, we set $M = N_{\rm G}N_B$ to account for the extra "trials factor" needed for sub-bands with multiple templates.

Appendix B: Full search results and survivor follow-up

This Appendix collates the full search results for reference and reproducibility for all targets in Figs. 4a–4s (except for IGR J18245−2452 which is shown in Fig. 2). Each of Figs. 4a–4s is laid out identically to Fig. 2.

The orbital parameters (P, a_0, and $T_{\rm asc}$), terminating frequency bin $[f(N_T)]$, log-likelihood ($\mathcal{L}$), and $p_{\rm noise}$, the probability that a search of that candidate's sub-band in pure noise would return at least one candidate at least as loud as the one seen are shown in Table VI, for each of the candidates that survive all vetoes and have $\mathcal{L} > \mathcal{L}_{\rm th}$.

1. Additional follow-up for survivors

The full frequency paths, $f(t) - f(N_T)$, for all candidates with $p_{\rm noise} \leq 0.1$ are shown in the top panels of Figs. 5a–5e. The bottom panels of Figs. 5a–5e display the cumulative log-likelihood along the frequency path relative to the average sum log-likelihood needed to reach $\mathcal{L}_{\rm th}$, namely $C\mathcal{L} \equiv \sum_{i=0}^{i=t}\left[\mathcal{L}(i) - \mathcal{L}_{\rm th}/N_T\right]$, where $\sum_{i=0}^{i=t}\mathcal{L}(i)$ is $\ln P(Q^*|O)$ from Eq. (2) truncated after the t-th segment. Over-plotted (blue dashed line) is the average cumulative log-likelihood needed at each data segment in order to reach $\mathcal{L}_{\rm th}$. This diagnostic indicates whether a handful of segments dominate in making the candidate's frequency path the optimal one for that template. If the candidate is a true signal, we would expect the signal strength to be approximately constant, and thus the cumulative log-likelihood should grow linearly as more data are considered. However, Monte Carlo tests with injections show that the cumulative log-likelihood only becomes linear for $\mathcal{L} \gtrsim \mathcal{L}_{\rm th} + 200$. This is not the case for any of the 16 survivor candidates, and thus their cumulative log-likelihood cannot help us distinguish whether they are truly astrophysical signals.

The sky resolution of the algorithm described in Sec. II is roughly 2 arcmin in RA and Dec., for an injection with $\mathcal{L}_{\rm th} \lesssim \mathcal{L} \lesssim \mathcal{L}_{\rm th} + 50$. The point-spread-function of an injection is an ellipse, which has a varying orientation and eccentricity dependent on the sky position. For each of our candidates we calculate $\mathcal{L}$ at 440 regularly spaced sky positions in a 100 arcmin^2 grid around the target's true location, using the template recovered from the search and listed in Table VI. For almost all survivor candidates, the distribution of $\mathcal{L}$ values in the patch of sky around the candidate does not match the elliptical point-spread-function we see in injections for their respective sky locations. The sole exception is Candidate 2 from IGR J16597−3704. Figure 6 shows $\mathcal{L}$ at 3721 regularly spaced sky positions in a 100 arcmin^2 grid around the target's true location, again using the template as listed in Table VI. The roughly elliptical shape is consistent with the point-spread-function of injections at this sky location. However, the region of sky with $\mathcal{L} \gtrsim \mathcal{L}_{\rm th}$ is centered ~ 1 arcmin lower in Dec. than the true declination of the source, which is known to a precision of 0.01 arcmin [67].

One final follow-up we perform for these candidates is to calculate $\mathcal{L}$ in a small, densely sampled patch of the $\{P,\ T_{\rm asc}\}$ parameter space around each candidate's template. Moderately loud injections ($\mathcal{L} \gtrsim \mathcal{L}_{\rm th} + 100$) are seen to "spread out" in the $\{P,\ T_{\rm asc}\}$ plane, and are detectable with $\mathcal{L} > \mathcal{L}_{\rm th}$ even when searching a template that has a slightly incorrect value of P and $T_{\rm asc}$. However, none of our candidates are this loud, so this diagnostic does not help us distinguish whether they are truly astrophysical signals or merely noise fluctuations.

We do not use any data from LIGO's Observing Runs 1 or 2 (O1 and O2 respectively) to aid in following up these candidates, as the detector is considerably more sensitive in O3. The duration of O3 was also longer than the durations of O1 and O2. If a candidate is only marginally above threshold in O3 data, it may be hidden in the noise in O1 and O2 data, so including data from those observing runs is not likely to increase the candidate's signal-to-noise ratio.

Appendix C: Survivor follow-up for target-of-opportunity search candidate

For posterity, and to aid future follow-up with different pipelines, we record in Table VII the template, the frequency f, the log-likelihood $\mathcal{L}$, and $p_{\rm noise}$, of the candidate from the target-of-opportunity search in Sec. VIII that survives all vetoes.

As in Appendix B 1, we perform additional follow-up for this remaining candidate. With $T_{\rm obs} = 24$ d the point-spread-function of a moderately loud injection ($\mathcal{L} \gtrsim \mathcal{L}_{\rm th} + 20$), at the sky location of the target, is a narrow ellipse ~ 2 arcmin wide in RA, but over ~ 30 arcmin tall in Dec. When we search a 100 arcmin^2 patch of sky around the location of SAX J1808.4−3658 we do not see any evidence of this point-spread-function at the source location. There is an ellipse with $\mathcal{L} > \mathcal{L}_{\rm th}$ roughly −2 arcmin away in RA from SAX J1808.4−3658, but as the location of the target is known to sub-arcsec precision [58], this ellipse is likely a noise fluctuation, rather than an astrophysical signal.

We also calculate $\mathcal{L}$ in a small, densely sampled patch of the $\{P,\ T_{\rm asc}\}$ parameter space around the candidate's template. As discussed in Appendix B 1, moderately loud injections ($\mathcal{L} \gtrsim \mathcal{L}_{\rm th} + 20$) "spread out" in the $\{P,\ T_{\rm asc}\}$

TABLE V: Target, starting frequency, f_s, for each ~ 0.61 Hz-wide sub-band, threshold calculated using Gaussian noise realizations and the exponential tail method, $\mathcal{L}^{e}_{\mathrm{th,\,G}}$, and threshold calculated using off-target noise realizations and the percentile method, $\mathcal{L}^{p}_{\mathrm{th,\,OT}}$. All thresholds are calculated with $\alpha_{N_{\mathrm{tot}}} = 0.3$.

Target	f_s (Hz)	$\mathcal{L}^{e}_{\mathrm{th,\,G}}$	$\mathcal{L}^{p}_{\mathrm{th,\,OT}}$	Target	f_s (Hz)	$\mathcal{L}^{e}_{\mathrm{th,\,G}}$	$\mathcal{L}^{p}_{\mathrm{th,\,OT}}$
IGR J00291+5934	598.6	291.9	1136.7	IGR J17498−2921	400.7	304.6	298.4
	798.2	294.9	288.4		534.4	304.7	297.9
	1197.5	295.2	287.6		801.7	311.2	304.5
MAXI J0911−655	339.7	297.0	290.0	IGR J17511−3057	244.5	302.0	293.7
	453.0	305.4	298.2		326.1	303.4	295.8
	679.6	305.5	300.4		489.4	305.1	297.9
XTE J0929−314	184.8	311.9	304.9	XTE J1751−305	435.0	312.8	316.0
	246.5	307.4	301.2		580.1	312.9	306.6
	369.9	310.4	304.5		870.3	319.9	315.7
IGR J16597−3704	104.9	321.6	316.4	Swift J1756.9−2508	181.8	308.7	302.8
	139.9	322.9	625.5		242.5	317.4	312.8
	210.0	323.7	318.5		363.8	315.3	309.0
IGR J17062−6143	163.4	292.1	285.1	IGR J17591−2342	527.1	299.3	289.4
	217.9	289.1	281.8		702.9	302.0	295.7
	327.0	293.3	283.3		1054.5	304.7	298.2
IGR J17379−3747	467.8	307.4	298.9	SAX J1808.4−3658	400.7	303.8	294.8
	623.8	307.4	299.9		534.3	305.0	296.1
	935.9	311.1	305.7		801.6	309.3	301.4
SAX J1748.9−2021	442.1	308.2	300.3	XTE J1807−294	190.3	295.5	287.0
	589.5	310.1	301.6		253.9	296.8	289.0
	884.4	311.5	304.9		380.9	299.7	292.0
NGC 6440 X−2	205.6	292.8	281.3	XTE J1814−338	314.1	301.8	293.3
	274.2	298.3	288.6		418.8	302.3	294.3
	411.5	295.9	287.2		628.4	305.8	298.4
IGR J17494−3030	375.7	315.3	309.3	IGR J18245−2452	254.0	311.2	305.4
	501.1	317.5	13763.8		338.8	312.5	305.9
	751.8	322.2	316.5		508.4	317.3	13569.7
Swift J1749.4−2807	517.6	316.4	308.8	HETE J1900.1−2455	377.0	299.6	288.1
	690.3	318.4	311.9		502.8	303.1	8459.4
	1035.5	321.0	316.3		754.3	303.8	294.7

TABLE VI: Orbital template, $(P,\ a_0,\ T_{\mathrm{asc}})$, terminating frequency bin, $f(N_T)$, log-likelihood, $\mathcal{L}$, and the probability that a search of the candidate's sub-band in pure noise would return a candidate just as loud, p_{noise}, for the 16 candidates with $\mathcal{L} > \mathcal{L}_{\mathrm{th}}$ that cannot be eliminated by any of the vetoes detailed in Sec. VI.

Target	Candidate	P (s)	a_0 (lt-s)	T_{asc} (GPS time)	$f(N_T)$ (Hz)	$\mathcal{L}$	p_{noise}
MAXI J0911−655	1	2659.933	0.0176	1238165869.0437	453.309532	299.2	0.26
IGR J16597−3704	1	2758.61	0.0048	1238163275.6122	105.002195	316.5	0.30
	2	2757.90	0.0048	1238163010.7583	210.359055	323.5	0.09
IGR J17062−6143	1	2278.2112	0.0040	1238165942.2745	163.531805	286.4	0.24
	2	2278.2112	0.0040	1238165942.2745	218.452091	283.9	0.19
	3	2278.2112	0.0040	1238165942.2745	327.058287	290.0	0.05
IGR J17379−3747	1	6765.84	0.0770	1238162768.3832	623.819568	303.9	0.08
SAX J1748.9−2021	1	31555.29	0.3876	1238151700.2214	590.048237	304.9	0.12
	2	31555.30	0.3876	1238151760.9764	590.040010	302.3	0.27
	3	31555.31	0.3876	1238151710.6406	884.592276	305.6	0.22
IGR J17498−2921	1	13835.619	0.36517	1238164013.8774	801.703605	305.8	0.22
XTE J1807−294	1	2404.416	0.00483	1238165585.2721	381.000852	296.7	0.10
SAX J1808.4−3658	1	7249.15	0.0628	1238161168.0040	534.633578	298.2	0.16
	2	7249.16	0.0628	1238161183.0831	534.407934	296.2	0.30
XTE J1814−338	1	15388.723	0.3906	1238151585.3941	314.564137	297.7	0.08
HETE J1900.1−2455	1	4995.26	0.0184	1238161529.0866	754.378543	295.8	0.25

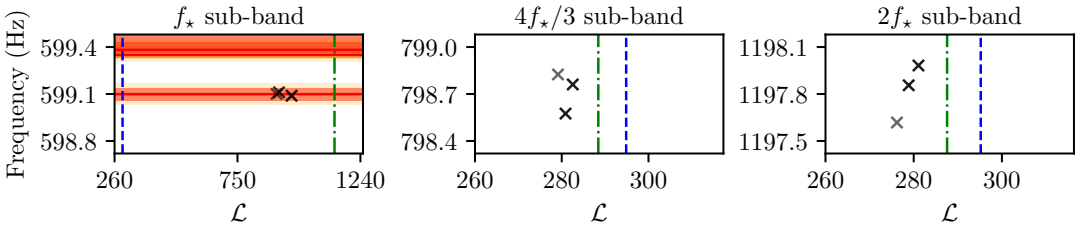

(a) Search results for IGR J00291+5934.

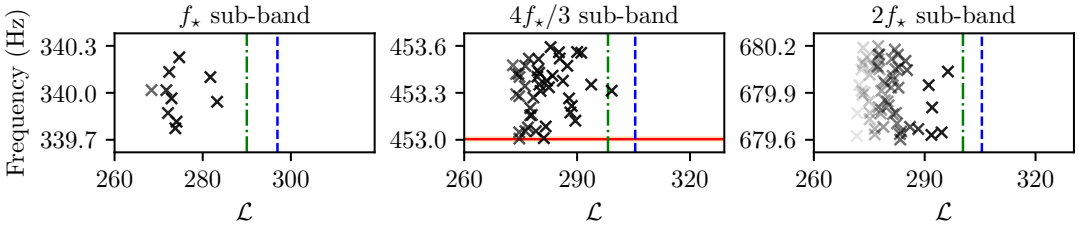

(b) Search results for MAXI J0911−655.

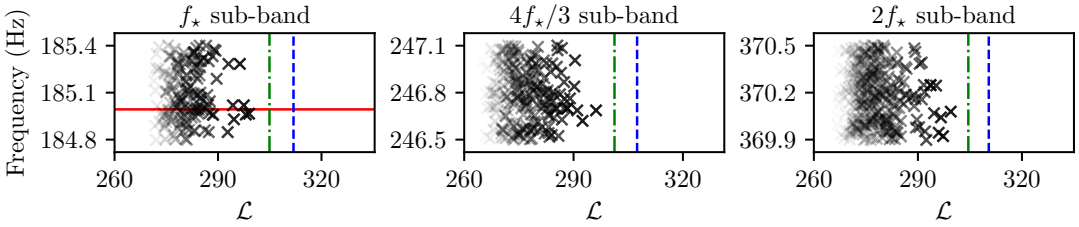

(c) Search results for XTE J0929−314.

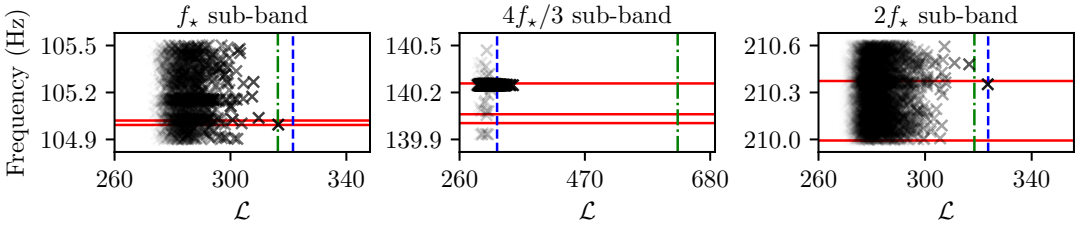

(d) Search results for IGR J16597−3704.

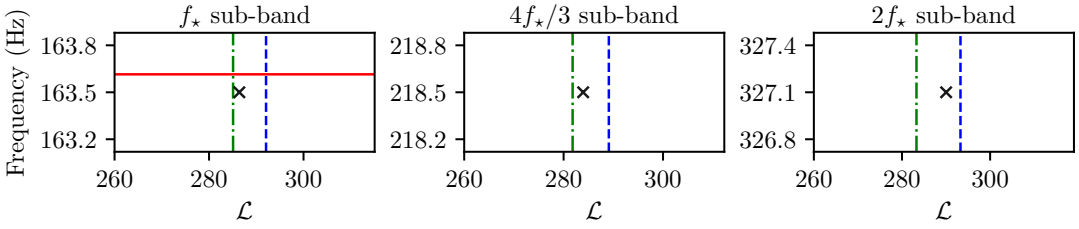

(e) Search results for IGR J17062−6143.

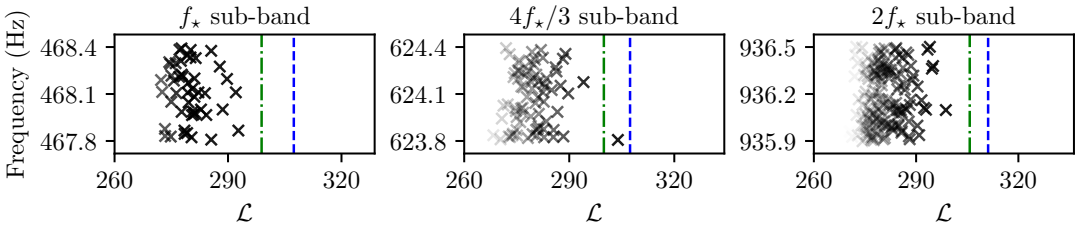

(f) Search results for IGR J17379−3747.

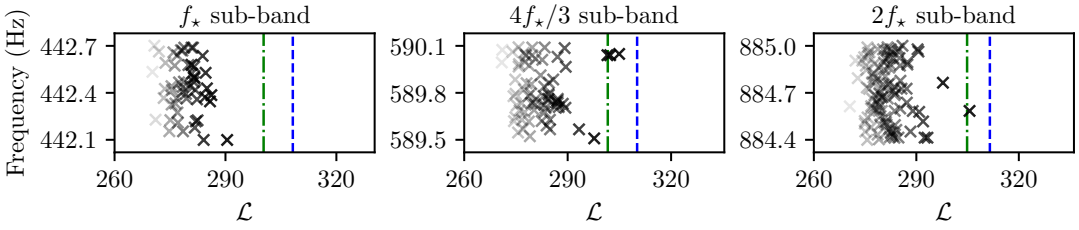

(g) Search results for SAX J1748.9−2021.

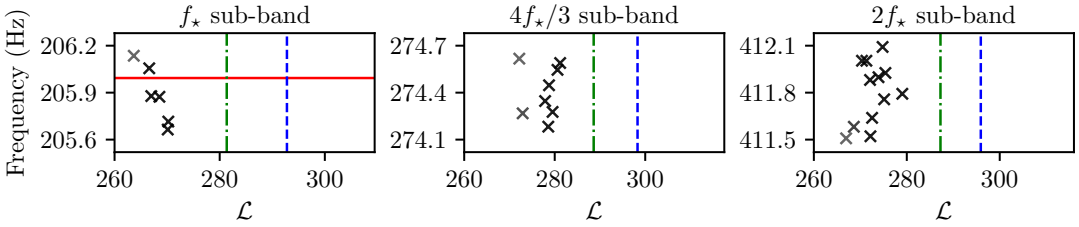

(h) Search results for NGC 6440 X−2.

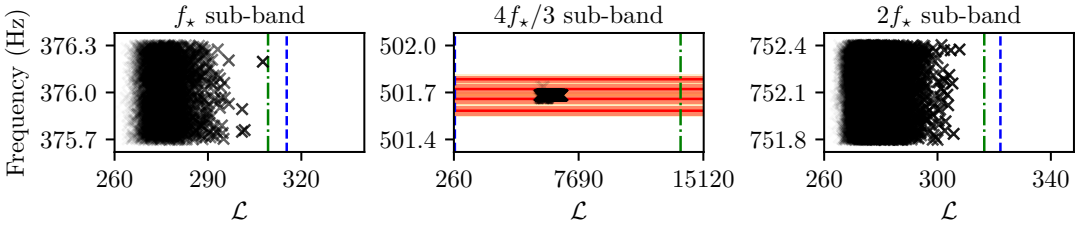

(i) Search results for IGR J17494−3030.

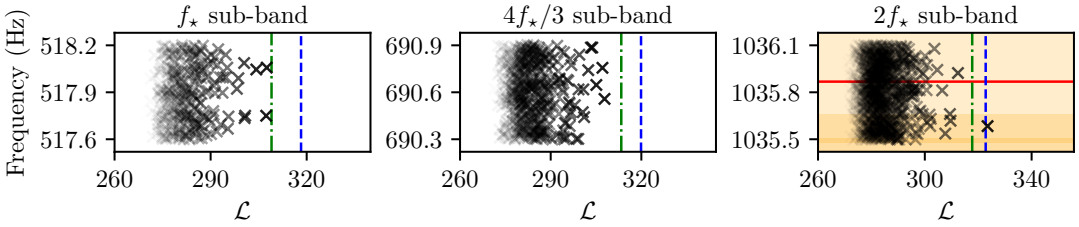

(j) Search results for Swift J1749.4−2807.

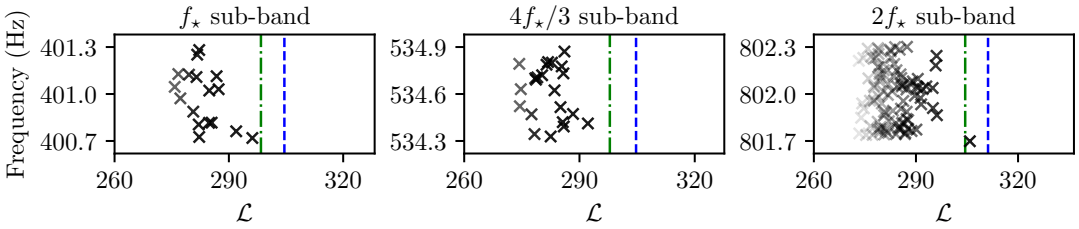

(k) Search results for IGR J17498−2921.

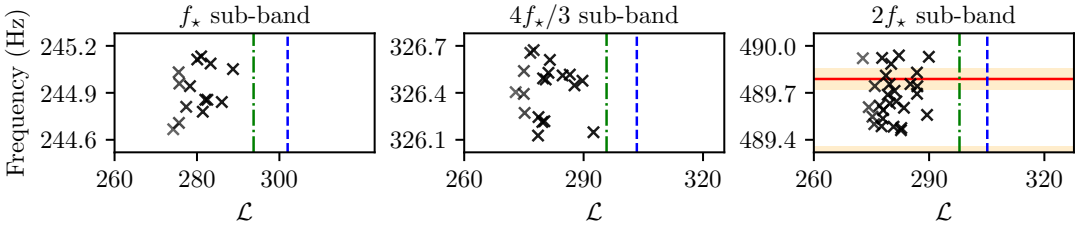

(l) Search results for IGR J17511−3057.

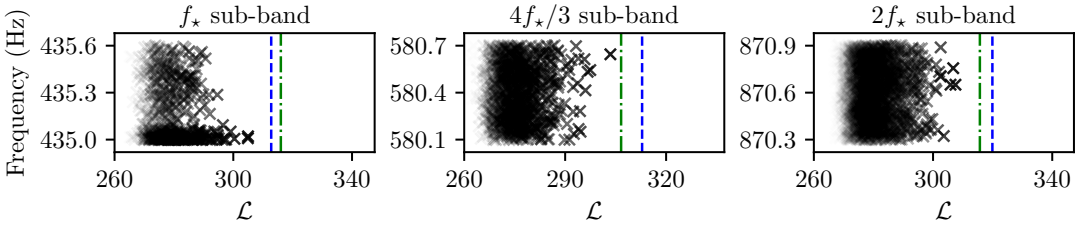

(m) Search results for XTE J1751−305.

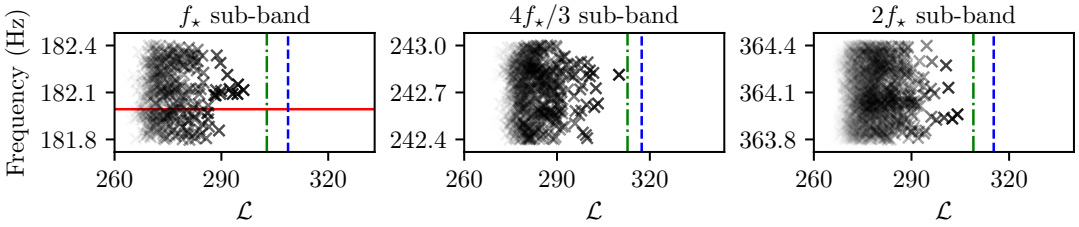

(n) Search results for Swift J1756.9−2508.

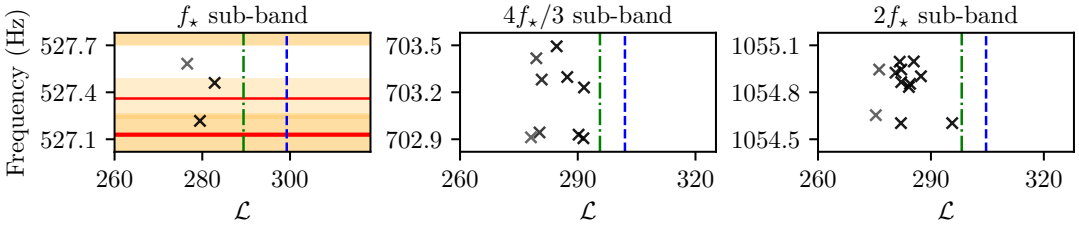

(o) Search results for IGR J17591−2342.

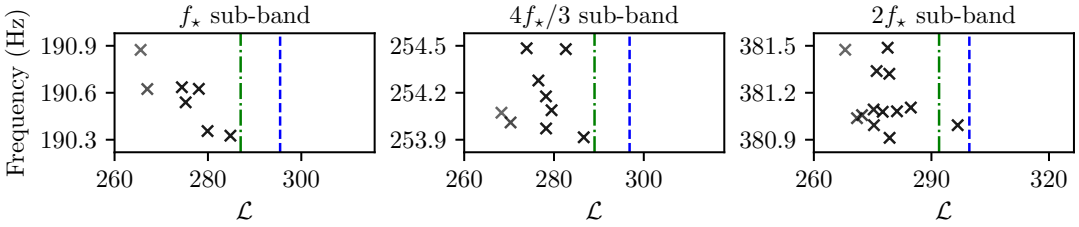

(p) Search results for XTE J1807−294.

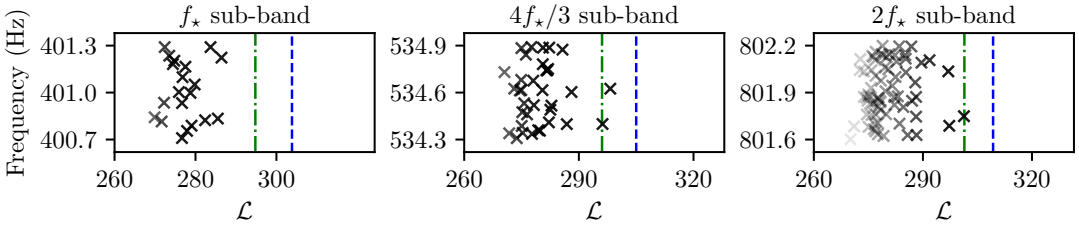

(q) Search results for SAX J1808.4−3658.

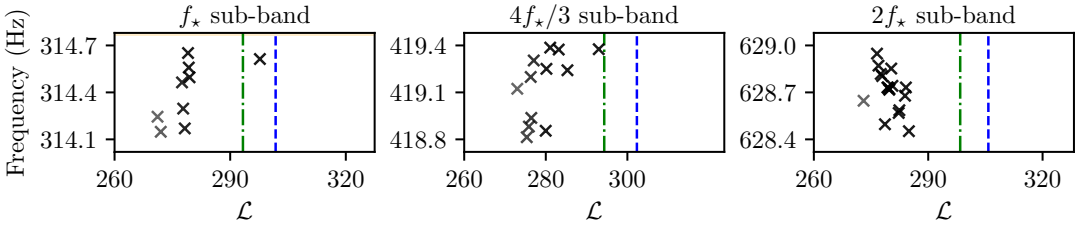

(r) Search results for XTE J1814−338.

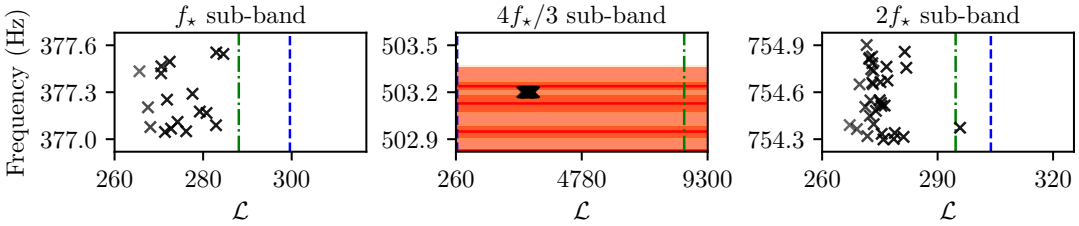

(s) Search results for HETE J1900.1−2455.

FIG. 4: Search results for each target and sub-band, laid out as in Fig 2. Black crosses indicate the frequency and $\mathcal{L}$ for the most likely path through the sub-band for each binary template. The vertical blue dashed (green dot-dashed) lines correspond to the threshold set via Gaussian (off-target) noise realizations, $\mathcal{L}_{\mathrm{th,\,G}}$ ($\mathcal{L}_{\mathrm{th,\,OT}}$), in each sub-band. Solid red lines indicate the peak frequency of known instrumental lines in the Hanford or Livingston detectors; the red band indicates the width of the line and the yellow band indicates the increased effective width due to Doppler broadening, as described in Sec. VI A. Multiple overlapping orange bands creates the red bands. The transparency of crosses in sub-bands with many templates, e.g. the sub-bands of IGR J16597−3704, is adjusted relative to the maximum $\mathcal{L}$ in that sub-band for clarity.

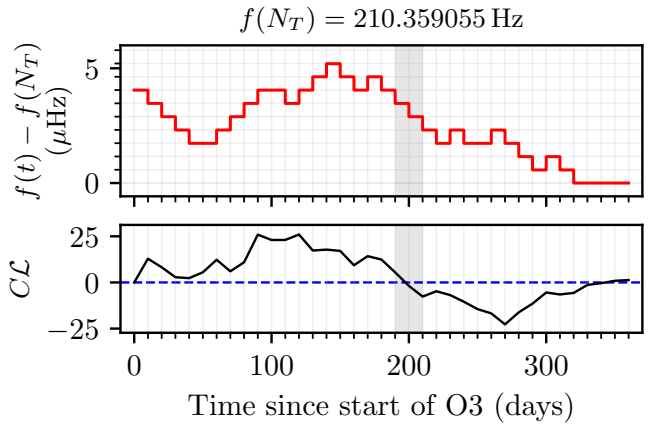

(a) Surviving candidate 2 from IGR J16597−3704.

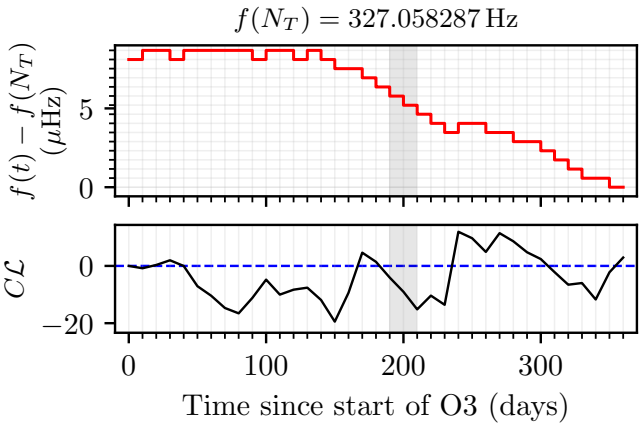

(b) Surviving candidate 3 from IGR J17062−6143.

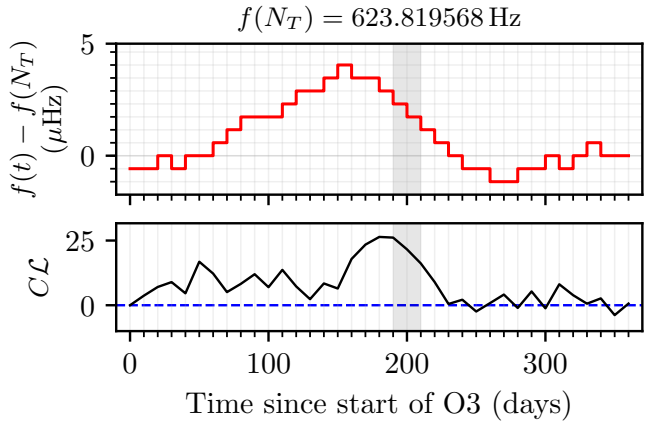

(c) Surviving candidate 1 from IGR J17379−3747.

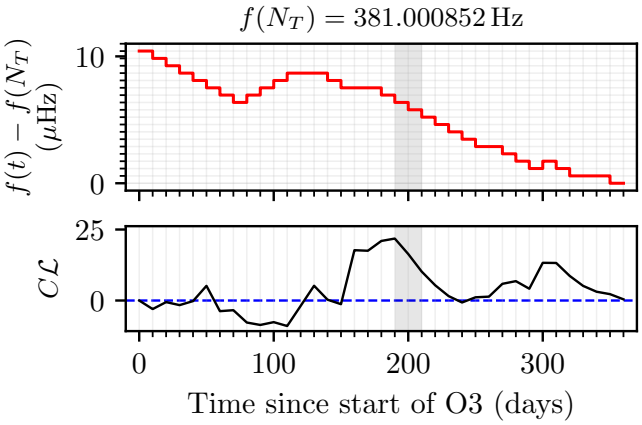

(d) Surviving candidate 1 from XTE J1807−294.

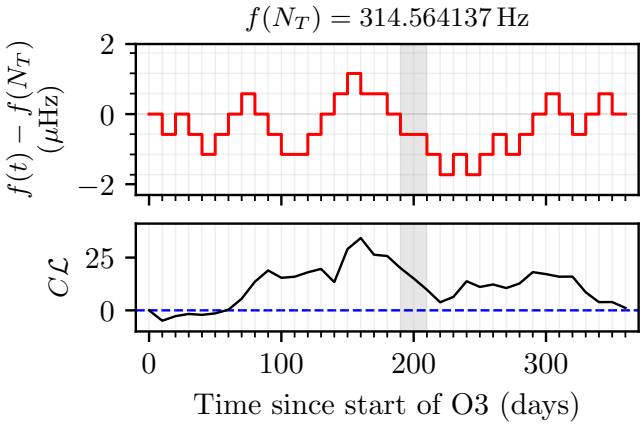

(e) Surviving candidate 1 from XTE J1814−338.

FIG. 5: Top panels: frequency paths, $f(t)$, for candidates with $p_{\mathrm{noise}} \leq 0.1$. The terminating frequency bin, $f(N_T)$, is subtracted and displayed in the title of each figure for clarity. Faint horizontal grey lines demarcate frequency bins of size $\Delta f = 5.787037 \times 10^{-7}\,\mathrm{Hz}$, while faint vertical grey lines demarcate chunks of length $T_{\mathrm{drift}} = 10\,\mathrm{d}$. Bottom panels: the cumulative log-likelihood along the frequency path relative to the average sum log-likelihood needed to reach $\mathcal{L}_{\mathrm{th}}$, $C\mathcal{L} \equiv \sum_{i=0}^{i=t} \left[\mathcal{L}(i) - \mathcal{L}_{\mathrm{th}}/N_T\right]$, where $\sum_{i=0}^{i=t} \mathcal{L}(i)$ is $\ln P(Q^*|O)$ from Eq. (2) truncated after the t-th segment. The horizontal blue dashed line corresponds to $\sum_{i=0}^{i=t} \mathcal{L}(i) = t\mathcal{L}_{\mathrm{th}}/N_T$. The grey shaded regions in both top and bottom panels correspond to the segments which have no SFTs and are therefore filled with a uniform log-likelihood, as described in Sec. V.

TABLE VII: Orbital template, (P, a_0, $T_{\rm asc}$), frequency, f, log-likelihood, $\mathcal{L}$, and the probability of seeing a candidate at least this loud in pure noise, $p_{\rm noise}$, for the remaining candidate from the target-of-opportunity, 24 d coherent search when SAX J1808.4−3658 was in outburst. The candidate cannot be eliminated by any of the vetoes detailed in Sec. VI.

P (s)	a_0 (lt-s)	$T_{\rm asc}$ (GPS time)	f (Hz)	$\mathcal{L}$	$p_{\rm noise}$
7249.155	0.062809	1249163578.03125	400.59656098	42.5	0.02

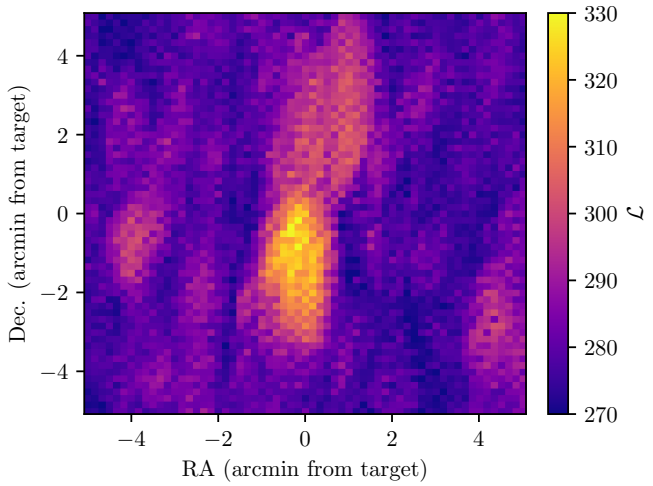

FIG. 6: $\mathcal{L}$, as represented by the color of each pixel, calculated at 3721 regularly spaced sky locations in a 100 arcmin^2 patch of sky, centered on IGR J16597−3704. See text in Appendix B 1 for details.

plane. However, the candidate is not loud enough for this diagnostic to provide evidence for or against the hypothesis that the candidate is a noise fluctuation.

If we assume that the remaining candidate is a false alarm, we calculate $h_0^{95\%}$ for the 24 d coherent search, using the procedure outlined in Sec. IX A. We find $h_0^{95\%} = 1.3 \times 10^{-25}$ for the sub-bands centered on $f_\star$ and $4f_\star/3$, and $h_0^{95\%} = 1.7 \times 10^{-25}$ for the sub-band centered on $2f_\star$. These upper limits are higher than the ones listed in Sec. IX B because the longer coherence time does not completely compensate for the shorter observation time.

Finally, we perform a complementary follow-up search using a deterministic signal template on the candidate of interest using `PyFstat` [150, 151]. The use of the `PyFstat` algorithm as a follow-up technique was applied to the last surviving outlier of Ref. [28] and previously in Refs. [24, 152]. The follow-up procedure, thoroughly described in Ref. [153], uses a Markov chain Monte Carlo (MCMC) sampler [154, 155] to explore a parameter-space region using the $\mathcal{F}$-statistic as log-likelihood [49]. Two coherence times are used here, namely $T_{\rm coh} = 12$ d and $T_{\rm coh} = 24$ d. Prior distributions are Gaussian distributions centered at the outlier parameters (Table VII) using a standard deviation of one parameter-space bin with maximum mismatch $\mu_{\rm max} = 1$ [109]. The results of the follow-up are evaluated using a Bayes factor, $\mathcal{B}_{\rm S/N}$, that compares the evidence for a model that the data contain a coherent signal to the evidence for a model that the data contain only noise. The value of $\mathcal{B}_{\rm S/N}$ is computed by comparing the change in the $\mathcal{F}$-statistic of the loudest candidate between the two follow-up stages with different coherence times: if a signal is present in the data, the $\mathcal{F}$-statistic should provide a consistent estimate of the signal-to-noise ratio; otherwise, the loudest candidate is a result of noise, the distribution of which follows a Gumbel distribution. This noise distribution is estimated using a similar method to the one described in Appendix A 4, with 600 off-source calculations performed.

The loudest candidate of the follow-up returns a log-Bayes factor of $\log_{10}\mathcal{B}_{\rm S/N} = 1.45$. We characterize the $\log_{10}\mathcal{B}_{\rm S/N}$ distribution using 400 isotropically distributed sources injected into the real data with an amplitude of $h_0^{95\%}$. We obtain a 1% false dismissal threshold of 8.75, which is significantly larger than the candidate's log-Bayes factor of 1.45. That is, if this were a true signal, with $h_0 = h_0^{95\%}$, we would expect the log-Bayes factor to be higher than what we see in the real data by about 7. We conclude that there is no significant evidence of continuous gravitational wave emission from this target.